The Interaction of Fast Flowing Plasma with Non-Magnetized Solar System Bodies: A New 3D Multi-fluid MHD Model of Mars and its Applications

by

Dalal Najib

A dissertation submitted in partial fulfillment
of the requirements for the degree of
Doctor of Philosophy
(Space and Planetary Sciences)
in The University of Michigan
2011

Doctoral Committee:

Professor Andrew F. Nagy, Co-Chair
Research Scientist Gábor Tóth, Co-Chair
Research Professor Stephen Bougher
Associate Professor Michael Liemohn
Professor Kenneth Powell
Assistant Research Geophysicist Yingjuan Ma

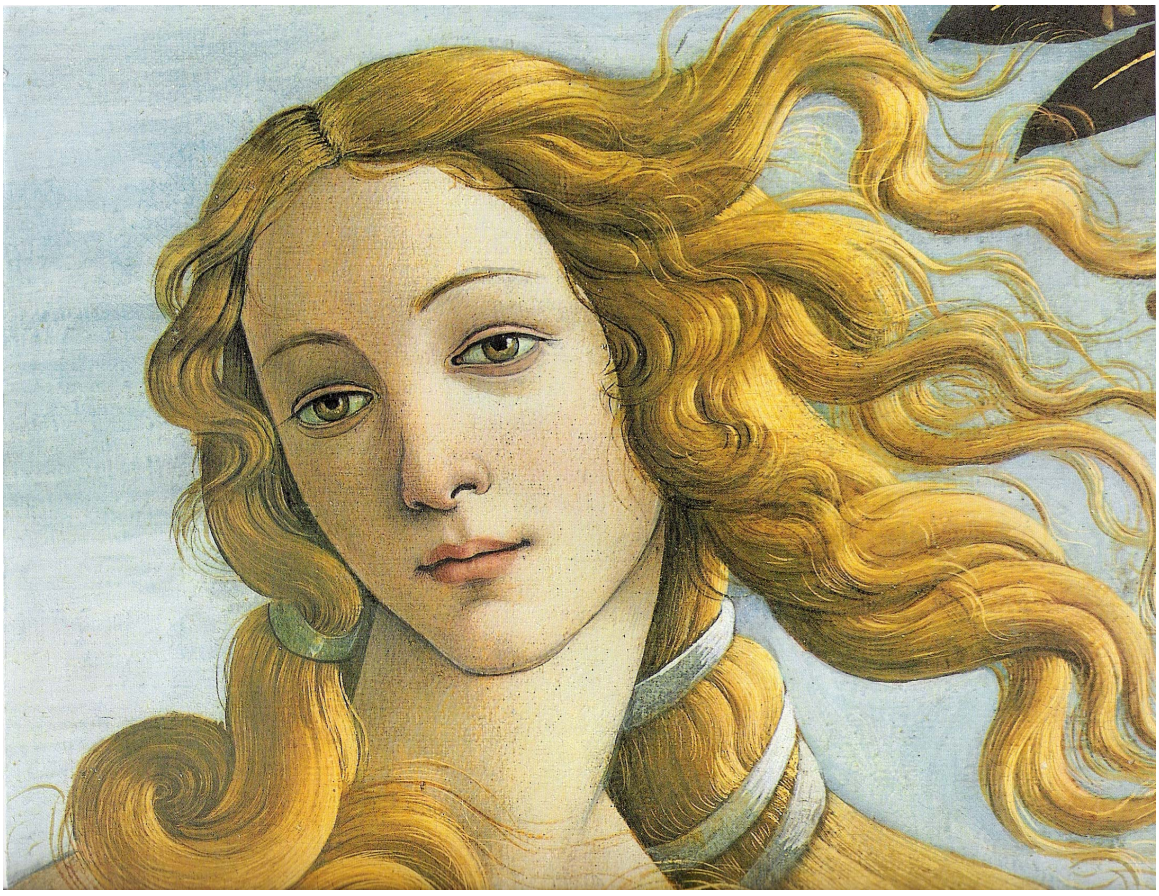

To my dear parents,

my mother Bouchra and my father Jilali,

for their love, support and guidance

ACKNOWLEDGEMENTS

Surprisingly, this is the most difficult part to write of my dissertation, since it involves acknowledging all the people who significantly contributed to my success without forgetting anyone, and thanking enough those I remembered.

My deepest gratitude goes to my advisor, Dr. Andrew Nagy for his mentorship and support. I have been extremely fortunate to have such an excellent advisor, who is always pushing me to do and be better. His extensive knowledge, his acute intuition and his endless encouragement made a significant difference in my academic training. On a personal level, he leaves on me an indelible mark of a very human person; I will always look up to his sense of integrity, his kindness and his willingness to teach, learn and help.

I also want to deeply thank Dr. Gábor Tóth for his tireless help. His knowledge, pedagogy, patience and modesty will never cease to impress me. He taught me how to approach problems in a methodic manner and he always gave me a honest and objective opinion about my work, allowing me to make significant progress in my research.

I would like to thank my committee members: Dr. Michael Liemohn for his precious advice and encouragement throughout my doctoral work, Dr. Stephen Bougher for his help, suggestions and for always caring about my progress, Dr. Yingjuan Ma for her continuous advice throughout my Phd work and Dr. Kenneth Powell, for graciously accepting to review my dissertation.

I also thank all the AOSS department faculty. I have been part of a community

that made me feel like family: the more time I spent here, the more I realized how fortunate I am to be close to such great minds who are at the same time very human and accessible. I deeply thank Dr. Lennard Fisk for his guidance and tremendous help, Dr. Thomas Zurbuchen for his continuous encouragement from day one, Dr. Tamas Gombosi and Dr. Steve Brecht for the very insightful discussions we had. To all the AOSS staff, thank you for always being very helpful, with a smile.

My gratitude goes to my colleagues and friends Martin Rubin, Jasper Kok, Raluca Ilie, Amanda Brecht, Valiery Tenishev, Alex Glocer, Fang Fang, Tony Visco, Noe Lugaz, Ofer Cohen, Patrick Sibanda, Erdal Yigit, Lars Daldroff , Yiqun Yu, Mitaire Ojaruega, Uthara Suvrathan, Javier Barrera, Paul Samaha, Myriam Afeiche, Cristina Reina, to name a few for their continuous support, interesting discussion and laughs. I thank my friends Isabelle Huynh, Remi Bourgeot, Alessia Trovato and Teja Schmidt McGuiness for sending me encouragements from across the ocean. I thank the Ibrahimi, Belhaj, Kastella and Ota families for their support.

Finally, this journey would not have been possible without the support and unconditional love of my family here in Ann Arbor and back in Morocco: I want to thank Fatos Kopliku for his support and for always believing in me. I thank my favorite sister Taghride and my favorite brother Fajr for always inspiring me to be better, I love you and I could not have done it without you. I thank my parents for their love, sacrifices and firm belief that education is the most important investment for our future; they never hesitated to put me and my siblings in the best schools or send us abroad when we had to, no matter how difficult these decisions were emotionally, socially or financially: I thank my mother Bouchra Saidi for her larger than life vision that made me everything I am today and my father Jilali Najib for his support and the unshakable principles he gave me.

TABLE OF CONTENTS

LIST OF FIGURES

Figure

LIST OF TABLES

Table

ABSTRACT

The Interaction of Fast Flowing Plasma with Non-Magnetized Solar System Bodies: A New 3D Multi-fluid MHD Model of Mars and its Applications

by

Dalal Najib

Co-Chairs: Andrew F. Nagy and Gábor Tóth

This dissertation presents numerical simulation results of the interaction of Mars ionosphere with the solar wind plasma using our new multi-fluid model, and the application of the model to Venus.

Our study starts with a multispecies Magnetohydrodynamics (MHD) single-fluid model. It contains four ion species, H^+, O_2^+, O^+ and CO_2^+ and includes an extensive chemistry model. We modify our existing single fluid model and solve the multi-fluid equations. This results in the ion species being decoupled, that is each one has its own density, velocity and pressure. We use a spherical adaptive grid system to obtain a very good altitude resolution (10km) and set the lower boundary at 100 km altitude in order to include the ionospheric region in our simulation.

Our results show clear asymmetries in the X-Z plane due to the effect of the electric field on the decoupled ions. These asymmetries, similar to the ones observed by kinetic models, could not be observed by the single fluid MHD model and show us a new distribution of the ions around the planet, a distinct magnetic field configuration and different escape fluxes. The model results agree well with Mars Global Surveyor

(MGS) and Viking observations. We use our Mars model to study the effect of different upstream conditions, the hot ionospheric oxygen corona and the crustal magnetic field. These applications show a clear change in the bow shock location and the ion distribution.

Finally, we successfully apply our multi-fluid model to Venus thus illustrating the versatility of our model. We reproduce the physical processes (asymmetries) calculated in Mars' case and observe, as expected, that kinetic effects are less pronounced in Venus' case. We use our model to study the effects of different solar wind conditions and we compare our results to observations by Pioneer Venus Orbiter (PVO) and Venus Express (VEX). Our results reproduce observed bow shock positions and show a reasonable fit to the data.

CHAPTER I

Introduction

1.1 General Background

The interaction of fast flowing plasma with non-magnetized solar system bodies has been the subject of several studies during the past decades. The fast flowing plasma is usually either the solar wind or the magnetospheric plasma of giant planets. It decelerates when it encounters an obstacle such as a planet, a satellite, a comet or an asteroid. However, the nature of this interaction can be very different based on the properties of the incident plasma conditions and the planetary obstacle. The details of these interaction processes are still subject to many uncertainties. The main reason for these uncertainties is the lack of relevant observations as well as the limitations of the numerical models used to study this type of processes (*Ledvina et al.*, 2008).

The fast flowing plasma in this study is the fully ionized solar wind , composed of hot and fast moving ionized particles. The solar wind is the extension of the solar corona to very large heliocentric distances. Due to the changing solar cycle, as well as the heliocentric distance, the properties of the solar wind plasma can be highly variable. When the fast flowing plasma interacts with a planet, a bow shock is formed and the flow is deflected around the obstacle. In the case where the planet has an intrinsic magnetic field, like at the Earth, Mercury and the giant planets, the interaction between the supersonic, superalfvenic, magnetized solar wind and the

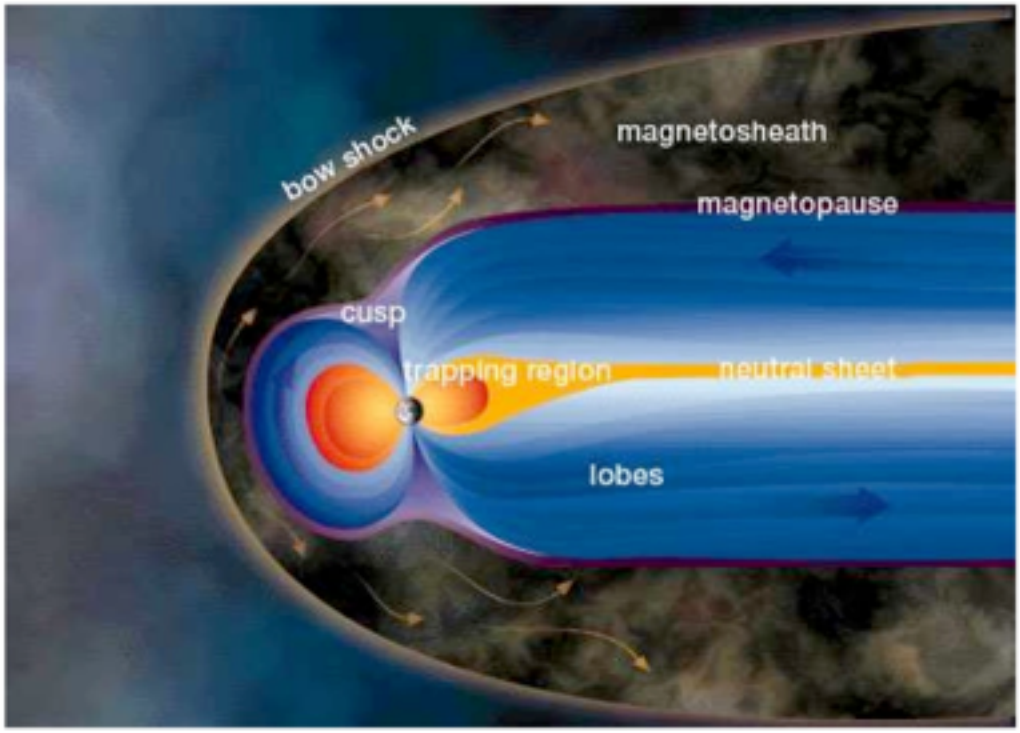

Figure 1.1: Interaction of the solar wind with the Earth's Magnetosphere (*Ma*, 2006)

intrinsic magnetic field of the Earth results in the formation of a magnetosphere. The outer limits of the magnetosphere is called magnetopause and the region between the magnetopause and the bow shock is referred to as the magnetosheath. Many complex wave and particle interaction processes take place in these regions. Figure 1.1 provides a representative illustration of these interaction regions.

Some solar system bodies do not have an intrinsic magnetic field. In these cases, many of the processes are different and the bow shock is also closer to the planet given the absence of a strong magnetic field. In the case of Mars and Venus, the two planets possess a substantial atmosphere, therefore, the solar wind plasma interacts directly with the ionosphere of the planet and its upper atmosphere. Thus the focus of this work is on interaction processes between the solar wind and planets that do not have an intrinsic magnetic field, but still have a substantial atmosphere.

In this chapter we first give a brief introduction to Mars and Venus, the two

non-magnetized solar system bodies we chose to focus on in this thesis, and then we provide an overview of the previous studies that have examined the topic, in particular previous and current numerical models.

1.1.1 Mars and Venus; Two Non-magnetic Solar System Bodies Interacting with the Solar Wind

In the case of non-magnetized planetary bodies, such as Venus and Mars, the obstacle to the supersonic solar wind flow is the ionosphere/atmosphere of the planet. Figure 1.2 illustrates the general overall structure seen around both Venus and Mars. A bow shock is formed a couple of planetary radii from the surface of the planet. The general region between the bow shock and the ionosphere is usually referred to as the magnetosheath, although there is no proper magnetosphere present. At Venus, where the maximum ionospheric thermal pressure is in general greater than the dynamic pressure of the upstream solar wind, there is a relatively sharp transition between the ionosphere and magnetosheath, at a location where these pressures are equal. This transition is called the ionopause. Most of the time a clear and sharp ionopause is not present at Mars and the transition is more gradual (*Duru et al.*, 2008). Between the bowshock and the ionosphere the shocked solar wind slows down and is deflected around the ionospheric obstacle. As the solar wind slows down, the imbedded interplanetary magnetic field increases and a magnetic pile up region is formed. At Venus this is usually referred to as the magnetic barrier region, while at Mars it is referred to as the magnetic pileup barrier and region. In this region there is an intermingling of both planetary and solar wind ions. Numerous review articles have appeared describing our understanding of these regions (c.f. *Schunk and Nagy*, 2009).

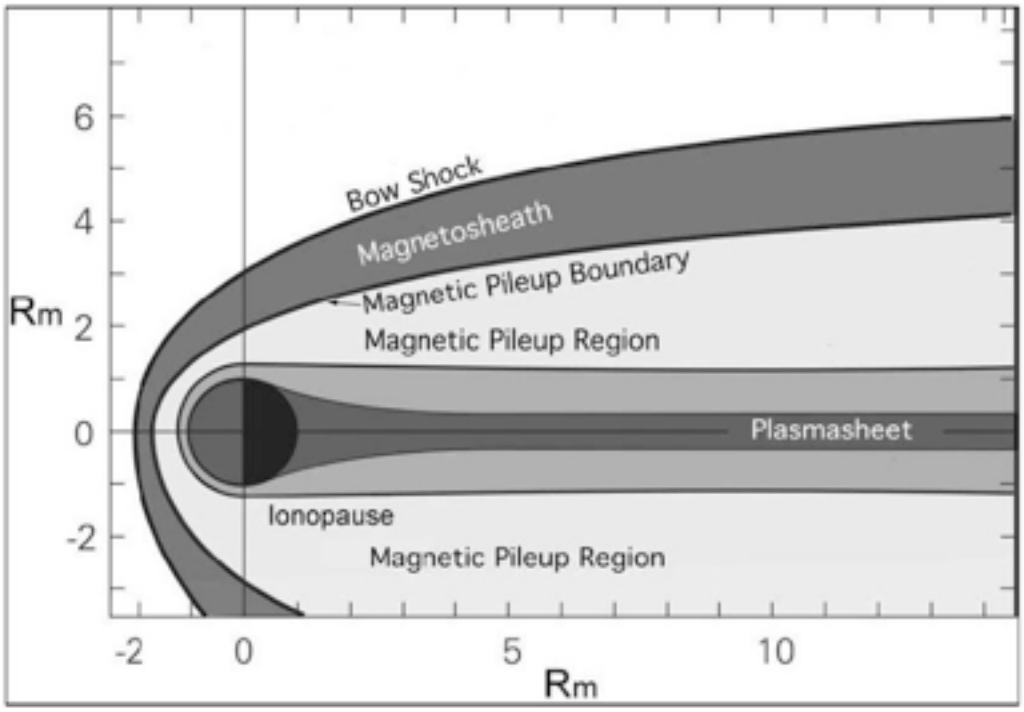

Figure 1.2: Sketch of the structure of the Martian environment as it interacts with the solar wind (*Schunk and Nagy*, 2009)

1.1.2 Mars

Besides being the God of War in ancient Roman mythology, Mars is also the fourth planet in the solar system and it has been dubbed for centuries as the Earth's "unidentical twin". It has fascinated many generations, especially as a potential second home. It has a radius of 3397 km, about half of that of the Earth. It is in a near circular orbit, at 1.52 AU from the Sun. The first mission to Mars was Mariner 4 in 1965, followed by other spacecrafts and landers on Mars, including Viking 1 and 2 in 1976. The Viking landers provided us with the only in-situ measurements of Mars upper atmosphere neutral composition and ionospheric plasma temperature. Of the many missions to Mars the other most relevant to the studies being discussed here are Mars Global Surveyor (MGS) and Mars Express (MEX). The next relevant and important mission to Mars is MAVEN, planned to be launched in 2013.

As the German-born English scientist William Hershel said in 1783 "The analogy

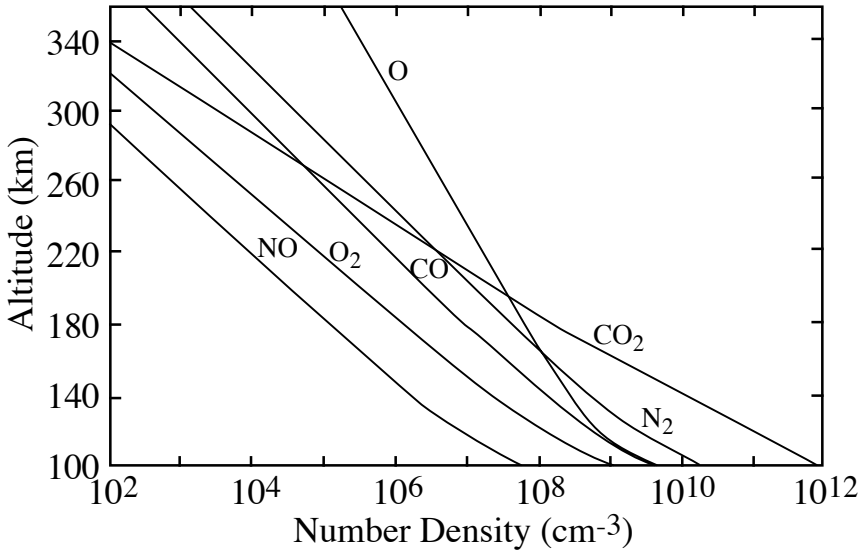

Figure 1.3: Representative neutral gas densities at Mars (*Chen et al.*, 1978).

between Mars and the Earth is, perhaps, by far the greatest in the whole Solar system". One of the main reasons is the similar inclination of the axis and the period of rotation, in addition to the presence of seasons like in Earth's case. Still, Mars is very different from the Earth. The major difference rests in the atmospheric density and composition, as well as the lack of a strong intrinsic magnetic field. However, Mars does have a remnant crustal field. The main constituent of Mars' atmosphere is carbon dioxide. Figure 1.3 shows the altitude profiles of the daytime, upper atmospheric neutral densities, based on Viking observations and ion density measurements (for the case of atomic oxygen) (*Hanson et al.*, 1977). While CO_2 is the dominant neutral species below 200 km altitude, atomic oxygen becomes dominant above this altitude (Figure 1.3). Mars exospheric temperatures are low and vary between 175 K and 300K (*Bougher et al.*, 1999, 2000). This is mainly due to the cooling effect of CO_2 15μm radiation.

The major source of daytime ionization at Mars is solar EUV radiation. The photoionization rate peak is at an altitude of 140 km (*Hanson et al.*, 1977). The major neutral at this altitude is CO_2, which led to believe that the major ion would be CO_2^+

as a direct consequence of the photoionization of CO_2. However, CO_2^+ transforms quickly into O_2^+, which becomes the major ion near 140 km altitude. The main chemical reactions are as follows:

$$\begin{aligned} CO_2 + h\nu &\rightarrow CO_2^+ + e^- \\ CO_2^+ + O &\rightarrow O_2^+ + CO \\ &\rightarrow O^+ + CO_2 \\ O + h\nu &\rightarrow O^+ + e^- \\ O^+ + CO_2 &\rightarrow O_2^+ + CO \\ O_2^+ + e^- &\rightarrow O + O \end{aligned}$$

At this time the only direct information regarding the ionospheric ion composition at Mars comes from two vertical profiles obtained by retarding potential analyzers carried aboard Vikings 1 and 2 (*Hanson et al.*, 1977).

Whether Mars possesses an intrinsic magnetic field or not was the subject of a lively debate within the scientific community for many years. However, MGS (Mars Global Surveyor) measurements, which were made deep in the ionosphere, unlike previous measurements, finally provided definitive answers to this long standing question. These measurements showed that the intrinsic diamagnetic field is negligible (less than 2 x 10^{21} G.cm^3), which is due to the absence of an active dynamo in the Martian core (*Acuna et al.*, 1998). It also found the unexpected presence of localized, small remnant crustal magnetic fields.

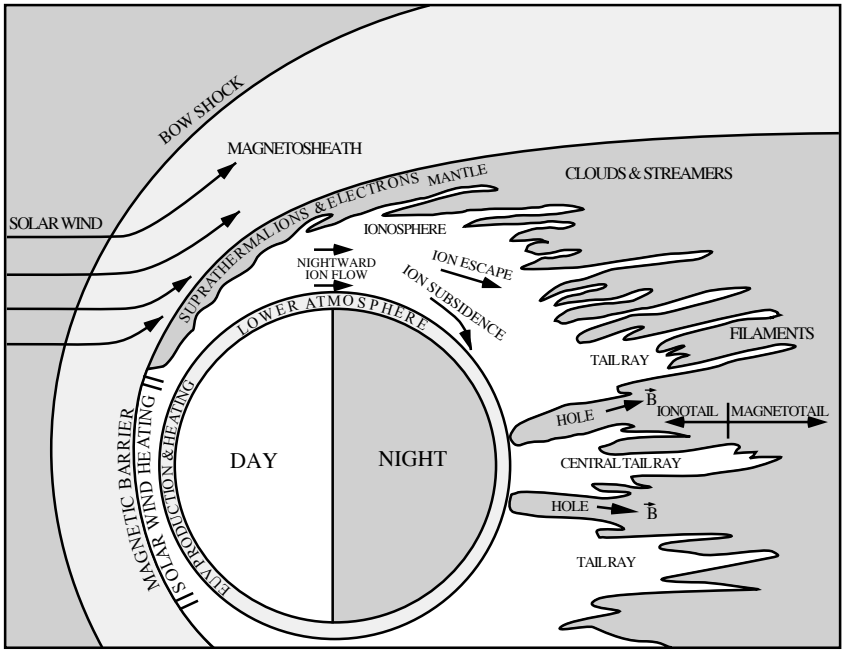

Figure 1.4: Interaction of the solar wind with Venus (*Schunk and Nagy*, 2009)

1.1.3 Venus

Venus is also often thought of as another "twin of the Earth". It is the second closest planet to the Sun, with a radius of 6051 km, only 650 km less than that of the Earth. It has an elliptic orbit with a semi-major axis of 0.7233 AU, orbiting the Earth every 224.7 Earth days. Venus has a long rotation period, which results in an effective night of about 58 Earth days. Since Mariner 2 flew by Venus in 1962, it has been the subject of intense investigation. The two missions that provided most of the information on the upper atmosphere and plasma environment of this planet are Pioneer Venus [measurements from 1978 to 1992] and Venus Express [2005 to to-date]. The data base from these missions means that we know more about the upper atmosphere and plasma environment of Venus than any other planet besides the Earth. Figure 1.4 describes the interaction process between Venus and the solar wind.

The dominant neutral gas species in the atmosphere of Venus is carbon dioxide,

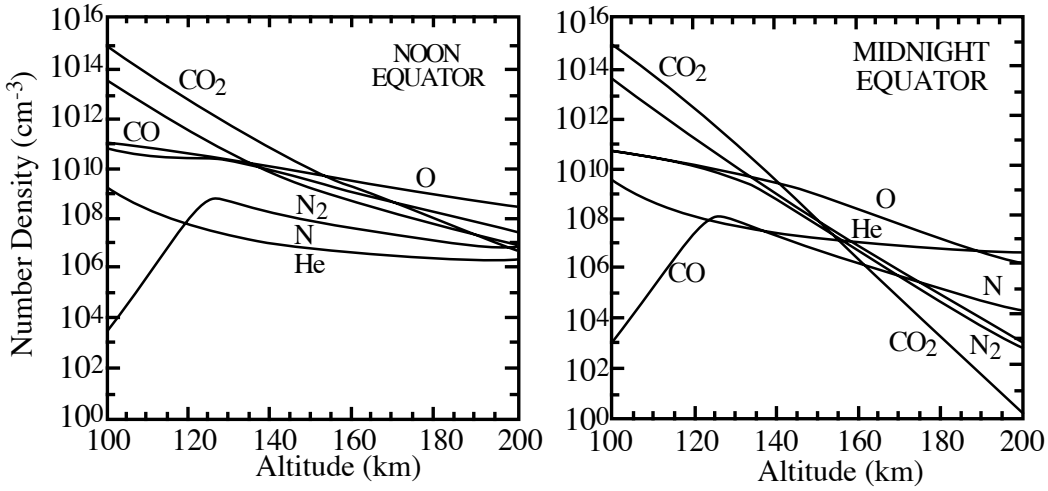

Figure 1.5: Representative neutral gas densities in the upper atmosphere of Venus (*Hedin et al.*, 1983)

similar to that of Mars. It is interesting to note that the surface pressure at Venus is more than a thousand times greater than at Mars, yet the upper atmospheric densities are quite similar, mainly because of the differences in gravity and temperatures in the lower atmosphere. Typical densities of the main neutral constituents are shown in Figure 1.5.

The typical upper atmospheric neutral gas temperatures vary from an average of about 280 K on the dayside to about 120 K on the nightside. Paradoxically, although Venus is closer to the Sun than Earth, the upper atmospheric temperatures are lower. As we have seen in Mars' case, this is also due to the cooling effect of CO_2 $15\mu m$ radiation, which is dominant in the altitude region between 100 and 160 km. It is important to mention though that the Venus temperatures vary less with solar cycle than those at Mars.

Given the very similar atmospheric composition at both Mars and Venus, the ion chemistry and resulting densities and composition are very similar. However, the data base for Venus is quite extensive. Typical observed and calculated ion densities are shown in Figure 1.6.

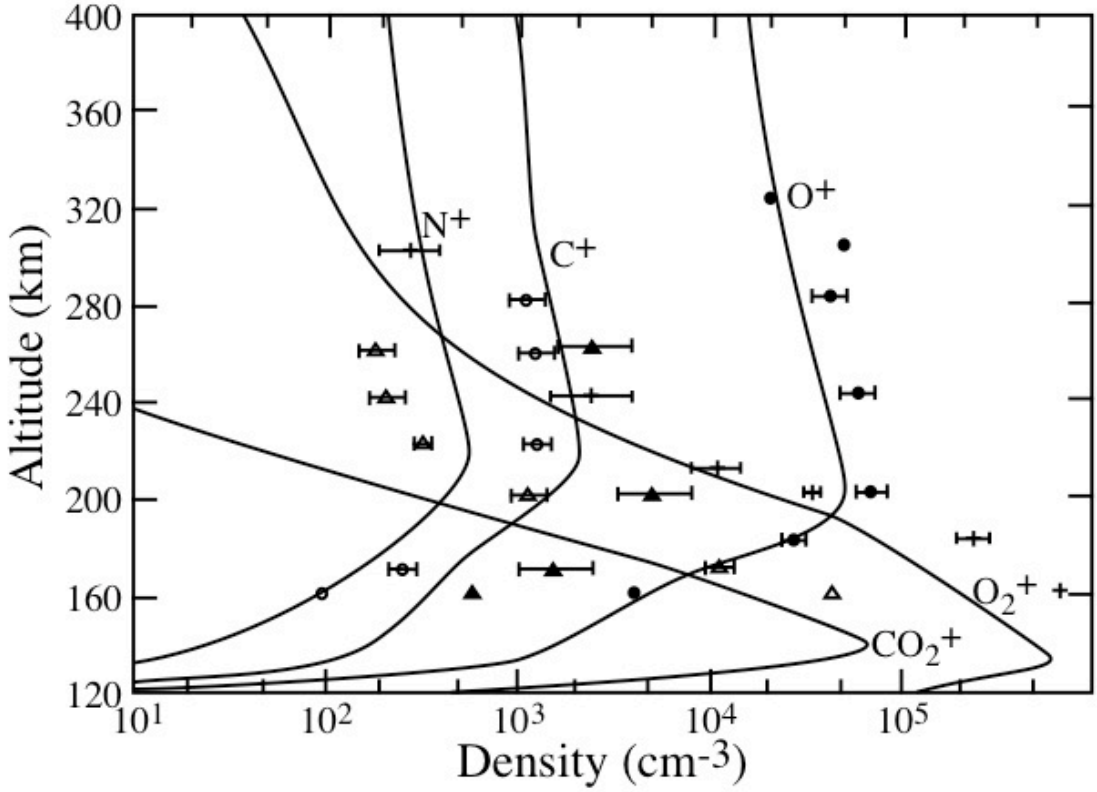

Figure 1.6: Measured and calculated daytime ion densities at Venus (*Nagy et al.*, 1980)

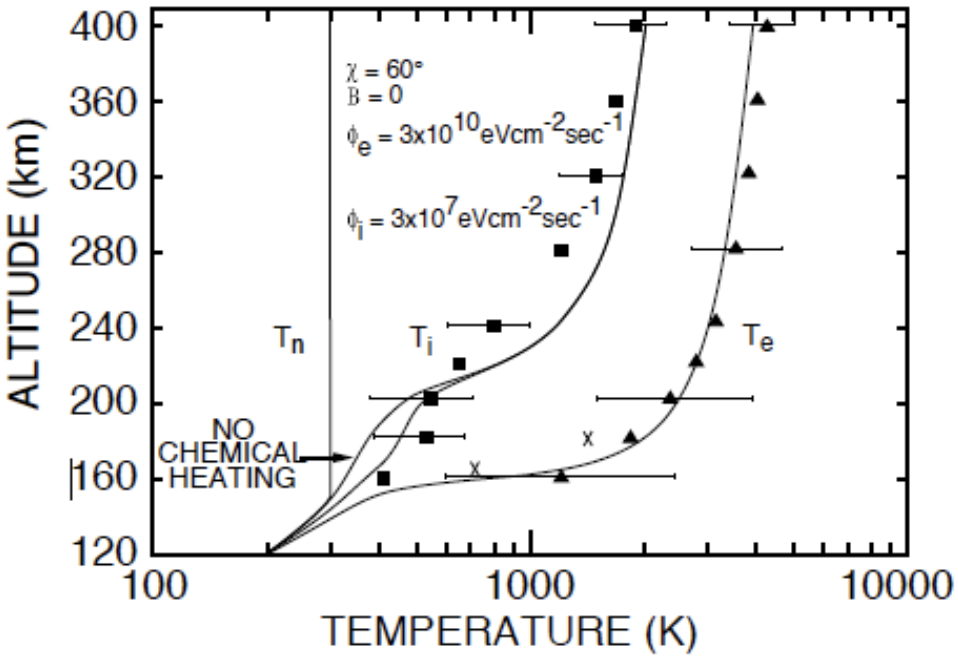

Figure 1.7: Measured (solid squares and triangles) and calculated (solid lines) electron and ion temperatures.

There is a great deal of electron and ion temperature data from Pioneer Venus, while only one set of measurements from the two Viking landers is available for Mars, at this time. Given the similar ion densities and composition the observed plasma temperatures are also believed to be similar. At both planets the observed temperatures exceed what one would expect from just solar radiation and classical thermal conductivities. At this time there is no clear understanding for the reason of these elevated temperatures, but it is believed to be a combination of reduced thermal conductivity and some topside energy input. Figure 1.7 shows representative measured and calculated electron and ion temperatures for Venus.

Venus does not have a significant intrinsic magnetic field. However, when the solar wind dynamic pressure is high, a significant induced horizontal magnetic field can be detected in the ionosphere. Vertical diffusion controls the altitude distribution

of the ion/electron density near the subsolar region, while horizontal plasma flows are dominant in larger solar zenith angles regions. Horizontal plasma velocities are believed to increase with altitude and solar zenith angle, reaching a few km/s at the terminator and becoming supersonic on the nightside (*Knudsen et al.*, 1980). These velocities are mainly driven by day-to-night pressure gradients. The result of these day to night flows along with soft electron precipitation results in a significant nightside ionosphere at Venus, despite the very long period of no solar radiation during the extended nighttime.

1.1.4 Conclusion

Mars and Venus present many similarities especially with respect to ionospheric composition and chemistry, and given the scarcity of in-situ measurements at Mars, our understanding of the planet has greatly benefited from the analogy with Venus. Another important similarity between the two planets are the mass loading (pick-up) processes. Pick up ions are the result of the ionization of extended neutral atmospheres that interact directly with the solar wind in the case of non-magnetized planets. The ionization can be by solar radiation, charge exchange reactions and impact ionization by the solar wind electrons. Given these similarities, it seems a natural choice to use the numerical model to be described in this thesis for both planets. However, one should keep in mind the existence of differences. Some of these differences and the associated implications are highlighted in Table 1.1.

1.2 Past Modeling Efforts

1.2.1 General introduction to past models

Numerous studies have been carried out in the past using particle, hybrid and MHD (single and multi fluid) models to simulate the interaction of fast flowing plasma

Table 1.1: Comparison of some physical properties between Mars and Venus (*Holmström and Kallio*, 2004)

Property	Difference	Implication
Planet radius and volume	1.8 and 6 times larger at Venus	Larger interaction region
Solar wind flux	Four times larger at Venus	Larger production
Gravity	Larger at Venus	Different exospheres
Internal magnetic fields	Crustal magnetizations at Mars	Modified flow
Proton gyroradius	Four times larger at Mars	Kinetics effects

with non-magnetized bodies. Two of these approaches have been used extensively: hybrid (*Brecht*, 1997; *Kallio et al.*, 2006, 2008; *Jarvinen et al.*, 2008; *Kallio et al.*, 2010) and MHD (*Ma et al.*, 2002, 2004; *Tanaka*, 1993; *Terada et al.*, 2009; *Benna et al.*, 2009) models. Both types of models have their strengths and their limitations (e.g, *Ledvina et al.*, 2008), thus we describe the general approach at this stage, without going into any deep discussion of the advantages and shortcomings of every model.

Hybrid or semi-kinetic models track the ions as particles. Ion motion and fields are solved self consistently, while electrons are treated as a massless fluid. This approach is usually applied to a collisionless plasma and when the electron mass (and the resulting kinetic effects) can be ignored.

MHD models treat the plasma as a charged neutral fluid. The single fluid MHD is described by a set of fluid equations that describe the conservation of mass, momentum and energy and the evolution of the magnetic field. It solves single continuity, momentum and pressure/energy equations, therefore it is a single species and single fluid model. However, when the plasma is composed of different species, it is more suitable to use an improved version of this model, the multispecies single fluid model. This model solves a separate continuity equation for every ion. This allows taking into account the ionospheric chemistry and accounts more accurately for the mass-loading (ion pick up) effects. It still solves only one momentum and energy/pressure equation and therefore treats the different species as one single fluid. Pick up ions,

as their name indicates, are picked up by the IMF and the convection electric field, and through momentum transfer, slow down the solar wind around the planet and therefore play an important role in the interaction process. However, some argue that despite the improvement that the multispecies single fluid MHD model formulation brings in the description of the existing physical phenomena, it is still limited by the fact that one fluid velocity and one temperature are imposed on the different species, while in reality these different species have their own dynamics and energetics. That is one of the main motivations for developing a multi-fluid model. This model not only solves separate continuity equations (as does the multispecies model), but also separate momentum and pressure/energy equations. Since the multi-fluid model and its applications are the subject of this thesis, we will provide a more accurate description of the model later.

1.2.2 Previous Modeling Studies of Mars

There have been numerous studies investigating the solar wind interaction with Mars. Hybrid models have been developed by *Brecht* (1997); *Brecht and Ledvina* (2006); *Modolo et al.* (2006) and *Simon et al.* (2007). They have been successful in describing flow patterns around the planet and the structure of the magnetic pile up boundary. However the spatial resolution of these hybrid models is still quite limited due to computing resources. This is not a drawback in case of some applications such as bow shock and magnetosheath studies, but becomes more of a problem in describing the ionosphere and the escape fluxes. The rapidly increasing computing capabilities will allow soon significant improvements in the spatial resolution used in these models.

Shinagawa and Bougher (1999) developed a two-dimensional MHD model of some aspects of the solar wind interaction with Mars ionosphere. While this model described the ionospheric electron density profiles and magnetic fields reasonably well,

it was not sufficient to account for the 3D effects, such as the tension of the magnetic field and some important plasma transport effects. Therefore, a 3D model became necessary. *Liu et al.* (1999) developed a 2-species, 3D, MHD model of Mars by considering solar wind protons and heavy O_2^+ separately. *Liu et al.* (2001) added a third major ion species O^+ to their model and also added a surface dipole field in order to simulate the crustal field. This model gave reasonable agreement with available data with respect to the bow shock location and structure. *Harnett and Winglee* (2003) developed a 3D, non-ideal single fluid model incorporating non-ideal MHD effects such as the Hall effect. However, there was no information about plasma composition, since the model did not include mass loading.

Next *Ma et al.* (2002, 2004) developed a multispecies MHD model for Mars using first a Cartesian (2002) and later a spherical grid (2004) structure. They were also able to have cell sizes as small as 10km in the ionospheric region and therefore obtain a much improved description of this region. This model did a good job in reproducing the observed density and magnetic field observations. The addition of the Hall effect to the model allowed them to describe some kinetic effects that cannot be accounted for with ideal MHD. This model has been applied extensively to Mars and Titan. However, the single fluid model is still limited by the single momentum and pressure/energy equations that fails to describe the individual dynamics and energetics of the ion species. A new multifluid model by *Harnett and Winglee* (2007) showed asymmetries that the single fluid MHD model could not show, however, it has limited ion composition capability and a very coarse resolution to describe the ionospheric processes appropriately.

1.2.3 Previous studies of Venus

Early model studies of Venus were based on gasdynamic calculations (e.g, *Spreiter et al.*, 1966). *Wu* (1992) used a time-asymptotic method to obtain a three dimensional

steady state solution to describe the MHD flow past Venus. This model showed that the magnetic pile up region resulted in the formation of a plasma depletion layer close to the obstacle. *Tanaka* (1993) developed a single species, single fluid MHD model using the newly developed finite volume total variation diminishing scheme (TVD) in order to study the interaction of the solar wind with non-magnetized bodies (Venus and Mars in particular). The model was able to describe several processes such as the formation of the bow shock and the structure inside the magnetosheath. Still, it could not describe accurately the mass loading processes. This model has been improved into a 2 species 3D MHD model (*Tanaka and Murawski*, 1997), which solved separate continuity equations for protons and for the O^+ in the ionosphere. This model succeeded in showing for the first time a nightside ionsophere, in addition to better describing the dayside interaction, including a clear ionopause. Fox and Sung [2001] conducted a comprehensive study modeling the low and high solar activity thermospheres and ionospheres of Venus. *Kallio et al.* (2006, 2008); *Barabash et al.* (2007) and *Jarvinen et al.* (2008) developed a hybrid model of Venus interaction with the solar wind and successfully described the flow pattern around the planet and the resulting kinetic effects. More recently, *Terada et al.* (2009) developed a comprehensive multispecies 3D model with 10 ion species. This model describes more accurately the ionospheric processes and mass loading and the model results compare very well with observations. Finally, *Benna et al.* (2009) applied to Venus a time dependent multi-fluid code with an adaptive mesh refined Cartesian grid.

1.3 Outline of the dissertation

In thesis, we will apply our new multifluid MHD model to Mars and Venus. This model treats the individual ions as separate fluids by solving individual continuity and momentum equations. This new model is the next logical step in our incremental improvement approach, as computational resources increase. This approach is

also very useful in checking and validating these extremely complex computational schemes.

In the next chapter, we will derive the governing equations of our multifluid MHD model. Then, in Chapter 3, we will present the numerical model that we are using. In Chapters 4 and 5, we will present the results of Mars and Venus simulations. Finally, we will conclude our work by a summary and a discussion of future work.

CHAPTER II

Multi-Fluid Equations

2.1 Transport Equations for Multi-fluid plasma

Magnetohydrodynamics (MHD) is the extension of fluid dynamics to plasmas and includes the effects of electric and magnetic fields. MHD equations can be obtained by combining macroscopic transport equations for the whole gas as a conducting fluid combined with Maxwells equations. MHD models are very popular tools to study the interaction of the solar wind with solar system bodies, both for magnetized and non-magnetized planets and moons. There are several types of MHD models. The single fluid single species model treats the plasma as a single, quasi-neutral and magnetized fluid. This model solves for the total mass density, the total momentum and the total energy. It proved to be very useful for many studies and was able to reproduce several features, such as the bow shock location. However, in the case of a plasma with multiple species as it is usually the case in planetary physics, this model becomes limited since it cannot account for the individual mass densities, velocities and pressures, thus it cannot evaluate accurately the mass loading, an important process in the case of non-magnetized planets.

A multi-species single fluid MHD model can account more accurately for mass loading by solving a continuity equation for each species. As a result, the model can solve for individual mass densities. However, it still treats the plasma as a single fluid

and solves for the total momentum and energy overlooking the separate dynamics of the different species.

The multi-fluid MHD model solves a separate continuity, momentum and energy equation for every ion. It is a more complex and more physically accurate model. It became necessary to use this model despite its complexity, in order to fully describe the interaction of the solar wind with non-magnetized bodies, Mars and Venus in particular, including the mass loading and flow patterns due to the decoupling of the ions.

The multi-fluid MHD model for Mars or Venus solves the separate MHD equations and includes the chemistry (ionization, recombination, charge exchange) and the elastic and non-elastic collisions in the source and loss terms.

In order to derive the multi-fluid MHD equations, we first start from the generalized transport equations, then we make assumptions and some simplifications in order to derive the MHD equations.

2.1.1 Generalized transport equation

Kinetic theory gives us the main key elements to connect the microscopic properties of the molecules composing a gas to the macroscopic properties of this gas. Let us consider one particle moving in a particular direction at a particular instant t. Each particle can be represented by a single point in the six-dimensional phase space *(x, y, z,* v_x, v_y, v_z*)* which can be denoted as (**r, v**), the vectors **r** and **v** being the Eulerian coordinates of the phase space.

We can then define for each gas species s the phase-space distribution function $F_s(\mathbf{r_s}, \mathbf{v_s}, t)$, which at an instant t, gives us the number of particles of species s, d^6N, within a phase-space element **r** to **r** + Δ**r** and $\mathbf{v_s}$ to $\mathbf{v_s}$ + $\Delta\mathbf{v_s}$.

Therefore we have:

$$d^6N = F_s(\mathbf{r_s}, \mathbf{v_s}, t) d^3r d^3v \tag{2.1}$$

Equation(2.1) shows that the phase-space distribution function, $F_s(\mathbf{r_s}, \mathbf{v_s}, t)$ is the density of the particles in the d^3rd^3v phase-space volume element around the phase-space point $(\mathbf{r_s}, \mathbf{v_s})$. Therefore the number density of species $n_s(t, \mathbf{r})$ can be obtained by integrating the phase space distribution function over the entire velocity space:

$$n_s(t, \mathbf{r}) = \iiint_{\infty} F_s(\mathbf{r_s}, \mathbf{v_s}, t) d^3v_s \tag{2.2}$$

Note that the phase-space distribution function $F_s(\mathbf{r_s}, \mathbf{v_s}, t)$ is different from the normalized phase-space distribution function $f_s(\mathbf{r_s}, \mathbf{v_s}, t)$.

$$\iiint_{\infty} f_s(\mathbf{r_s}, \mathbf{v_s}, t) d^3v_s = \frac{1}{n(\mathbf{r})} \iiint_{\infty} F_s(\mathbf{r_s}, \mathbf{v_s}, t) d^3v_s = 1 \tag{2.3}$$

We can write $n_s(t, \mathbf{r})$ as n_s for the sake of simplicity. Similarly, any average quantity $\langle Q_s \rangle$ be it density, flow velocity, temperature is given by

$$\langle Q_s \rangle = \iiint_{\infty} Q_s(\mathbf{v}) f_s(\mathbf{r_s}, \mathbf{v_s}) d^3v \tag{2.4}$$

The time evolution of each phase-distribution function $F_s(\mathbf{r_s}, \mathbf{v_s}, t)$ is described by the Boltzmann equation:

$$\frac{\partial F_s(\mathbf{r_s}, \mathbf{v_s}, t)}{\partial t} + \mathbf{v_s} \cdot \nabla_{\mathbf{r}} F_s(\mathbf{r_s}, \mathbf{v_s}, t) + \mathbf{a_s}(\mathbf{r_s}, \mathbf{v_s}, t) \cdot \nabla_{\mathbf{v_s}} F_s(\mathbf{r_s}, \mathbf{v_s}, t) = (\frac{\delta F_s(\mathbf{r_s}, \mathbf{v_s}, t)}{\delta t})_{coll} \tag{2.5}$$

The right hand-side term in equation (2.5) represents the changing rate of the phase-space distribution function due to both elastic and non-elastic collisions. Location $\mathbf{r}$, particle velocity $\mathbf{v}$ and time t are independent variables. The acceleration of the particle, $\mathbf{a_s}$, is the effect of external forces on the charged particles. In planetary ionospheres, this term consists mainly of the Lorentz and gravitational forces (*Schunk*

and Nagy, 2009):

$$\mathbf{a_s} = \mathbf{G} + \frac{q_s}{m_s}(\mathbf{E} + \mathbf{v_s} \times \mathbf{B}) \tag{2.6}$$

It is usually assumed in kinetic theory that the acceleration of a molecule $\mathbf{a_s}(t, \mathbf{r}, \mathbf{v})$ is divergenceless in velocity space, $\nabla_v \cdot \mathbf{a_s} = 0$. Lorentz and gravitational forces satisfy this condition and so do most of external forces.

The bulk gas flow or average drift velocity can be defined as $\mathbf{u_s} = \langle v_s \rangle$. The Boltzmann equation can also be expressed in terms of the random velocity $\mathbf{c_s}$, which is the velocity of the particle with respect to $\mathbf{u_s}$, at time t and location $\mathbf{r}$:

$$\mathbf{c_s} = \mathbf{v_s} - \mathbf{u_s}(t, \mathbf{r}) \tag{2.7}$$

If we multiply (2.5) by $m_s, m_s\mathbf{c}_s$ and $m_s\frac{c_s^2}{2}$ and integrate over the entire velocity space we obtain the continuity, momentum and energy equations. This corresponds to taking the zeroth, first and second velocity moments of the Boltzmann equation:

$$m_s\frac{\partial n_s}{\partial t} + m_s\nabla \cdot (n_s\mathbf{u}_s) = m_s\frac{\delta n_s}{\delta t} \tag{2.8}$$

$$m_s n_s\frac{\partial \mathbf{u}_s}{\partial t} + m_s n_s(\mathbf{u_s} \cdot \nabla)\mathbf{u}_s + \nabla \cdot P_s - n_s m_s\mathbf{G} - n_s q_s(\mathbf{E} + \mathbf{u}_s \times \mathbf{B}) = \frac{\delta M_s}{\delta t} \tag{2.9}$$

$$\frac{1}{\gamma - 1}\frac{\partial p_s}{\partial t} + \frac{1}{\gamma - 1}(\mathbf{u}_s \cdot \nabla)p_s + \frac{\gamma}{\gamma - 1}p_s(\nabla \cdot \mathbf{u}_s) + (\nabla \cdot \mathbf{h}_s) = \frac{\delta E_s}{\delta t} \tag{2.10}$$

where γ is the heat ratio and it is equal to $\frac{5}{3}$ if we assume that the particles have no internal degree of freedom. $\mathbf{h}_s$ in the energy equation is the heat flux and is defined as $\mathbf{h}_s = \frac{1}{2}m_s n_s\langle c_s^2\mathbf{v}_s\rangle$ .This term can be approximated by $\mathbf{h}_s = -\kappa\nabla T_s$ when collisions are frequent. We will neglect $\mathbf{h}_s$ in our calculation. P_s is the pressure tensor and is defined as the net rate of transport of molecular momentum per unit area, that is, the net flux of momentum across unit area due to random particle motion. $P_{ij}(t, \mathbf{r})$

is given by

$$P_{i,j}(t,\mathbf{r}) = m \iiint_{\infty} c_i c_j F(t,\mathbf{r},\mathbf{c}) d^3c \tag{2.11}$$

P_s can also be written as $P_s = m_s n_s \langle \mathbf{c_s c_s} \rangle$ and can be expressed using the scalar pressure p_s and stress tensor τ_s:

$$P_s = p_s \mathbf{I} + \tau_s \tag{2.12}$$

where p_s the scalar pressure is given $p_s = \frac{1}{3} m_s n_s \langle c_s^2 \rangle$. The stress tensor τ_s can be neglected when collisions are important. We will assume it is the case in our work, the diagonal elements of the pressure tensor are therefore the dominating elements and they are generally equal; we assume that the plasma is isotropic and $P_s = p_s \mathbf{I}$.

2.1.2 Collision Terms in Transport Equations for Multi-Fluid Plasma

As mentioned previously, the collision term in the right hand side of the transport equation describes the rate of change of the distribution function, due to collisions. We will consider two types of collisions:

- Elastic collisions: this type of collisions does not change the identity of the particle
- Inelastic collisions: this type of collisions changes the identity of the particle and can include photoionization, impact ionization, charge transfer and recombination

2.1.2.1 Elastic collisions

Elastic collisions by definition do not change the identity of the particles. The rate of change of the phase-space distribution function due to elastic collisions was derived by Boltzmann (the derivation can be found in *Gombosi* (1994); *Schunk and*

Nagy (2009) and is called the "Boltzmann collision integral"). It is a complicated nonlinear, multidimensional integral of the distribution function. The rate of change described by the Boltzmann collision integral drives the solution of the Boltzmann equation towards equilibrium. Although there have been several simplified approximations to the Boltzmann collision integral, the most widely used one (and also the simplest) is the so-called "relaxation time" approximation or BGK (*Gombosi*, 1994; *Schunk and Nagy*, 2009). The relaxation time approximation assumes the phase-space distribution function F_s is being gradually replaced by an equilibrium (Maxwellian) distribution functionvF_0, with a time constant τ_{st}:

$$\frac{\delta F_s(\mathbf{r_s}, \mathbf{v_s}, t)}{\delta t} = -\sum_{t=all} \frac{F(t, \mathbf{r}, \mathbf{v}) - F_{0s(st)}(t, \mathbf{r}, \mathbf{v})}{\tau_{BGK}} \tag{2.13}$$

where the subscript t refers to all species present in the gas mixture (including species s) and τ_{st} is the velocity-independent average collision time between particles s and t. As a results of these collisions between s and t, the distribution function of particles s asymptotically approaches $F_{0s(st)}$. It is important to note that $F_{0s(st)}$ is not only dependent on s but also on t, therefore $F_{0s(st)}$ changes as the distributions of both s and t particles change with time. The parameters of $F_{0s(st)}$ can be obtained by requiring that the total mass, momentum and energy of the s and t gases be conserved:

$$F_{0s(st)} = n_s\Big(\frac{m_s}{2\pi k T_{s(st)}}\Big)^{\frac{3}{2}} exp\Big[-\frac{m_s}{2kT_{s(st)}}(\mathbf{v}_s - \mathbf{u}_{st})^2\Big] \tag{2.14}$$

where

$$\mathbf{u}_{st} = \frac{m_t\mathbf{u}_t + m_s\mathbf{u}_s}{m_s + m_t} \tag{2.15}$$

$$T_{s(st)} = T_s + \frac{m_s m_t}{(m_s + m_t)^2}[2(T_t - T_s) + \frac{m_t}{3k}(\mathbf{u}_t - \mathbf{u}_s)^2] \tag{2.16}$$

Similarly to what we did in order to evaluate the left hand side of the transport equations, we calculate the zeroth, first and second velocity moment of Equation (2.13) by multiplying it with $m_s, m_s\mathbf{c}_s$ and $m_s\frac{c_s^2}{2}$ and integrating over the entire velocity space. We obtain the transfer integrals for elastic collisions:

$$\left(\frac{\delta n_s}{\delta t}\right)_{elastic} = 0 \tag{2.17}$$

$$\left(\frac{\delta M_s}{\delta t}\right)_{elastic} = m_s n_s \sum_{t=all} \nu_{st}(\mathbf{u}_t - \mathbf{u}_s) \tag{2.18}$$

$$\left(\frac{\delta E_s}{\delta t}\right)_{elastic} = \sum_{t=all} \frac{m_s n_s \nu_{st}}{m_s + m_s}[3k(T_t - T_s) + m_t(\mathbf{u}_t - \mathbf{u}_s)^2] \tag{2.19}$$

where ν_{st} is the non-resonant momentum transfer collision frequency and is defined as:

$$\nu_{st} = \frac{m_t}{m_s + m_t}\frac{1}{\tau_{st}} \tag{2.20}$$

There are several types of collisions: ion-ion, ion-neutral, electron-electron, electron-neutral and ion-electron collisions. We will give an overview of the collisions that play a significant role in ionospheric regions.

- Ion-neutral collisions

  The collision frequency ν_{in} between ion and neutral can be approximated using the neutral polarizability γ_n as (*Schunk and Nagy*, 2009):

  $$\nu_{in} = 2.21\pi\frac{n_s m_n}{m_i + m_n}\left(\frac{\gamma_n e^2}{\mu_{in}}\right) \tag{2.21}$$

  where μ_{in} is the reduced mass and is defined by

  $$\mu_{in} = \frac{m_i m_n}{m_i + m_n} \tag{2.22}$$

and where the neutral polarizabilarity γ_n is given by

$$\gamma_n = \alpha_n \times 10^{-24} cm^3 \tag{2.23}$$

Therefore equation (2.21) becomes:

$$\nu_{in} = 2.7 \times 10^{-9} \frac{n_n (\alpha_n \mu_{in})^{1/2}}{m_i} s^{-1} \tag{2.24}$$

Finally, we can write ν_{in} in an even simpler form:

$$\nu_{in} = C_n n_n \tag{2.25}$$

The values of C_n can be found in *Schunk and Nagy* (2009)

- Ion-ion collisions

  Ion-ion collisions play a significant role in the lower atmosphere since they couple the individual ions temperatures. The ion-ion frequency can be written in this form:

$$\nu_{st} = B_{st} \frac{n_t}{T_t^{\frac{3}{2}}} \tag{2.26}$$

  where B_{st} is a numerical coefficient; the corresponding values are given in *Schunk and Nagy* (2009)

- Electron-neutral collisions

  The parameter for elastic electron-neutral collisions that is generally measured is the velocity-dependent momentum transfer cross section Q_{en}. We do not go in the details of computing the value of Q_{en} which can be found in *Schunk and Nagy* (1980, 2009).

- Electron-ion collisions

  A lengthy derivation of electron-ion collisions frequency ν_{ei} can be found in *Schunk and Nagy* (2009) and gives us:

$$\nu_{ei} = 54.5 \frac{n_i Z_i^2}{T_e^{3/2}} \tag{2.27}$$

  where subscript e denotes electrons and subscript i denotes ions and Z_i is the particle charge number. The density n_i is in cm^{-3} and the electron temperature T_e is in Kelvins.

2.1.2.2 Inelastic collisions

Unlike elastic collisions, inelastic collisions can change the identity of the particle. One main assumption is that all particles have no internal degree of freedom. These collisions are very important in the ionospheric region and therefore play a decisive role in the interaction process between non-magnetized planets and the solar wind. They are very closely related to the chemical processes that occur in that region. We first give an overview of the relevant chemical reactions in the ionosphere and describe inelastic collisions for ions and electrons separately.

A) Chemical and mass loading processes The three major mas loading processes in the ionosphere are ionization, charge exchange and recombination (*Szegö et al.*, 2000).

Let us first consider ionization, which is one of the important mass loading process in the ionosphere and contributes significantly to inelastic collisions. It can be either photoionization by solar EUV or impact ionization by photoelectrons, energetic electrons and energetic neutrals. These ionization processes create new charges from the thermal neutral population.

- Photoionization

  Photoionization is the major source of ionization in most ionospheres and occurs when a photon interacts with a neutral and produces and electron-ion pair.

$$S + h\nu \longrightarrow S^+ + e^- \tag{2.28}$$

  The ion S^+ keeps the parent neutral velocity. Since the energy of the ionizing photons usually exceeds the threshold ionization energy, the excess goes either into electron kinetic energy or excitation of the resulting ion. The reason the electrons pick up the bulk of the kinetic energy is that the ions are much more massive than the electrons, and therefore, the ions acquire very little recoil energy during the photoionization process.

- Impact ionization

  Impact ionization can be by photoelectrons, energetic electrons and energetic neutrals. It produces an ion electron pair as well. In the problem we consider here, these ionizations are either small or negligible.

$$S + M(e, ion, neutral) \longrightarrow S^+ + e^- + M(e, ion, neutral) \tag{2.29}$$

- Charge exchange

  Let us consider two particles S and M and the respective ion species S^+ and M^+. A charge exchange reaction transfers an electron from one particle to another:

$$S^+ + M \longrightarrow S + M^+ \tag{2.30}$$

- Ion-atom interchange

In this type of reactions, the nature of both reactants (the ion AB^+ and the atom C) changes and we obtain new products:

$$AB^+ + C \longrightarrow AC^+ + B \tag{2.31}$$

- Recombination

  Last but not least, recombination is an important inelastic collisions process. The most straightforward recombination process is the reverse of photoionization, radiative recombination. An ion species S^+ reacts with an electron e^- in order to produce a neutral S which may be in excited state S^*.

$$S^+ + e^- \longrightarrow S^* + h\nu \tag{2.32}$$

  However, the radiative recombination rate is small and in most cases this is a negligibly slow process.

  Another type of recombination is dissociative recombination and is the dominating ionospheric chemical loss process in Mars and Venus for example. The product atoms A and B may be in an excited state and the excess energy goes to the kinetic energy of the products:

$$S^+ + e^- \longrightarrow A + B \tag{2.33}$$

  Both radiative recombination and dissociative recombination constitute sinks for electrons and ion species s. Finally, we have three-body recombination which is the reverse of impact ionization and is usually negligible in the ionospheric regions.

B) Inelastic collisions for ion species For an ion species s, photoionization and impact ionization are both sources while recombination is a loss process.

$$\Big(\frac{\delta F_s(\mathbf{r},\mathbf{v}_s,t)}{\delta t}\Big)_{ionization} = (\nu_{ph,s'} + \nu_{imp,s'}) n_{s'} f_{s'}(\mathbf{r},\mathbf{v}_s,t) \tag{2.34}$$

$$\Big(\frac{\delta F_s(\mathbf{r},\mathbf{v}_s,t)}{\delta t}\Big)_{recombination} = -\alpha_{R,s} n_e F_s(\mathbf{r},\mathbf{v}_s,t) \tag{2.35}$$

where $\nu_{ph,s'}$ and $\nu_{imp,s'}$ are respectively the photoionization and the total impact ionization frequencies. $n_{s'}$ and $f_{s'}(\mathbf{r},\mathbf{v}_s,t) = F_{s'}(\mathbf{r},\mathbf{v}_s,t)/n_{s'}$ are the density and the normalized distribution function of the neutral species s'. Finally, $\alpha_{R,s}$ is the recombination rate and n_e the total electron density.

As for charge exchange, it will be either a loss or source term for species s depending whether the species is a reactant or a product. In most cases, in a charge exchange reaction, each particle tends to retain its original kinetic energy. Therefore, the phase-space distribution function due to charge exchange of particle changes with the following rate:

$$\Big(\frac{\delta F_s(\mathbf{r},\mathbf{v}_s,t)}{\delta t}\Big)_{chargeexchange} = -\sum_{t'=neutrals} k_{st'} n_{t'} n_s f_s(\mathbf{r},\mathbf{v}_s,t) + \sum_{i=ions} k_{is'} n_i n_{s'} f_{s'}(\mathbf{r},\mathbf{v}_s,t) \tag{2.36}$$

Equation (2.36) shows both loss and source terms. The first term describes the loss of particles s due to charge exchange between ion species s and neutral t' and $k_{st'}$ is the charge exchange rate. The second term is a source term and describes the creation of ions s as a results of charge exchange between neutral s and ion i.

Adding up all the collision terms, we obtain the total rate of change of the ion distribution function due to inelastic collisions:

$$\Big(\frac{\delta F_s(\mathbf{r},\mathbf{v}_s,t)}{\delta t}\Big)_{inelastic} = \Big(\frac{\delta F_s(\mathbf{r},\mathbf{v}_s,t)}{\delta t}\Big)_{ionization} + \Big(\frac{\delta F_s(\mathbf{r},\mathbf{v}_s,t)}{\delta t}\Big)_{recombination} + \Big(\frac{\delta F_s(\mathbf{r},\mathbf{v}_s,t)}{\delta t}\Big)_{chargeexchange} \quad (2.37)$$

$$\Big(\frac{\delta F_s(\mathbf{r},\mathbf{v}_s,t)}{\delta t}\Big)_{inelastic} = \Big(\nu_{ph,s'} + \nu_{imp,s'} + \sum_{i=ions} k_{is'} n_i\Big) n_{s'} f_{s'}(\mathbf{r}.\mathbf{v}_s,t) - \Big(\alpha_{R,s} n_e + \sum_{t'=neutrals} k_{st'} n_{t'}\Big) n_s f_s(\mathbf{r},\mathbf{v}_s,t) \quad (2.38)$$

We can now compute the corresponding transfer integrals for inelastic collisions:

$$m_s\Big(\frac{\delta n_s}{\delta t}\Big) = m_s n_{s'}\Big(\nu_{ph,s'} + \nu_{imp,s'} + \sum_{i=ions} k_{is'} n_i\Big) - m_s n_s\Big(\alpha_{R,s} n_e + \sum_{t'=neutrals} k_{st'} n_{t'}\Big) \quad (2.39)$$

$$\Big(\frac{\delta M_s}{\delta t}\Big)_{inelastic} = m_s n_{s'}\Big(\nu_{ph,s'} + \nu_{imp,s'} + \sum_{i=ions} k_{is'} n_i\Big)(\mathbf{u}_{s0} - \mathbf{u}_s) \quad (2.40)$$

$$\Big(\frac{\delta E_s}{\delta t}\Big)_{inelastic} = \frac{1}{\gamma-1} n_{s'} k T_{s0}\Big(\nu_{ph,s'} + \nu_{imp,s'} + \sum_{i=ions} k_{is'} n_i\Big) + \frac{1}{2} m_s n_{s'}\Big(\nu_{ph,s'} + \nu_{imp,s'} + \sum_{i=ions} k_{is'} n_i\Big)(\mathbf{u}_{s0} - \mathbf{u}_s)^2 - \frac{1}{\gamma-1} n_s k T_s\Big(\alpha_{R,s} n_e + \sum_{t'=neutrals} k_{st'} n_{t'}\Big) \quad (2.41)$$

where $\mathbf{u}_{s0}$ and T_{s0} are the bulk velocity and temperature of neutral species s' respectively. We will assume all neutral species have the same temperature T_n and move with the same bulk velocity $\mathbf{u}_n$. Finally, we can write the production and loss rates of ion species s as S_s and L_s:

$$S_s = m_s n_{s'} \Big(\nu_{ph,s'} + \nu_{imp,s'} + \sum_{i=ions} k_{is'} n_i \Big) \tag{2.42}$$

$$L_s = m_s n_s \Big(\alpha_{R,s} n_e + \sum_{t'=neutrals} k_{st'} n_{t'} \Big) \tag{2.43}$$

which allows us to write the integrals for inelastic collision for ion species s in a more simplified form:

$$m_s \Big(\frac{\delta n_s}{\delta t} \Big) = S_s - L_s \tag{2.44}$$

$$\Big(\frac{\delta M_s}{\delta t} \Big)_{inelastic} = S_s (\mathbf{u}_{s0} - \mathbf{u}_s) \tag{2.45}$$

$$\Big(\frac{\delta E_s}{\delta t} \Big)_{inelastic} = \frac{k}{\gamma - 1} \frac{S_s T_n - L_s T_s}{m_s} + \frac{1}{2} S_s (\mathbf{u}_n - \mathbf{u}_s)^2 \tag{2.46}$$

C) Inelastic collisions for electrons species We can apply the same reasoning we did for ions to electrons in order to evaluate the effect of inelastic collisions on their distribution function. While ionization and recombination affect electrons and ions similarly, charge exchange has no effect on the electrons' distribution function. We then have:

$$\Big(\frac{\delta F_e(\mathbf{r}, \mathbf{v}_e, t)}{\delta t} \Big)_{inelastic} = \Big(\frac{\delta F_e(\mathbf{r}, \mathbf{v}_e, t)}{\delta t} \Big)_{ionization} + \Big(\frac{\delta F_e(\mathbf{r}, \mathbf{v}_e, t)}{\delta t} \Big)_{recombination} \tag{2.47}$$

$$= \sum_{s'} (\nu_{ph,s'} + \nu_{imp,s'}) n_{s'} f_{s'}(\mathbf{r}, \mathbf{v}_e, t) - \sum_{s=ions} \alpha_{R,s} n_s n_e f_e(\mathbf{r}, \mathbf{v}_e, t) \tag{2.48}$$

If we write the production and loss rates of the electrons, S_e and L_e, as:

$$S_e = m_e \sum_{s'} (\nu_{ph,s'} + \nu_{imp,s'}) n_{s'} \tag{2.49}$$

$$L_e = m_e n_e \sum_{s=ions} \alpha_{R,s} n_s \tag{2.50}$$

We can write the simplified form of the integrals for inelastic collisions for electrons:

$$m_s \left(\frac{\delta n_s}{\delta t}\right)_{inelastic} = S_e - L_e \tag{2.51}$$

$$\left(\frac{\delta M_s}{\delta t}\right)_{inelastic} = S_e(\mathbf{u}_n - \mathbf{u}_e) \tag{2.52}$$

$$\left(\frac{\delta E_s}{\delta t}\right)_{inelastic} = \frac{k}{\gamma - 1} \frac{S_e T_n - L_e T_e}{m_e} + \frac{1}{2} S_e (\mathbf{u}_n - \mathbf{u}_e)^2 \tag{2.53}$$

2.1.3 Summary of the Transport Equation

We can now add up elastic and inelastic collisions for both ions and electrons and derive the complete form of the transport equations

Transport equations for ion species Let us define the mass density $\rho_s = m_s n_s$. We then obtain the following transport equations for ion species s:

$$\frac{\partial \rho_s}{\partial t} + \nabla \cdot (\rho_s \mathbf{u}_s) = S_s - L_s \tag{2.54}$$

$$\rho_s \frac{\partial \mathbf{u}_s}{\partial t} + \rho_s(\mathbf{u}_s \cdot \nabla)\mathbf{u}_s + \nabla p_s - \rho_s \mathbf{G} - n_s q_s(\mathbf{E} + \mathbf{u}_s \times \mathbf{B}) = \rho_s \sum_{t=neutrals} \nu_{st}(\mathbf{u}_n - \mathbf{u}_s) + S_s(\mathbf{u}_n - \mathbf{u}_s) \tag{2.55}$$

$$\frac{1}{\gamma - 1}\frac{\partial p_s}{\partial t} + \frac{1}{\gamma - 1}(\mathbf{u}_s \cdot \nabla)p_s + \frac{\gamma}{\gamma - 1}p_s(\nabla \cdot \mathbf{u}_s) + (\nabla \cdot \mathbf{h}_s) = \sum_{t=neutrals} \frac{\rho_s \nu_{st}}{m_s + m_t}[3k(T_n - T_s) + m_t(\mathbf{u}_n - \mathbf{u}_s)^2] + \nu_{se} n_s [3k(T_e - T_s) + m_e(\mathbf{u}_s - \mathbf{u}_e)^2] \frac{k}{\gamma - 1}\frac{S_s T_n - L_s T_s}{m_s} + \frac{1}{2}S_s(\mathbf{u}_n - \mathbf{u}_s)^2 \tag{2.56}$$

Transport equation for electron species We similarly obtain the transport equations for electrons:

$$\frac{\partial \rho_e}{\partial t} + \nabla \cdot (\rho_e \mathbf{u}_e) = S_e - L_e \tag{2.57}$$

$$\rho_e \frac{\partial \mathbf{u}_e}{\partial t} + \rho_e(\mathbf{u}_e \cdot \nabla)\mathbf{u}_e + \nabla p_e - \rho_e \mathbf{G} - n_e q_e(\mathbf{E} + \mathbf{u}_e \times \mathbf{B}) = \rho_e \sum_{t=neutrals} \nu_{et}(\mathbf{u}_n - \mathbf{u}_e) + S_e(\mathbf{u}_n - \mathbf{u}_e) \tag{2.58}$$

$$\frac{1}{\gamma - 1}\frac{\partial p_e}{\partial t} + \frac{1}{\gamma - 1}(\mathbf{u}_e \cdot \nabla)p_e + \frac{\gamma}{\gamma - 1}p_e(\nabla \cdot \mathbf{u}_e) + (\nabla \cdot \mathbf{h}_e) = \sum_{t=neutrals} \frac{\rho_e \nu_{et}}{m_t}[3k(T_n - T_e) + m_t(\mathbf{u}_n - \mathbf{u}_e)^2] \sum_{t=ions} \nu_{et}\frac{m_e}{m_t} n_e [3k(T_t - T_e) + m_t(\mathbf{u}_t - \mathbf{u}_e)^2] \frac{k}{\gamma - 1}\frac{S_e T_n - L_e T_e}{m_e} + \frac{1}{2}S_e(\mathbf{u}_n - \mathbf{u}_e)^2 \tag{2.59}$$

By assuming quasi-neutrality of the plasma, we can then replace the continuity equation by:

$$n_e = \sum_{s=ions} Z_s n_s \tag{2.60}$$

We can directly derive the electron velocity $\mathbf{u}_e$ from the current using Ohm's law:

$$\mathbf{u}_e = \mathbf{u}_+ - \frac{\mathbf{j}}{en_e} \tag{2.61}$$

where $\mathbf{u}_+$ is the charge averaged velocity

$$\mathbf{u}_+ = \sum_{s=ions} \frac{q_s n_s u_s}{en_e} \tag{2.62}$$

s being the ion species and q_s and n_s the respective charge and number densities.

In order to solve the electron transport equations, it is then only necessary to solve the electron energy equation:

$$\begin{aligned} \frac{1}{\gamma-1}\frac{\partial p_e}{\partial t} + \frac{1}{\gamma-1}(\mathbf{u}_e\cdot\nabla)p_e + \frac{\gamma}{\gamma-1}p_e(\nabla\cdot\mathbf{u}_e) + (\nabla\cdot\mathbf{h}_e) = \\ \sum_{t=neutrals} \frac{\rho_e\nu_{et}}{m_t}[3k(T_n-T_e) + m_t(\mathbf{u}_n-\mathbf{u}_e)^2] \\ \sum_{t=ions} \nu_{et}\frac{m_e}{m_t}[3k(T_t-T_e) + m_t(\mathbf{u}_t-\mathbf{u}_e)^2] \\ \frac{k}{\gamma-1}\frac{S_eT_n - L_eT_e}{m_e} + \frac{1}{2}S_e(\mathbf{u}_n-\mathbf{u}_e)^2 \end{aligned} \tag{2.63}$$

We assume $m_e \ll m_s$ and therefore consider electron-ion collisions contribution negligible in the ion and electron momentum equation compared to the other terms. The term $m_e(\mathbf{u}_i - \mathbf{u}_e)^2$ is neglected in the pressure equation in the following calculations since it has a negligible contribution.

In most previous works (*Ma et al.*, 2004; *Glocer et al.*, 2009), the electron pressure is generally assumed to be a fraction of the total pressure $p_e = \alpha\sum_s p_s$. In our calculations, ion and electron pressures are set to be equal. The derivation of the

electron energy equation (Equation 2.63) is still relevant as our next and imminent step is to solve separately for ions and electrons.

2.2 Multi-Fluid MHD Equations

In this section, we derive the multi-ion equations and simplify some of the terms. The electric field **E** can be expressed as a function of the current and ion velocity. We assume that in the electron momentum equation (Equations 2.58), the terms proportional to m_e are negligible compared the rest of the terms, and therefore we obtain from the simplified electron momentum equation:

$$\mathbf{E} = -\frac{\nabla p_e}{e n_e} - \mathbf{u}_e \times \mathbf{B} \tag{2.64}$$

We also know that $\mathbf{u}_e$ is related to the current $\mathbf{j}$ through equation (2.61) and therefore we obtain:

$$\mathbf{E} = -\frac{\nabla p_e}{e n_e} - (\mathbf{u}_+ - \frac{\mathbf{j}}{e n_e}) \times \mathbf{B} \tag{2.65}$$

which can be substituted into the ion momentum equation (Equations 2.55) and re-ordered to obtain the following form of the ion momentum equations :

$$\frac{\partial \rho_s \mathbf{u}_s}{\partial t} + \nabla \cdot (\rho_s \mathbf{u_s} \mathbf{u_s} + I p_s) = n_s q_s (\mathbf{u}_s - \mathbf{u}_+) \times \mathbf{B} + \frac{n_s q_s}{n_e e} (\mathbf{J} \times \mathbf{B} - \nabla p_e) + \mathbf{S}_{\rho_s u_s} \tag{2.66}$$

where $\mathbf{S}_{\rho_s u_s}$ are all the momentum source terms combined. Unlike the single-fluid multispecies case, the multi-fluid equations cannot be written in conservative form because of the term $\frac{n_s q_s}{n_e e}(\mathbf{J} \times \mathbf{B} - \nabla p_e)$.

We can also replace **E** in the Faraday's law

$$\frac{\partial \mathbf{B}}{\partial t} = -(\nabla \times \mathbf{E}) \tag{2.67}$$

in order to obtain the induction equation:

$$\frac{\partial \mathbf{B}}{\partial t} - \nabla \times (\mathbf{u}_e \times \mathbf{B} + \frac{\nabla p_e}{n_e}) = 0 \tag{2.68}$$

In most cases, $\mathbf{u}_e$ is replaced by $\mathbf{u}_+$ as it is considered dominant compared to the Hall term $\frac{\mathbf{j}}{en_e}$. It is then assumed that the relative motion of electrons with respect to the averaged ion motion is much smaller than $\mathbf{u}_+$. This simplifies the induction equation to:

$$\frac{\partial B}{\partial t} - \nabla \times (\mathbf{u}_+ \times \mathbf{B}) = 0 \tag{2.69}$$

However, in cases where the ion gyroradius becomes comparable to the body's radius, the Hall effect is not negligible and we need to include it (see Chapter 4). The details of the implementation of the Hall effect can be found in (*Ma et al.*, 2007; *Tóth et al.*, 2008)

We also neglect heat conduction for the time being for the sake of simplification.

Finally, since we are setting the ion and electron pressures to be equal, we will not consider ion-electron and electron neutral collision terms and the electron energy source terms will be accounted for in the individual ion energy equations.

The final form of multi-fluid MHD equations that we are solving in our study:

$$\frac{\partial \rho_s}{\partial t} + \nabla \cdot (\rho_s \mathbf{u}_s) = S_s - L_s \tag{2.70}$$

$$\begin{aligned}\frac{\partial \rho_s \mathbf{u}_s}{\partial t} + \nabla \cdot (\rho_s \mathbf{u_s} \mathbf{u_s} + I p_s) &= n_s q_s (\mathbf{u}_s - \mathbf{u}_+) \times \mathbf{B} + \frac{n_s q_s}{n_e e}(\mathbf{J} \times \mathbf{B} - \nabla p_e) \\ &+ \rho_s \sum_{t=neutrals} \nu_{st}(\mathbf{u}_n - \mathbf{u}_s) + S_s(\mathbf{u}_n - \mathbf{u}_s)\end{aligned} \tag{2.71}$$

$$\begin{aligned}\frac{1}{\gamma - 1}\frac{\partial p_s}{\partial t} + \frac{1}{\gamma - 1}(\mathbf{u}_s \cdot \nabla) p_s &= -\frac{\gamma}{\gamma - 1} p_s (\nabla \cdot \mathbf{u}_s) \\ &+ \sum_{t=neutrals} \frac{\rho_s \nu_{st}}{m_s + m_t}[3k(T_n - T_s) + m_t(\mathbf{u}_n - \mathbf{u}_s)^2] \\ &+ \frac{k}{\gamma - 1}\frac{S_s T_n - L_s T_s}{m_s} + \frac{1}{2} S_s (\mathbf{u}_n - \mathbf{u}_s)^2 \\ &+ \frac{n_s}{n_e}\frac{k}{\gamma - 1}\frac{S_e T_n - L_e T_e}{m_e}\end{aligned} \tag{2.72}$$

$$\frac{\partial B}{\partial t} - \nabla \times (\mathbf{u}_+ \times \mathbf{B}) = 0 \tag{2.73}$$

with

$$S_s = m_s n_{s'} \Big(\nu_{ph,s'} + \nu_{imp,s'} + \sum_{i=ions} k_{is'} n_i \Big) \tag{2.74}$$

$$L_s = m_s n_s \Big(\alpha_{R,s} n_e + \sum_{t'=neutrals} k_{st'} n_{t'} \Big) \tag{2.75}$$

$$S_e = m_e \sum_{s'} (\nu_{ph,s'} + \nu_{imp,s'}) n_{s'} \tag{2.76}$$

$$L_e = m_e n_e \sum_{s=ions} \alpha_{R,s} n_s \tag{2.77}$$

CHAPTER III

Numerical Model

3.1 Introduction

The multi-fluid equations we just derived in Chapter 2 cannot be solved analytically, given their complicated nature. We therefore solve them numerically using a modified version of the Block Adaptive Tree Solar Wind Roe-Type Upwind Scheme (BATS-R-US). BATS-R-US has been developed since 1996 at University of Michigan (*Groth et al.*, 1999; *Powell et al.*, 1999; *Hansen*, 2001; *Powell et al.*, 2006). It is a highly scalable, massively parallel code using a block based adaptive mesh refinement (Block-AMR) algorithm. The code applies a second-order Godounov-type, finite volume upwind scheme which can solve hyperbolic problems and obtain accurate solutions. This family of numerical schemes also ensures stability as well as the absence of oscillations near sharp gradients, like shock waves. A detailed description of the approach can be found in (*Powell et al.*, 1999; *Tóth et al.*, 2011). The BATS-R-US code has been extensively and successfully used to study the environment of various solar system bodies.

In this chapter, we will discuss important aspects of the numerical scheme used in our simulations and address questions that are relevant to the multi-fluid calculations.

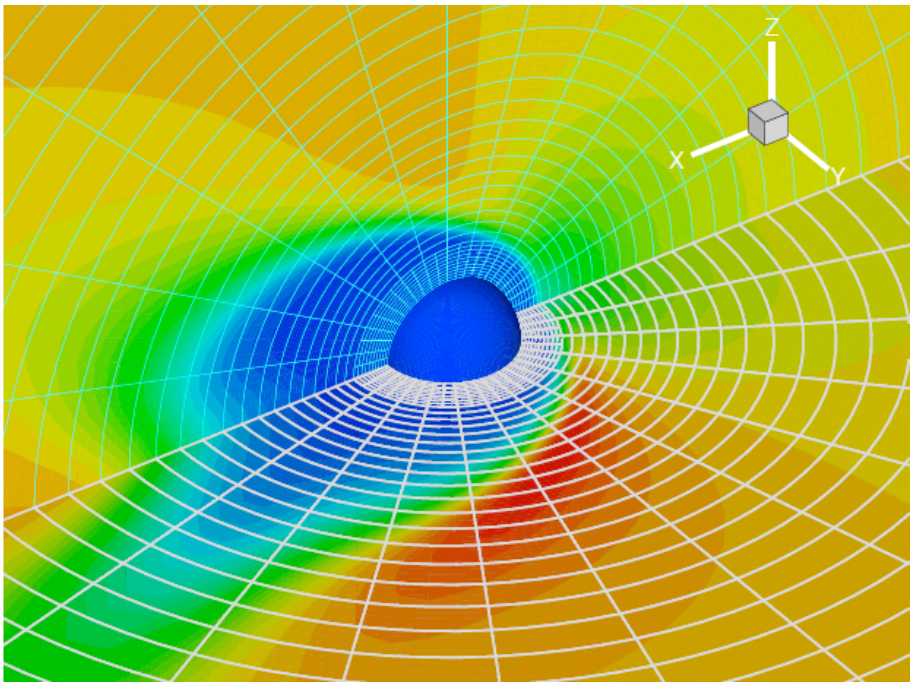

Figure 3.1: Example of a spherical grid (*Ma*, 2006)

3.2 Grid structure: spherical adaptive grid

In our model, we use a block based, adaptive spherical grid. The grid is generated by dividing the computational domain into many blocks, each of them containing the same number of cells (anywhere between $4 \times 4 \times 4$ and $12 \times 12 \times 12$). The block sizes can be different in terms of the volume of physical space they occupy. The main advantages of having a block-based tree data structure is the ease with which the grid can be adapted and the ease of parallelization (*Powell et al.*, 1999).

The streched spherical coordinate system uses the natural logarithm of the radial coordinate, r, and the two other spherical coordinates θ and ϕ. While a Cartesian grid has been used for Mars in the past (*Ma et al.*, 2002) a spherical grid has the advantage of achieving a much better altitude resolution without exhausting computational resources by using an exhaustive number of cells. In the case of Mars and Venus, we were able to have cell sizes as small as 10 km in the ionospheric region, using a spherical grid.

The use of an adaptive grid is very convenient, especially in problems where we need a high resolution (and therefore a refined grid) in regions of interest (ionospheric regions for example) and at the same time, we have other regions of less interest, where a coarse grid can be used instead, to save time and computational resources.

One of the most effective techniques to use computational resources optimally is the Adaptive Mesh Refinement (AMR) technique. It considers each grid block as a node of the tree. The root of the tree are coarse blocks covering the entire solution domain. In regions we want to refine, a "parent block" is divided into eight "children" block. Each of these eight octants becomes a new block having the same number of cells as the parent, and its cell size (Δlnr, $\Delta\theta$, $\Delta\phi$) are each halved from their value on the "parent block". The "children" blocks can be in turn refined and so on. At the end, we obtain a tree of successively finer blocks until we reach the cell-size that we want in the region of interest. In Figure 3.2, we can see a hierarchical multi-root data structure with two refinement levels. While we have dynamic adaptive mesh refinement as an option in our code, we decided to refine our code in spherical regions that we set manually: one that captures the ionospheric region and one that captures the bow shock (Figure 3.3)

A more comprehensive description of Adaptive Mesh Refinement in BATS-R-US and the implementation of the new Block Adaptive Tree Library, BATL can be found in *Tóth et al.* (2011).

3.3 Finite volume discretization

We use in our model a finite volume, total variation diminishing (TVD) type discretization with a second order minmod limiter to solve the governing equations. The physical domain is divided into smaller volumes where each of the variables are calculated. This method solves the integral form of the equations and therefore allows us to solve conservation laws for discontinuous problems (such as shocks).

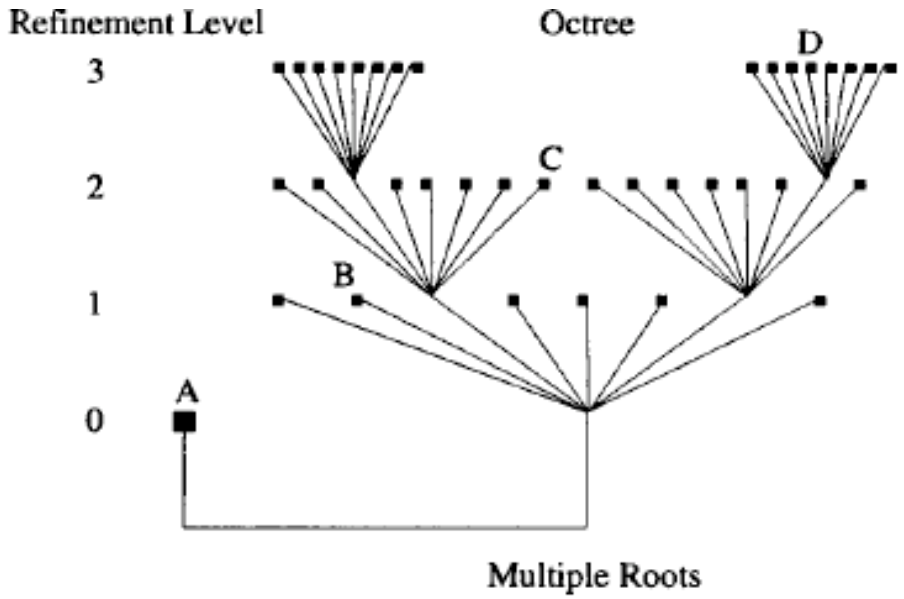

Figure 3.2: A hierarchial multi-root octree data structure (*Groth et al.*, 1999).

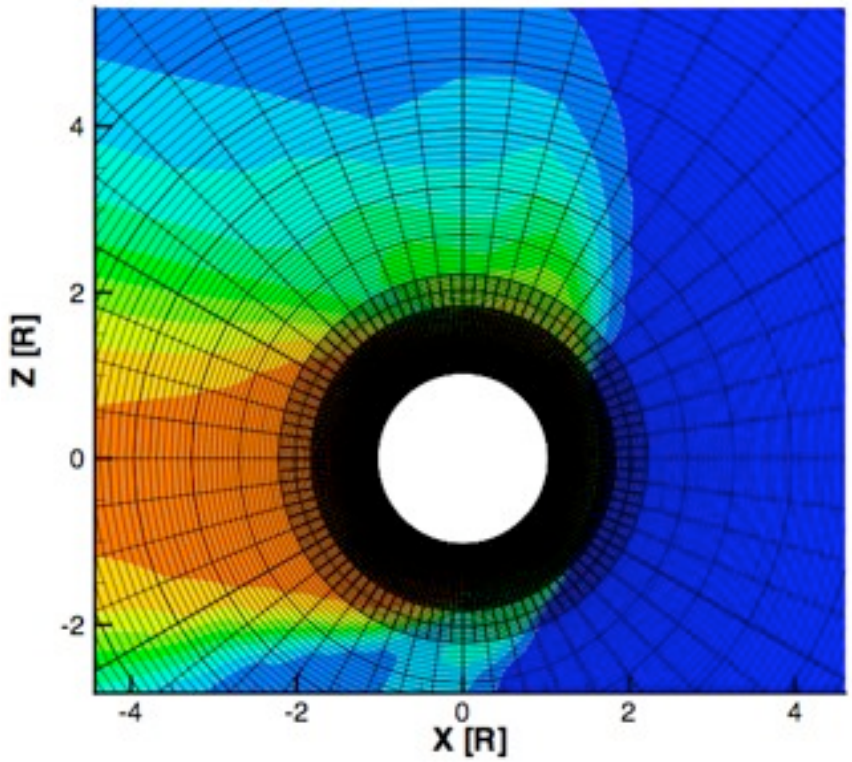

Figure 3.3: The spherical grid for Mars simulations showing the two-refinement levels

As we saw in Chapter 2, the multi-fluid MHD equations can be written in the following form:

$$\frac{\partial \mathbf{W}}{\partial t} + (\nabla \cdot \mathbf{F})^T = \mathbf{S} \tag{3.1}$$

where $\mathbf{W}$ is the state vector of conserved quantities, $\mathbf{F}$ is a flux tensor and $\mathbf{S}$ is a source vector, containing the terms that can not be expressed in divergence form. These terms can be gravity, the Lorentz force or the electron pressure gradient term in the multi-fluid momentum equations, for example.

We integrate the equations over the volume of a cell i, in the grid:

$$\int\limits_{cell_i} \frac{\partial \mathbf{W}}{\partial t} dV + \int\limits_{cell_i} \nabla \cdot \mathbf{F} dV = \int\limits_{cell_i} \mathbf{S} dV \tag{3.2}$$

Using the divergence theorem, we can rewrite equation 3.2 as follows:

$$\frac{d\mathbf{W}_i}{dt} + \frac{1}{V_i} \oint\limits_{cell_i} \mathbf{F} \cdot \hat{\mathbf{n}} dA = \mathbf{S}_i \tag{3.3}$$

where V_i is the cell volume, $\mathbf{W}_i$ is the cell-averaged conserved state and $\mathbf{S}$ the cell-averaged source vector. $\hat{\mathbf{n}}$ is a unit normal vector, pointing outward from the boundary of the cell i.

The surface integral in equation 3.3 can be evaluated by summing up the fluxes at the surfaces of each finite volume considered in the calculation as in equation 3.4. The term $\mathbf{F} \cdot \hat{\mathbf{n}}$ is evaluated at the center of the cell faces

$$\frac{d\mathbf{W}_i}{dt} + \frac{1}{V_i} \sum_{faces} \mathbf{F} \cdot \hat{\mathbf{n}} dA = \mathbf{S}_i \tag{3.4}$$

The finite volume method has many advantages. It allows us to conserve quantities in a given volume. It also allows for unstructured meshes; in the case of a spherical grid, this means we can still express the physical vectors, such as $\mathbf{u}$ and $\mathbf{B}$, in Cartesian

coordinates, since only the grid mesh positions are defined in spherical coordinates.

3.4 Linde Solver

There are several algorithms to calculate the flux at the cell interfaces in equation 3.4. It is a classic problem, the Riemann problem, where we need to find the solution of the hyperbolic system of equations with piece-wise constant initial conditions. In our multi-fluid model simulations, we use the Linde solver (*Linde*, 1998), based on the HLL solver devised by Harten, Lax and van Leer (*Harten et al.*, 1983). Using the Linde solver, the numerical flux can be calculated as :

$$\mathbf{F}\cdot\hat{\mathbf{n}}(\mathbf{W}_L,\mathbf{W}_R)=\frac{\lambda_R\cdot\mathbf{F}(\mathbf{W}_L)\cdot\hat{\mathbf{n}}+\lambda_L\cdot\mathbf{F}(\mathbf{W}_R)\cdot\hat{\mathbf{n}}}{\lambda_R-\lambda_L}+\frac{\lambda_R\cdot\lambda_L}{\lambda_R-\lambda_L}(\mathbf{W}_R-\mathbf{W}_L) \quad (3.5)$$

where $\lambda_R \geq 0$ and $\lambda_L \leq 0$ are respectively the eigenvalues corresponding to the fastest right-going and fastest left going waves.

The Linde solver is directly applicable to the MHD problems and has proven to be more efficient and robust than other solvers in solving the multi-fluid equations in our applications.

3.5 Time-stepping

3.5.1 Local time stepping towards steady-state solution

Convergence towards steady state can be greatly accelerated by employing different local time steps in every grid cell. The local time-step is limited by the local stability conditions only. By taking the maximum possible time step (in an explicit time stepping scheme), the residual can propagate through the computational domain in fewer iterations (*Tóth et al.*, 2011). Formally the scheme can be written as

$$\mathbf{U}_i^{n+1} = \mathbf{U}_i^n + \Delta t_i \mathbf{R}_i(\mathbf{U}^n) \tag{3.6}$$

where $\mathbf{U}$ is the vector of state variables, $\mathbf{R}_i$ is the discretized right hand side of the partial differential equation $\frac{\partial U}{\partial t} = R(U)$, and Δt_i is the time step for grid cell i. The superscripts n and n+1 indicate the current and next time levels, respectively. When we reach steady state, $\mathbf{U}_i^{n+1} = \mathbf{U}_i^n$, so that R_i becomes zero irrespective of the value of Δt_i. This means that the discrete steady-state solution is consistent with the PDE.

For the MHD equations the situation is a bit more complicated. The variation of the time step from cell-to-cell corresponds to a space dependent factor α in front of the time derivative. The discrete induction equation is therefore consistent with the following PDE:

$$\alpha \frac{\partial \mathbf{B}}{\partial t} = -\nabla \times \mathbf{E} \tag{3.7}$$

Let us take the divergence of this equation:

$$\nabla\alpha \cdot \frac{\partial \mathbf{B}}{\partial t} + \alpha \frac{\partial \nabla \cdot \mathbf{B}}{\partial t} = 0 \tag{3.8}$$

It is clear that $\nabla \cdot \mathbf{B}$ is not conserved if $\nabla\alpha$ is not zero. The divergence-free condition depends on the initial condition only, therefore, the local time stepping will lead to a steady state solution that has non-zero $\nabla \cdot \mathbf{B}$ unless we do something about it. We can introduce modifications to the induction equation so that the divergence free condition depens on the boundary conditions and not on the initial conditions. We will discuss this issue in section 3.6.

We used local time-stepping in our Mars and Venus simulations and it allowed us to reach a converged solution in a reasonable time.

3.5.2 Point-implicit scheme

The source terms in our multi-fluid equations can become stiff, which would require very small explicit time steps in order to achieve stability. BATS-R-US offers various time-stepping algorithms that allow us to take much larger time steps: point-implicit, semi-implicit and fully implicit time discretization schemes (*Tóth et al.*, 2011). We will only describe here the point implicit scheme that we are using in our simulations. We only apply the point-implicit scheme within 5 R (Mars and Venus radii) since we know that source terms are negligible beyond this point.

The point implicit scheme can be used when the stiff source terms in our equations depend on the local information only (and not on the spatial derivatives). These terms can be chemical reactions, recombination, photo-ionization, collisional terms, and terms proportional to $(\mathbf{u}_s - \mathbf{u}_+)$ in the multi-ion MHD equations. The point-implicit scheme allows us to address the stability problem while taking large time steps.

Applying the point-implicit scheme occurs in two steps: first, we do an explicit update without the stiff source terms. This can be done in one stage:

$$\mathbf{U}^* = \mathbf{U}^n + \Delta t \mathbf{R}_{expl}(U^n) \tag{3.9}$$

or two stages (which is more stable for higher CFL numbers):

$$\mathbf{U}^{n+\frac{1}{2}} = \mathbf{U}^n + \frac{\Delta t}{2}\mathbf{R}_{expl}(U^n) \tag{3.10}$$

$$\mathbf{U}^* = \mathbf{U}^n + \Delta t \mathbf{R}_{expl}(U^{n+\frac{1}{2}}) \tag{3.11}$$

where $\mathbf{R}_{expl}$ is the non-stiff part of the right hand side.

We add next the stiff source term $\mathbf{S}_{impl}^{n+1}$ to the $\mathbf{U}_{impl}$ set of variables that are

affected by S_{impl} (and $\mathbf{U}_{expl}$ denotes the rest of the variables):

$$\mathbf{U}_{impl}^{n+1} = \mathbf{U}_{impl}^{*} + \Delta t \mathbf{S}_{impl}(\mathbf{U}_{expl}^{n}, U_{impl}^{n+1}) \tag{3.12}$$

This can be linearized around time level n:

$$\mathbf{U}_{impl}^{n+1} = \mathbf{U}_{impl}^{*} + \Delta t \mathbf{S}_{impl}(U^{n}) + \Delta t \frac{\partial \mathbf{S}_{impl}}{\partial \mathbf{U}_{impl}} \cdot (\mathbf{U}_{impl}^{n+1} - \mathbf{U}_{impl}^{n}) \tag{3.13}$$

Note that we have two terms in Equation 3.13 that are evaluated at time level n+1. We can solve the equation for $\mathbf{U}_{impl}^{n+1}$ by inverting an $N_{impl} \times N_{impl}$ matrix, where N_{impl} is the number of implicit variables. In our case, we solve point-implicitly for the individual densities ρ_s, individual momenta $\rho_s \mathbf{u}_s$ and individual pressures p_s. The rest of the variables are treated explicitly ($\mathbf{U}_{expl}^{n+1} = \mathbf{U}_{expl}^{*}$).

As for the Jacobian matrix $\frac{\partial \mathbf{S}_{impl}}{\partial \mathbf{U}_{impl}}$, it can be calculated numerically as

$$\frac{\partial S_{impl,v}}{\partial U_{impl,w}} = \frac{S_{impl,v}(\mathbf{U}^{n} + \delta_w \epsilon_w) - S_{impl,v}(\mathbf{U}^{n})}{\epsilon_w} \tag{3.14}$$

where v and w are indexes 1....N_{impl} of the implicit variables, δ_w is an array with all zeros except for a single one corresponding to w-th implicit variable. Finally ϵ_w is a small perturbation for variable w:

$$\epsilon_w = \epsilon |U_{impl,w}| + \chi_w \tag{3.15}$$

where ϵ is the square root of the machine precision of real numbers and χ_w is a very small positive number relative to the typical values of $|U_{impl,w}|$, which is needed to avoid division by zero if $U_{impl,w}$ happens to be zero in a grid cell.

We also implemented a second order in ϵ_w algorithm to compute $\frac{\partial \mathbf{S}_{impl}}{\partial \mathbf{U}_{impl}}$, which proved to be useful for the multi-fluid case:

$$\frac{\partial S_{impl,v}}{\partial U_{impl,w}} = \frac{S_{impl,v}(\mathbf{U}^n + \delta_w \epsilon_w) - S_{impl,v}(\mathbf{U}^n - \delta_w \epsilon_w)}{2\epsilon_w} \tag{3.16}$$

As we can see in equation 3.16 , the original state (at $t = t_n$) is perturbed symmetrically in both directions.

3.6 Divergence of B control

When solving numerically for the MHD equations, the divergence-free constraint, $\nabla \cdot \mathbf{B} = 0$ still has to be respected and imposed upon the numerically solved magnetic field. There are several methods to address the $\nabla \cdot \mathbf{B} = 0$ issue. A possible way is using the projection method (e.g., *Ramshaw*, 1983; *Vignes*, 1989; *Tanaka*, 1993). After each time-step, $\mathbf{B}^*$ is replaced by a new field $\mathbf{B}$ that is given as:

$$\mathbf{B} = \mathbf{B}^* - \nabla\phi \tag{3.17}$$

$$\nabla^2\phi = \nabla \cdot \mathbf{B} \tag{3.18}$$

In our calculation, we use an alternative approach, the 8-wave scheme proposed by *Godunov* (1959) and *Powell* (1994). In this scheme, instead of dropping the terms including $\nabla \cdot \mathbf{B}$, because of the absence of magnetic monopole, we keep them in the derivation and solve our MHD equations with an additional source vector term, proportional to $\nabla \cdot \mathbf{B}$ in the induction equation.

$$\frac{\partial \mathbf{B}}{\partial t} + (\nabla \times \mathbf{E}) = -u\nabla \cdot \mathbf{B} \tag{3.19}$$

When using the local time stepping, the time step varies from cell to cell corresponding to a space dependent factor α in front of the time derivative (cf. Equation 3.7). Therefore, Equation 3.19 becomes:

$$\alpha\frac{\partial \mathbf{B}}{\partial t} + (\nabla \times \mathbf{E}) = -u\nabla \cdot \mathbf{B} \tag{3.20}$$

$$\nabla\alpha\frac{\partial \mathbf{B}}{\partial t} + \alpha\frac{\partial \nabla \cdot \mathbf{B}}{\partial t} = -\nabla \cdot (u\nabla \cdot \mathbf{B}) \tag{3.21}$$

so that $\nabla \cdot (u\nabla \cdot \mathbf{B}) = 0$ in steady state while $\nabla \cdot \mathbf{B} = 0$ at the boundaries. This means that the numerical zero $\nabla \cdot \mathbf{B}$ is propagated from the boundaries together with the flow to the entire computational domain, so that $\nabla \cdot \mathbf{B} = 0$ will be zero to the truncation error (*Tóth et al.*, 2011).

In summary, the 8-wave scheme method has the advantage of being simple, inexpensive and robust.

3.7 Conservation

It is essential to use a conservative discretization to capture shocks correctly. Unfortunately, the multi-ion MHD equations cannot be written in conservative form, therefore a conservative discretization is not possible. However, we can solve the multi-ion energy equations conservatively in the hydrodynamic limit, when the magnetic energy density and ∇p_e are small relative to the kinetic and thermal terms. We therefore solve for the hydrodynamic energy density e_s given by $e_s = \rho_s \mathbf{u}_s^2/2 + p_s/(\gamma - 1)$ as

$$\frac{\partial e_s}{\partial t} + \nabla \cdot [(e_s + p_s)\mathbf{u_s}] = \mathbf{u_s} \cdot \left[\frac{n_s q_s}{n_e e}(\mathbf{J} \times \mathbf{B} - \nabla p_e) + n_s q_s(\mathbf{u_s} - u_+) \times \mathbf{B}\right] + S_{e_s} \tag{3.22}$$

where S_{e_s} is the energy source term. We apply the conservative discretization outside and around the bow shock (we limit the region between non-conservative and conservative regions with a parabola; in Mars' case, the parabola is within a radius of 1.4 R_M in the subsolar direction).

3.8 Testing and code development

The major challenge that we faced while developing our code has been the "testing" part. It is easy to write lines of code, sometimes it is even easier to obtain results that look"ok", however, the main challenge is to understand why the code gives certain results, in other words, understand whether these results are physically meaningful. A way to check this is to apply the code to a simpler problem: a two-fluid shock tube, a simple sound wave, or what we call the pseudo multi fluid problem. These checks are essential to validate our model and in order to discover issues that we wouldn't be able to track in a more complex code.

3.8.1 Breaking down the problem: shocktube, sound wave, pseudo multi-fluid

Before adding a new component to our code (extra fluid, conservative scheme, electron pressure), we decide to apply it first to a simpler problem that would be easier to investigate. Our strategy had been to first run a simple two-fluid shocktube case and a two-fluid sound wave case. We also ran these cases with and without the total MHD fluid. The variables of the MHD fluid correspond to the sum of the variables of the individual fluid (density, momenta, pressure). These case studies proved to be very helpful in debugging our code efficiently and rapidly. Some of the results of our test cases are shown in Figures 3.4 and 3.5.

Another very efficient way of testing our code has been what we call the "pseudo multi-fluid" run, where we run our multi-fluid code, but overwrite the individual velocities and temperatures and set them to be equal: $u_i = u$ and $T_i = T$. The results of the pseudo multi-fluid runs are expected to be identical to the single fluid multi-species results (*Ma et al.*, 2004). This test is based on the fact that the single fluid multi-species MHD code has been extensively tested and has given very good results that compare very well to observations (*Ma et al.*, 2004). Figure 3.6 shows an exam-

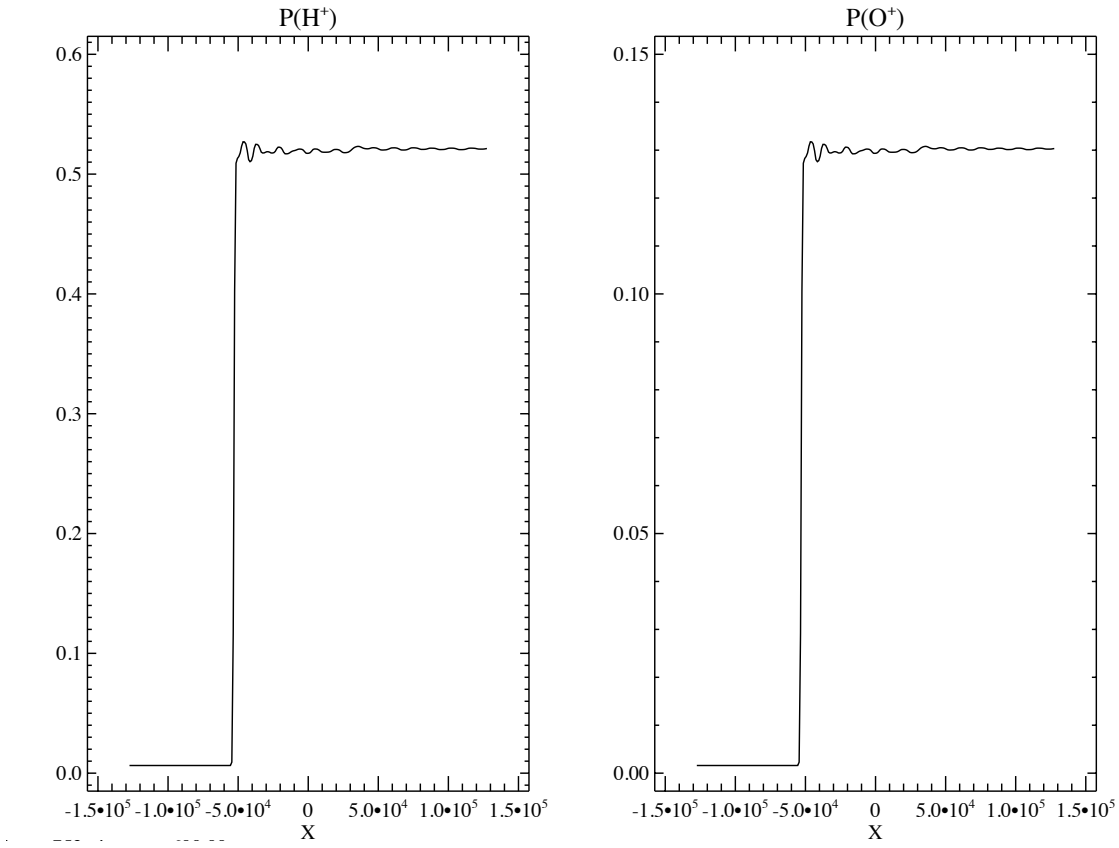

Figure 3.4: An example of a two fluid shocktube case run: hydrogen and oxygen pressures (in nPa) as a function of distance (in km)

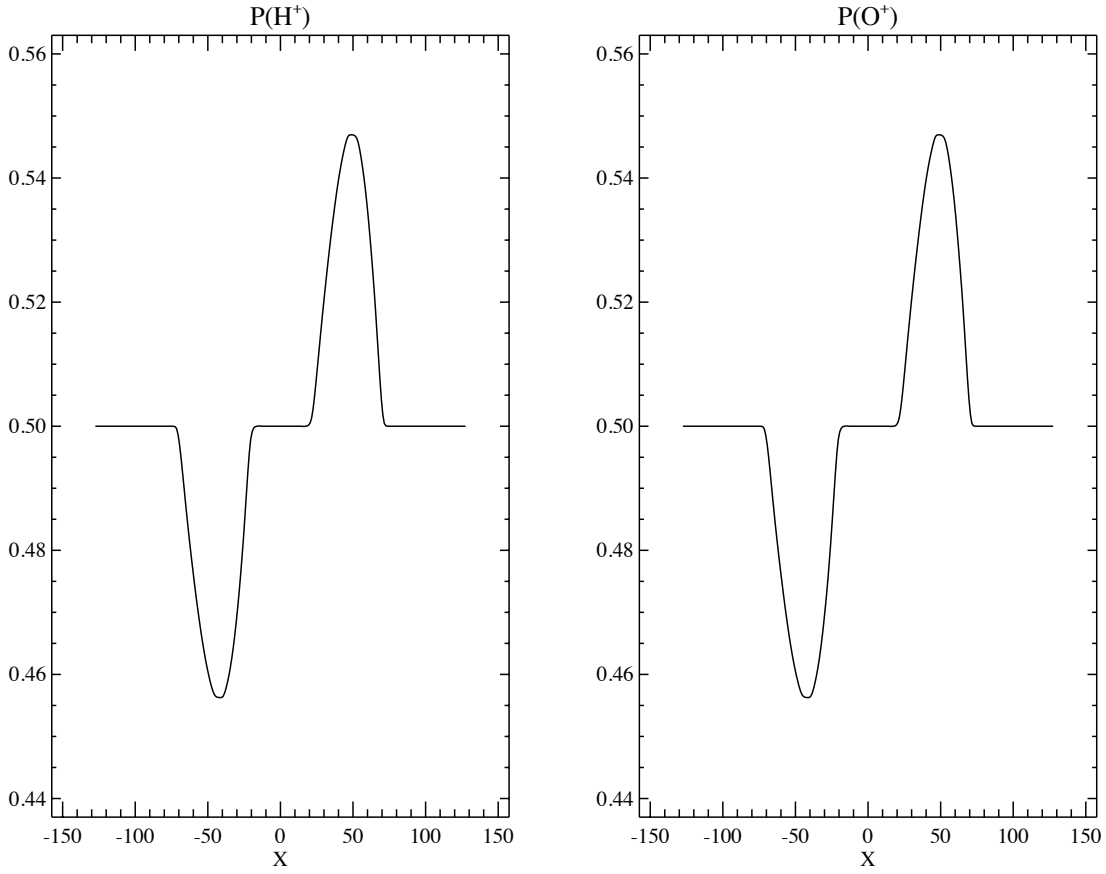

Figure 3.5: An example of a two fluid sound wave case run: hydrogen and oxygen pressures (in nPa) as a function of distance (in km)

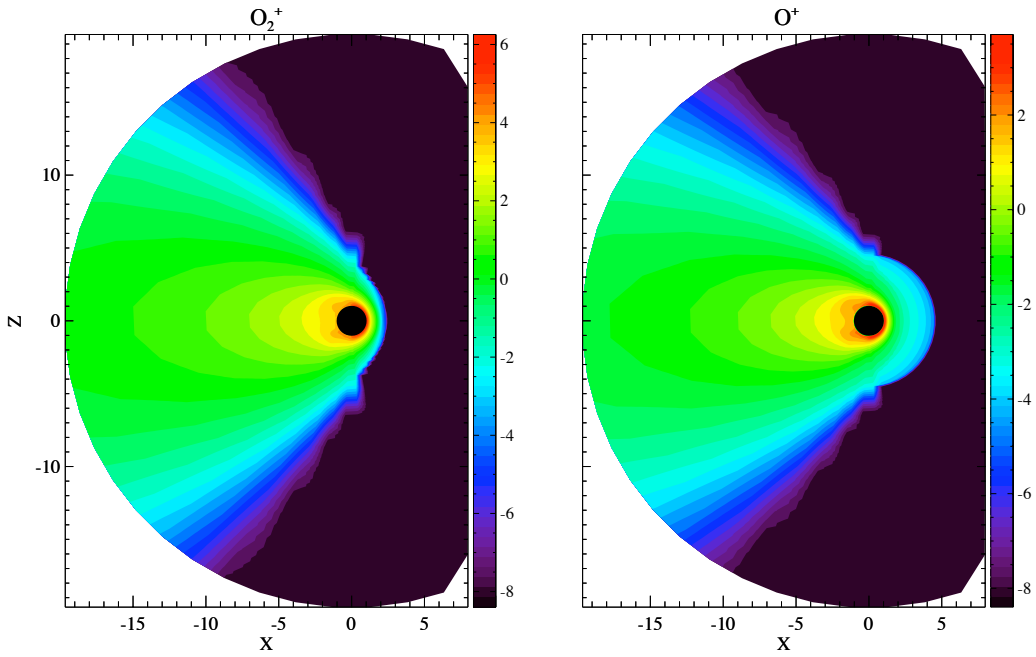

Figure 3.6: Mass densities of O_2^+ and O^+ in amu/cc for a Pseudo multi-fluid test run

ple of converged pseudo multi-fluid run while Figure 3.7 shows a direct comparison between the pseudo multi-fluid and the single fluid cases for a short run, including the electron pressure. In fact, the comparison between the pseudo multi-fluid and single fluid enabled us to find a bug in the electron-neutral collision rates as they were turning negative when the temperature was too small. This was happening in particular for hydrogen's interaction with electrons where the collision term is proportional to $(1 - 1.35 \times 10^{-4} T_e)$. This term can turn negative as soon as T_e is greater than a few thousand Kelvins, therefore we set an upper limit at $T_e = 5000K$ which allows us to avoid the problem.

Another advantage of using the pseudo multi-fluid has been to better understand the evolution of the "real" multi-fluid model as it is much easier to compare two models that have the same structure and the same number of variables. The difference is that in the multi-fluid model the velocities and temperatures can evolve indepen-

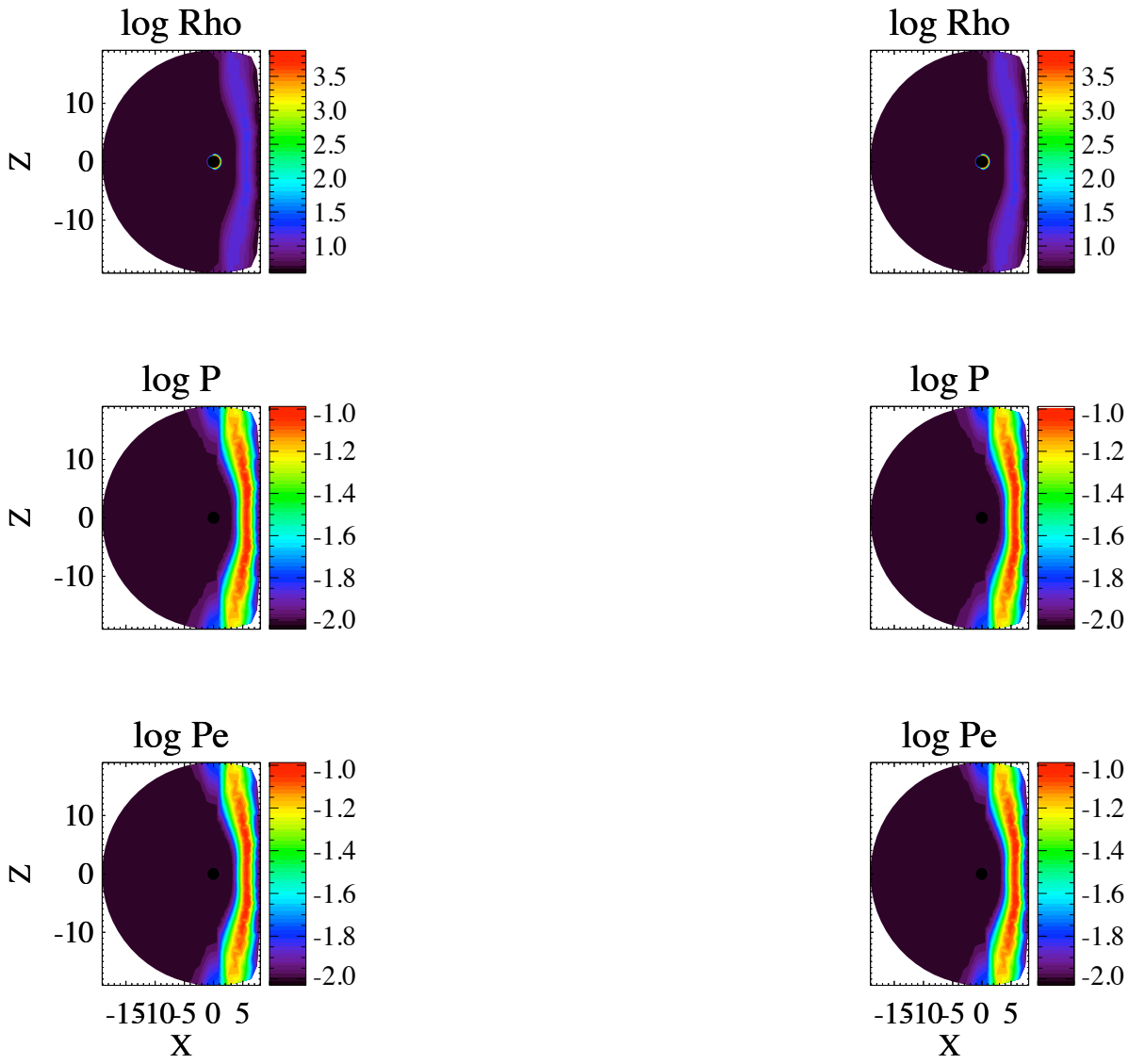

Figure 3.7: Simulation results (from top to bottom: density, ion pressure, electron pressure) for single fluid (right) and pseudo multi-fluid (left) runs after the first 20 iterations

dently. Now, if for example, a quantity X_i for the fluid i is orders of magnitude higher or lower than the same quantity for the other fluids, it is much simpler to run the pseudo multi-fluid until convergence and restart with the real multi-fluid and observe what causes the quantity X_i to deviate.

3.8.2 Positivity

In the case of Mars and Venus, the most important numerical challenge has been to maintain the positivity of pressure and density of all ion fluids. In the regions upstream of the body where the plasma consists essentially only of solar wind protons, the ionospheric ion densities are initialized to very small values (a fraction of the total density $\sim 10^{-9}$), while velocity and temperature are set to the same value as the total fluid, in order to avoid zeros and associated problems. The issue of positivity also arises when implementing a conservative scheme. The comparative runs between the pseudo multi-fluid and the real multi-fluid showed that we may obtain negative values for the thermal pressure when we compute it by substracting the kinetic energy from the total hydrodynamic energy. In order to solve this problem, we check the pressures at every time step and if it is negative we overwrite it by a very small fraction of the total pressure.

3.8.3 Code performance

Finally, it is important to provide an idea about our code performance. Our code uses 8000 CPU hours to converge in a steady state mode (roughly 12 hours on 600 cores using Pleiades supercomputers, we can therefore have a converged run overnight). It uses 12 million cells, the smallest cell size being equal to 10 km in the radial direction. We use a Courant-Friedrichs-Lewy (CFL) number of 0.2 for the first 10000 iterations to avoid instabilities, then we switch to a 0.8 CFL number in the later stage.

CHAPTER IV

Multi-fluid model of Mars' interaction with the solar wind

Introduction

Our newly developed 3D, multi-fluid, MHD model is used to study the interaction of the solar wind with Mars. This model is based on the BATS-R-US code, using a spherical grid and a radial resolution equal to 10 km in the ionospheric regions. We solve separate continuity, momentum and energy equations for each ion fluid and run our model for both solar minimum and maximum conditions. We obtain asymmetric densities, velocities and magnetic pile up in the X-Z plane. These asymmetries are the result of the decoupling of the individual ions; therefore our model is able to account for the respective dynamics of the ions and show new physical processes that could not be observed by the single fluid model. Our results are consistent with the measured bow shock and MPB locations and with the Viking observed ion densities. We also compute the escape fluxes for both solar minimum and solar maximum conditions and compare them to the single fluid results and the observed values from Mars Express.

4.1 Physical Model and simulation details

Our previous multi-species model had continuity equations for all the ions, but only one momentum and one energy equation. In the case of multi-fluid formulation, we have separate mass, momentum and energy equations for the four fluids H^+, O_2^+, O^+, CO_2^+. The multi-ion MHD equations can be written in non-conservative form only and they are as follows:

$$\frac{\partial \rho_s}{\partial t} + \nabla \cdot (\rho_s \mathbf{u}_s) = S_{\rho_s} \tag{4.1}$$

$$\frac{\partial \rho_s \mathbf{u}_s}{\partial t} + \nabla \cdot (\rho_s \mathbf{u_s} \mathbf{u_s} + I p_s) = n_s q_s (\mathbf{u}_s - \mathbf{u}_+) \times \mathbf{B} + \frac{n_s q_s}{n_e e} (\mathbf{J} \times \mathbf{B} - \nabla p_e) + S_{\rho_s u_s} \tag{4.2}$$

$$\frac{\partial p_s}{\partial t} + (\mathbf{u}_s \cdot \nabla) p_s = -\gamma p_s (\nabla \cdot \mathbf{u}_s) + S_{p_s} \tag{4.3}$$

$$\frac{\partial B}{\partial t} - \nabla \times (\mathbf{u}_+ \times \mathbf{B}) = 0 \tag{4.4}$$

where ρ_s, n_s, q_s, $\mathbf{u}_s$ and p_s are respectively the individual mass density, number density, charge, velocity and pressure of the ion s. $\mathbf{B}$ is the magnetic field, $\mathbf{J}$ is the current density, $\mathbf{I}$ is the identity matrix, e is the electric charge and γ is the ratio of specific heats (and taken to be $\frac{5}{3}$).

The electron number density n_e can be calculated from charge neutrality as

$$n_e = \frac{1}{e} \sum_s n_s q_s \tag{4.5}$$

The charge averaged ion velocity u^+ is:

$$\mathbf{u}_+ = \frac{\sum_s n_s q_s \mathbf{u}_s}{e n_e} \tag{4.6}$$

The electron pressure gradient term in the momentum equation is taken to be equal to the total ion pressure gradient.

As for the source terms S_{ρ_s}, the mass density source term, $S_{\rho_s u_s}$, the momentum source term and S_{p_s}, the pressure source term, they contain charge exchange, photoionization, recombination, ion-neutral and ion-ion collisions:

$$S_{\rho_s} = S_s - L_s \tag{4.7}$$

$$S_{\rho_s u_s} = \rho_s g - \rho_s \sum_{t=neutrals} \nu_{st}(u_n - u_s) + S_s u_n - L_s u_s \tag{4.8}$$

$$\begin{aligned} S_{p_s} \;=\; & (\gamma - 1)\Big(2 \sum_{t=neutrals} \nu_{st} \frac{m_s}{m_s + m_t} n_s k (T_n - T_s) + 2 \sum_{t=ions} \nu_{st} \frac{m_s}{m_s + m_t} n_s k (T_t - T_s) \\ & + \frac{2}{3} \sum_{t=neutrals} \nu_{st} \frac{m_s m_t}{m_s + m_t} n_s (u_n - u_s)^2 + k \frac{S_s T_n - L_s T_s}{m_s} + \frac{1}{3} S_s (u_n - u_s) + \frac{n_s}{n_e} S_{p_e} \Big) \end{aligned} \tag{4.9}$$

with S_s and L_s, the production and loss rate for ions, respectively, T_s and m_s, the temperature and ion mass, T_n and u_n are the neutral temperature and velocity, k is the Boltzmann constant, ν_{st} is the collision frequency between species s and t and S_{p_e} accounts for the contribution of the electron source terms. A complete derivation of these equations can be found in Chapter 2.

We use a reasonably comprehensive chemical scheme; the associated reactions and rates are presented in Table 4.1. In order to evaluate some of the reaction rates that are temperature dependent, the individual ion temperatures are obtained from the individual pressures, while the electron temperature is assumed to be equal to the average ion temperature.

We choose to include the energy exchange due to ion-ion collisions since they are not negligible in the lower ionosphere, where they contribute to the pressure source term. We neglected the friction term resulting from ion-ion collisions since in this region of interest, the ion velocities are small. For ion-neutral collisions, unlike the single fluid model that used an ion-neutral collision frequency calculated

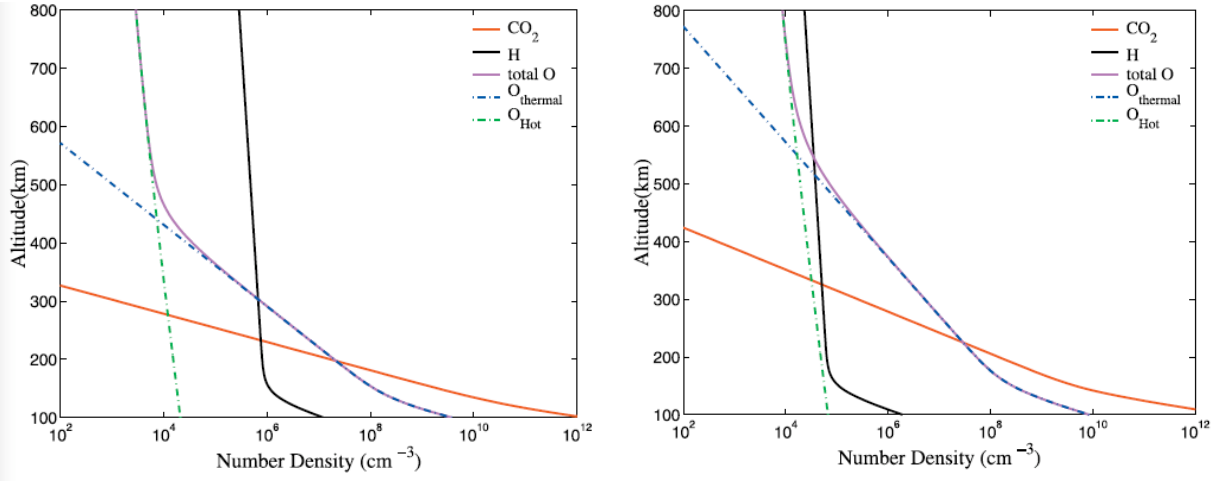

Figure 4.1: Density profiles of the neutral species adopted for solar cycle minimum (left) and maximum (right) conditions (*Ma et al.*, 2004)

by multiplying a constant number (4×10^{-10}) by the total neutral density, we calculate ion neutral collision frequencies separately for each combination of ion and neutral (*Schunk and Nagy*, 2009).

We approximate the optical depth effect by including a cosine factor for the different solar zenith angles and by assuming average absorption coefficients of 2.6×10^{-17} and 1.5×10^{-17} for CO_2 and O, respectively (*Schunk and Nagy*, 2009). On the nightside, we set the solar flux to be 10^{-15} times the unattenuated solar radiation, so as to avoid zeros. In order to permit direct comparison with the multi-species model results, we select the neutral atmosphere to be the same as was used by *Ma et al.* (2004) as shown in Figure 4.1.

We run simulations with and without crustal fields and also for the solar minimum and maximum conditions. We use the 60 degree harmonic expansion for the crustal magnetic field, developed by *Arkani-Hamed* (2001) to describe the observed fields at Mars (*Acuna et al.*, 1998). We can see clearly in Figure 4.2 the presence of significant and localized fields in the southern hemisphere of Mars.

The X axis of our coordinate system points from Mars toward the Sun, the Z

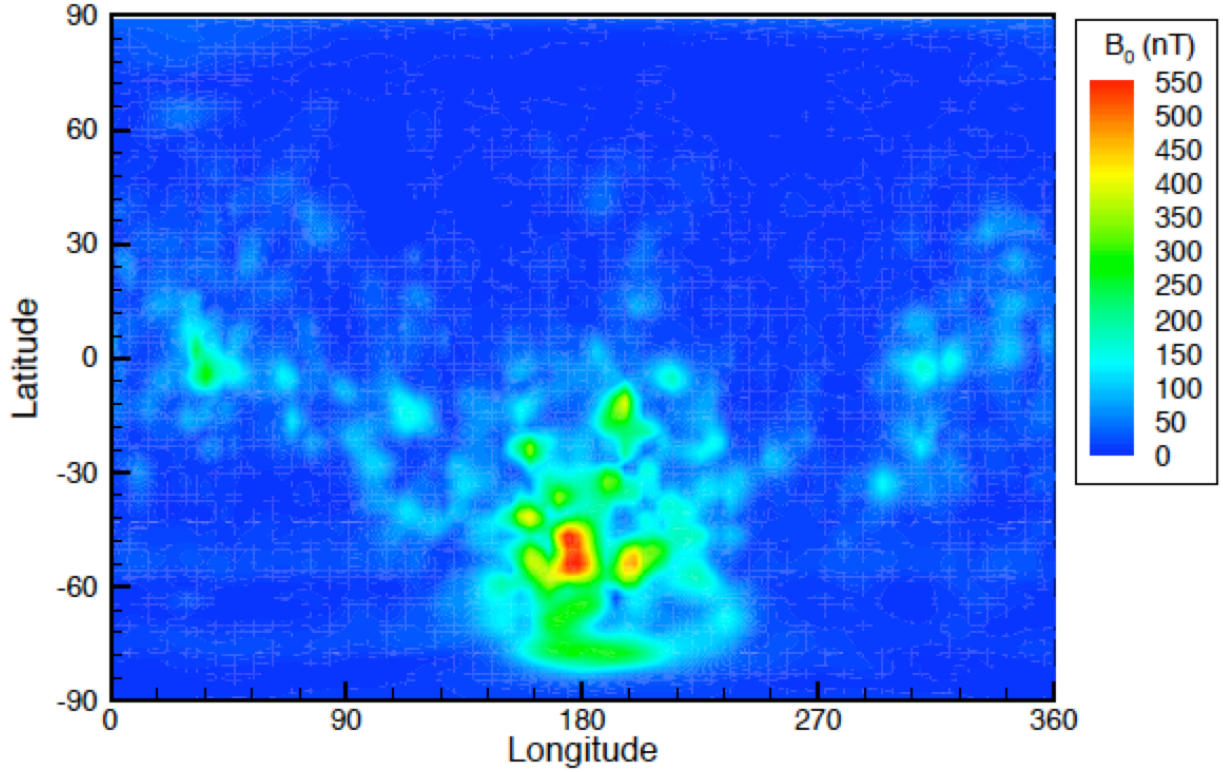

Figure 4.2: The remnant crustal magnetic field magnitude at an altitude of 200 km, calculated using the 60-order harmonic expansion of *Arkani-Hamed* (2001)

Table 4.1: List of chemical reactions and rates considered in the model

Reactions	Rate coefficient	References
$CO_2 + h\nu \rightarrow CO_2^+ + e$	$7.30 \times 10^{-7} s^{-1} (solarmax)$ $2.47 \times 10^{-7} s^{-1} (solarmin)$	*Schunk and Nagy* (2009)
$O + h\nu \rightarrow O^+ + e$	$2.73 \times 10^{-7} s^{-1} (solarmax)$ $8.89 \times 10^{-8} s^{-1} (solarmin)$	*Schunk and Nagy* (2009)
$H + h\nu \rightarrow H^+ + e$	$8.59 \times 10^{-8} s^{-1} (solarmax)$ $5.58 \times 10^{-8} s^{-1} (solarmin)$	*Ma et al.* (2004)
$CO_2^+ + O \rightarrow O_2^+ + CO$	$1.64 \times 10^{-10} cm^{-3} s^{-1}$	*Schunk and Nagy* (2009)
$CO_2^+ + O \rightarrow O^+ + CO_2$	$9.60 \times 10^{-11} cm^{-3} s^{-1}$	*Schunk and Nagy* (2009)
$O^+ + CO_2 \rightarrow O_2^+ + CO$	$1.1 \times 10^{-9} (\frac{800}{Ti})^{(0.39)} cm^{-3} s^{-1}$	*Fox and Sung* (2001)
$O^+ + H \rightarrow H^+ + O$	$6.4 \times 10^{-10} cm^{-3} s^{-1}$	*Schunk and Nagy* (2009)
$H^+ + O \rightarrow O^+ + H$	$5.08 \times 10^{-10} cm^{-3} s^{-1}$	*Fox and Sung* (2001)
$O_2^+ + e \rightarrow O + O$	$7.38 \times 10^{-8} (\frac{1200}{Te})^{(0.56)} cm^{-3} s^{-1}$	*Schunk and Nagy* (2009)
$CO_2^+ + e \rightarrow CO + O$	$3.10 \times 10^{-7} (\frac{300}{Te})^{(0.5)} cm^{-3} s^{-1}$	*Schunk and Nagy* (2009)

axis is normal to Mars' orbital plane and positive toward the north celestial pole, and Y axis completes the right-hand coordinate system. Our computational domain is defined by $-24R_M \leq X \leq 8R_M, 16R_M \leq Y, Z \leq 16R_M$, where R_M is the radius of Mars ($\sim$ 3396km). We use a non-uniform, spherical grid structure with a radial resolution varying from 10 km at the lower boundary to 630 km at the outer boundary.

We set our lower boundary to 100 km above the surface. The O_2^+, O^+ and CO_2^+ densities at the inner boundary are taken to be the photochemical equilibrium values. The electron and ion temperatures are assumed to be equal to the neutral temperature taken to be 300 K. A reflective boundary condition is used for $\mathbf{u}$, that results in near zero velocities at the inner boundary. We ran our model for the four different cases presented in Table 4.2. Cases 1, 2 and 3 are idealized simulations to better understand the model. Cases 4 and 5 correspond to realistic cases (solar minimum and maximum, respectively). The solar wind plasma temperature is set to 3.5×10^5 K. The IMF (Interplanetary Magnetic Field) is assumed to be a Parker spiral in the X-Y plane equal to (-1.677, 2.487, 0) - except for Case 1, where the IMF has only a By component. The solar wind velocity and density are selected to be 400 km/s and

Table 4.2: Simulation cases used in this study

Cases	Solar condition	Upstream B field	Position of crustal field	Hot O corona
Case 1	Solar minimum	(0, 3 nT, 0)	no crustal field	yes
Case 2	Solar minimum	(-1.677, 2.487, 0)	no crustal field	yes
Case 3	Solar minimum	(-1.677, 2.487, 0)	no crustal field	no
Case 4	Solar minimum	(-1.677, 2.487, 0)	$99.4°W$ $25.3°N$	yes
Case 5	Solar minimum	(-1.677, 2.487, 0)	$180°W$ $0°N$	yes
Case 6	Solar maximum	(-1.677, 2.487, 0)	$180°W$ $0°N$	yes

4 cm^{-3}, respectively for all the simulated cases.

4.2 Simulation results and discussion

4.2.1 Test case

We first look at the symmetric test case (Case 1) results for both single and multi-fluid cases. The O_2^+ ion densities in the X-Z plane are shown in Figure 4.3. These ions are generated by photoionization and chemical reactions (see Table 4.1). While in the single fluid case the O_2^+ ion distribution is symmetric, in the multi-fluid MHD case, O_2^+ ions can move upstream and across the dominant H^+ ions of the solar wind. The density distribution is asymmetric due to the effect of the convective electric field **E** (along the Z axis, pointing northward), accounted for in the multi-fluid momentum equation, unlike the single fluid case.

In fact, the main signature of multi-fluid effects are the asymmetries due to the Lorentz force on each ion. In the individual momentum equation, we include the gyration of the ion with respect to the charge averaged velocity $\mathbf{u}_+$. It can easily be proved that the $(\mathbf{u_s} - \mathbf{u}_+) \times \mathbf{B}$ term will lead to an asymmetry in the X-Z plane only, as long as the magnetic field is in the X-Y plane.

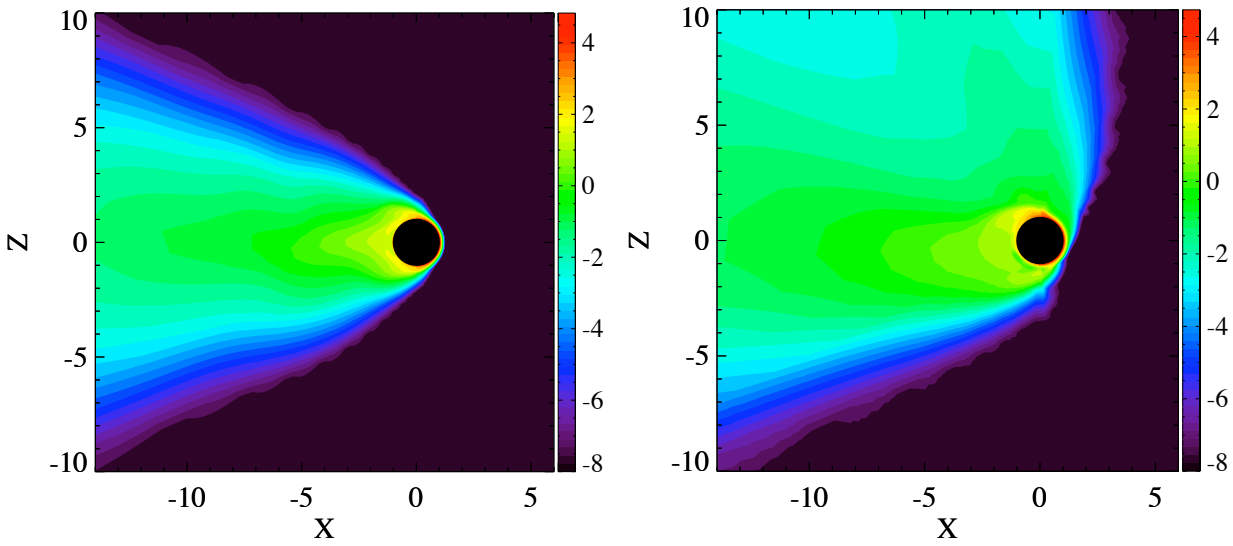

Figure 4.3: Calculated O_2^+ number densities: the single-fluid (left) and multi-fluid (right) models in a logarithmic scale from 10^{-8} to 10^4 cm^{-3} (Case 1).

4.2.2 Magnetic field and velocity

The asymmetries described in the previous section can be observed in solar minimum simulation results (Case 2). We purposely chose to consider a case without crustal field (Case 2) to highlight the multi-fluid effect on the magnetic field, without overlapping of the the crustal field effect.

The calculated magnetic field and velocity values are shown in Figures 4.4 and 4.6. In both figures, we plotted the magnetic field in the X-Y and X-Z planes, respectively. The magnetic field in the X-Z plane is clearly asymmetric (Figure 4.4). This is a very important signature that we could not observe with ideal single fluid MHD.

In the X-Y plane, the magnetic pile up is symmetric (Figure 4.6). If we include the crustal field (Case 4), we observe the presence of closed magnetic filed lines on the dayside resulting from the "merging" of the crustal and IMF fields (Figure 4.7). The presence of such minimagnetospheres has been inferred by the electron reflectometer carried aboard the Mars Global surveyor (MGS) spacecraft (*Mitchell et al.*, 2001).

Similarly, the velocity profiles in Figures 4.4 and 4.6 show a sharp asymmetry in

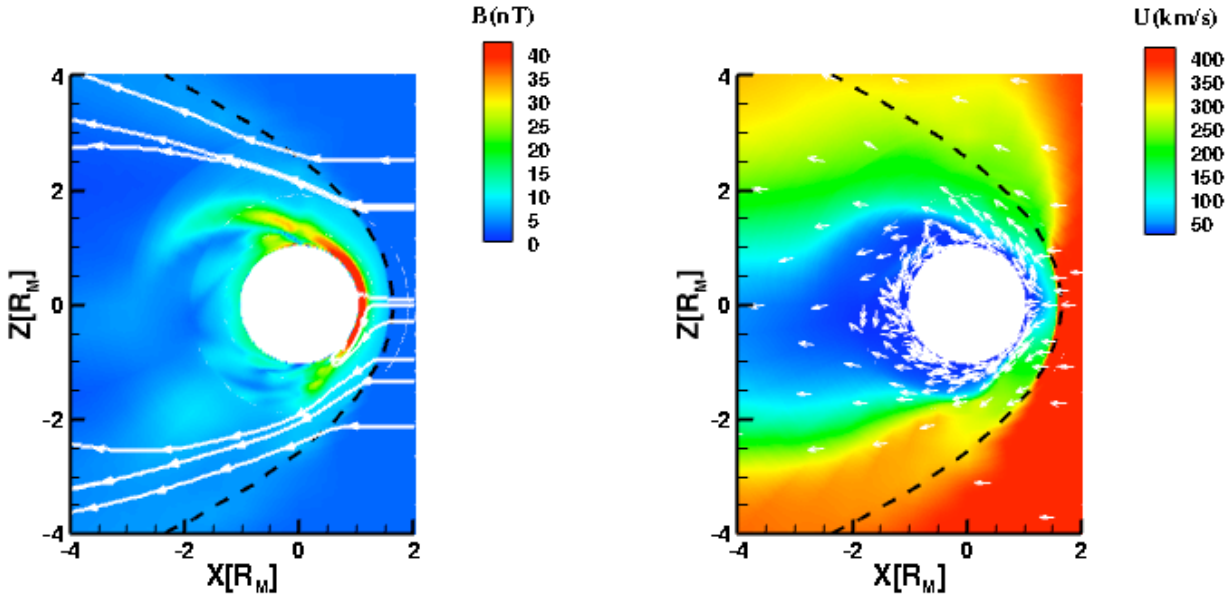

Figure 4.4: The calculated magnetic field and average ion velocity in the equatorial plane in the X-Z plane for solar minimum conditions. The color plots show the magnitudes; the white lines marked with arrows indicate the vector direction of the magnetic field and the white arrows show the direction (not the magnitude) of the velocity (Case 2). The dashed line represents the mean bow shock location from *Vignes et al.* (2000).

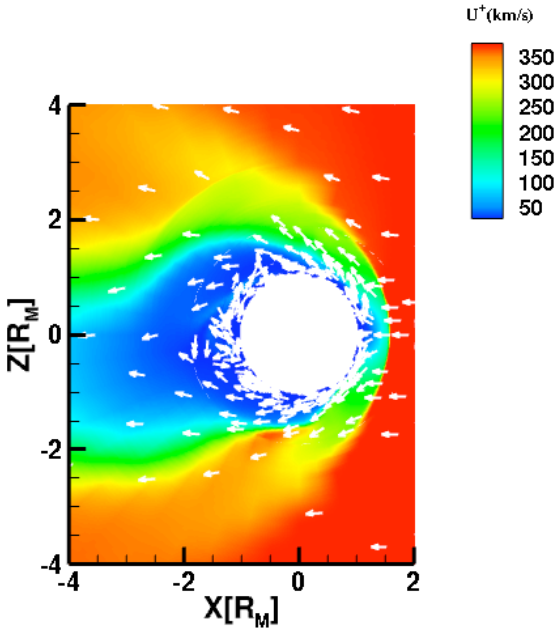

Figure 4.5: Calculated charge averaged velocity $\mathbf{u}_+$ in the X-Z plane (Case 2).

the X-Z plane and a symmetry in the X-Y plane. The newly observed asymmetry is again absent in the single fluid case (*Ma et al.*, 2004). The asymmetry of the total velocity in the X-Z plane is a result of the asymmetry of the individual velocities, since the total momentum is the sum of the individual momenta. The flow pattern is as expected, upward and toward the terminator on the dayside and partially downward on the nightside, to help maintain the nightside ionosphere, as well as outward through the tail, contributing to the escape flux. We also plotted the charge averaged velocity $\mathbf{u}_+$ in the X-Z plane: as we can see in Figure 4.5, the bow shock shape for $\mathbf{u}_+$ is closer to that of the magnetic field, which is a direct result of the induction equation.

Figure 4.8 shows the velocity of each species and we notice that the ionospheric heavy species are accelerated in the upper hemisphere. In fact, the newly born O^+, O_2^+, CO_2^+ are accelerated by the convective electric field. Given that the gyroradius is proportional to the mass of the species, we can see in Figure 4.8 that the lighter ion, O^+, is accelerated closer to the body, while the heavier CO_2^+ is accelerated further

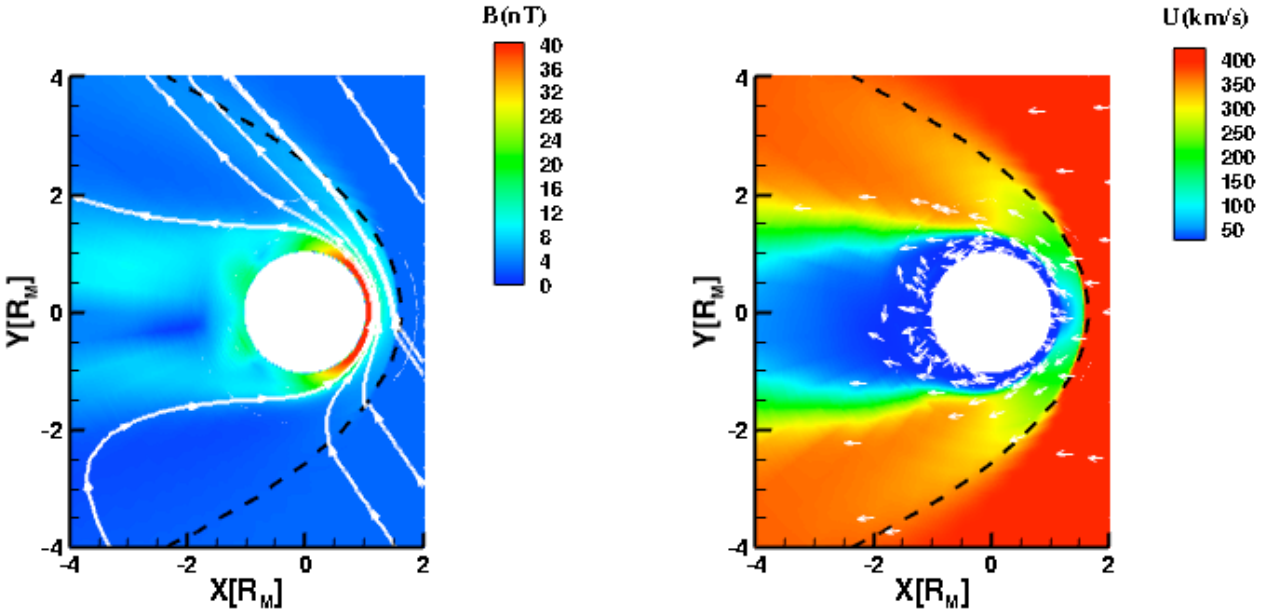

Figure 4.6: The calculated magnetic field and average ion velocity in the equatorial plane in the X-Y plane for solar minimum conditions. The color plots show the magnitudes; the white lines marked with arrows indicate the vector direction of the magnetic field and the white arrows show the direction (not the magnitude) of the velocity (Case 2). The dashed line represents the mean bow shock location from *Vignes et al.* (2000).

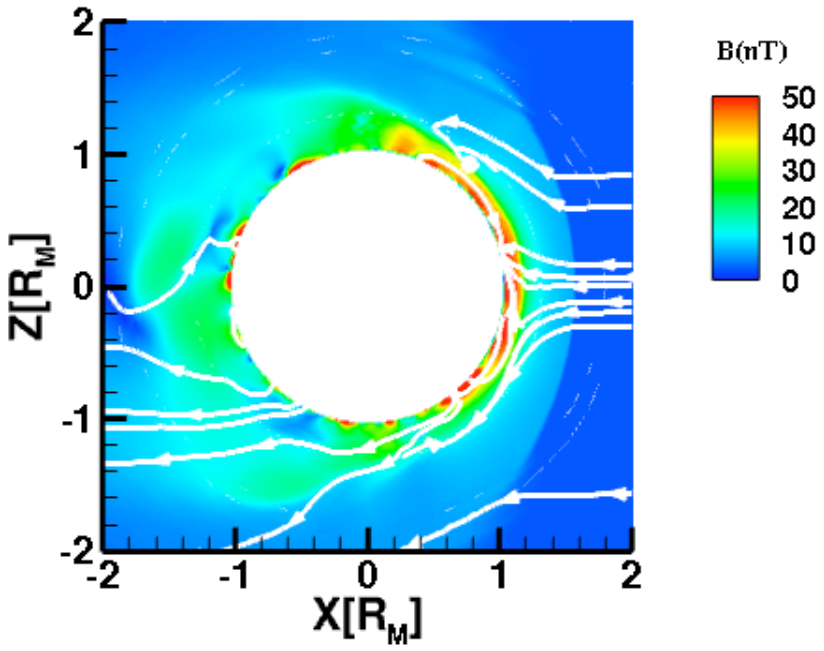

Figure 4.7: The calculated magnetic field the X-Z plane for Case 4 (including the crustal field).

out. In fact we can compute the gyroradius using the solar wind speed as the relative speed for each species obtaining $\sim 6.5\ R_M$ for O^+, $\sim 13\ R_M$ for O_2^+ and $\sim 18\ R_M$ for CO_2^+. We expect the acceleration to take place at a distance equal to twice the gyroradius which is confirmed by our calculations (Figure 4.8). Similar kinetic effects have been previously obtained by hybrid models in Mars (*Kallio et al.*, 2010) as we can see in Figures 4.9 (note the difference in scales) and they are now captured by our multi-fluid model (Figure 4.8).

4.2.3 Density

The multi-fluid effect can also be seen in the density results. Again, while in the single fluid case the densities are symmetric, the multi-fluid densities are strongly asymmetric in the X-Z plane, as we can see it in Figure 4.10. Hydrogen is not as asymmetric mainly because H^+ flows with the magnetic field $\mathbf{B}$. Also, it has a much smaller gyroradius than the other species. On the other hand, the densities in the X-Y plane are fairly symmetric since the convective electric field (and Lorentz force) are not contained in that plane and therefore do not affect the ion density distribution (Figure 4.11). Similarly to what we discussed previously for the velocities, the calculated ion distribution in the multi-fluid model is similar to the hybrid models' asymmetric density distributions (Figures 4.9). In Figure 4.12, we can see the results of different hybrid simulations of Mars; in all of them, we recognize an asymmetric density distribution similar our calculated densities. The"bite out" near 90° in the O^+ distribution in the X-Z plane (Figure 4.10) is caused by our simplified scheme to calculate the photoionization rate. The use of the more accurate Chapman function to calculate these rates would result in the photoionization of the atomic corona beyond the terminator.

The O_2^+ and CO_2^+ contour plots are quite similar whereas O^+ has a different shape mainly due to the ionization of the neutral oxygen corona, which pushes the density

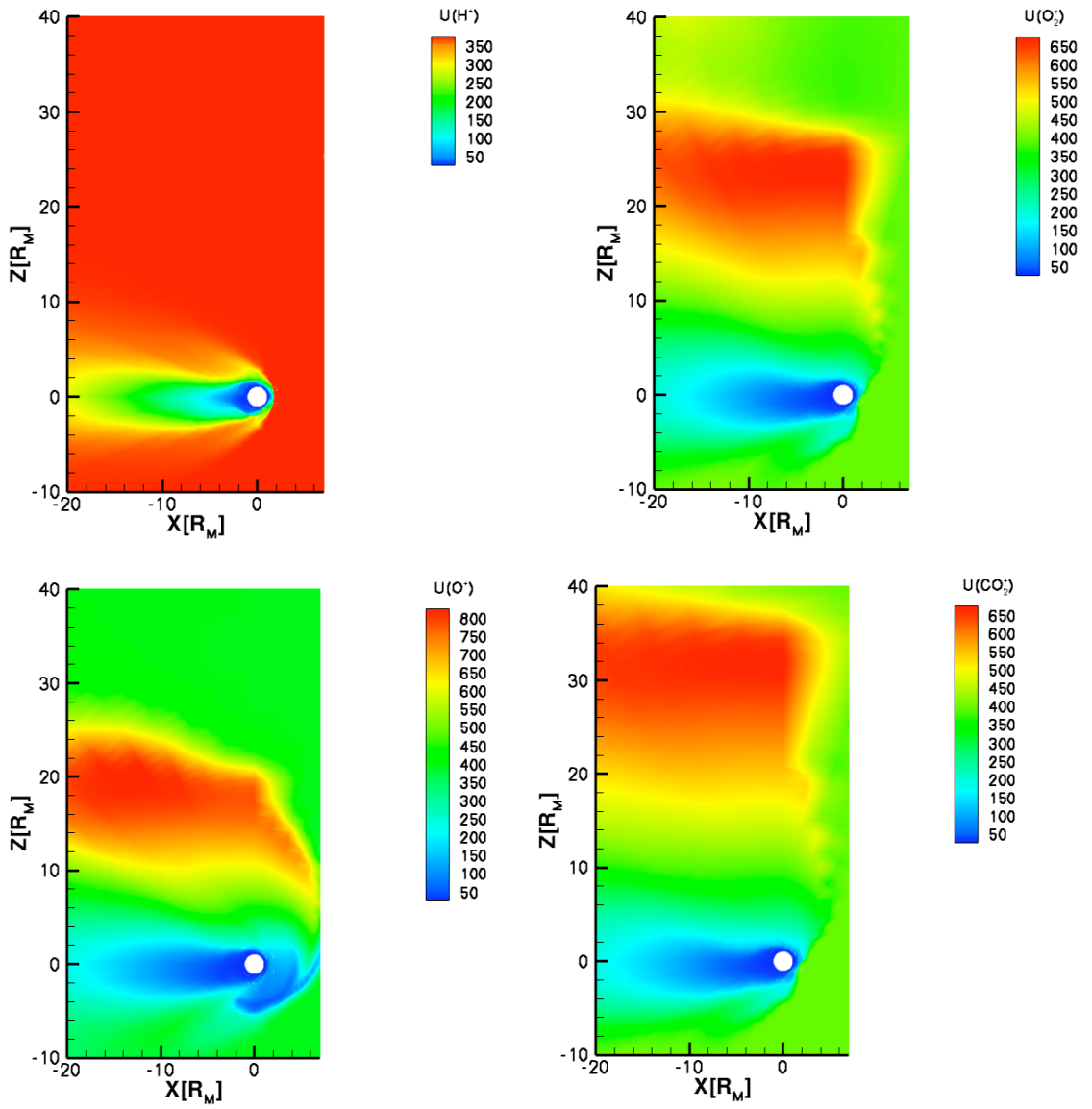

Figure 4.8: Calculated individual velocity for H^+, O_2^+, O^+, CO_2^+ (absolute value). We observe an acceleration of the flow around the body for the ionospheric species (Case 2)

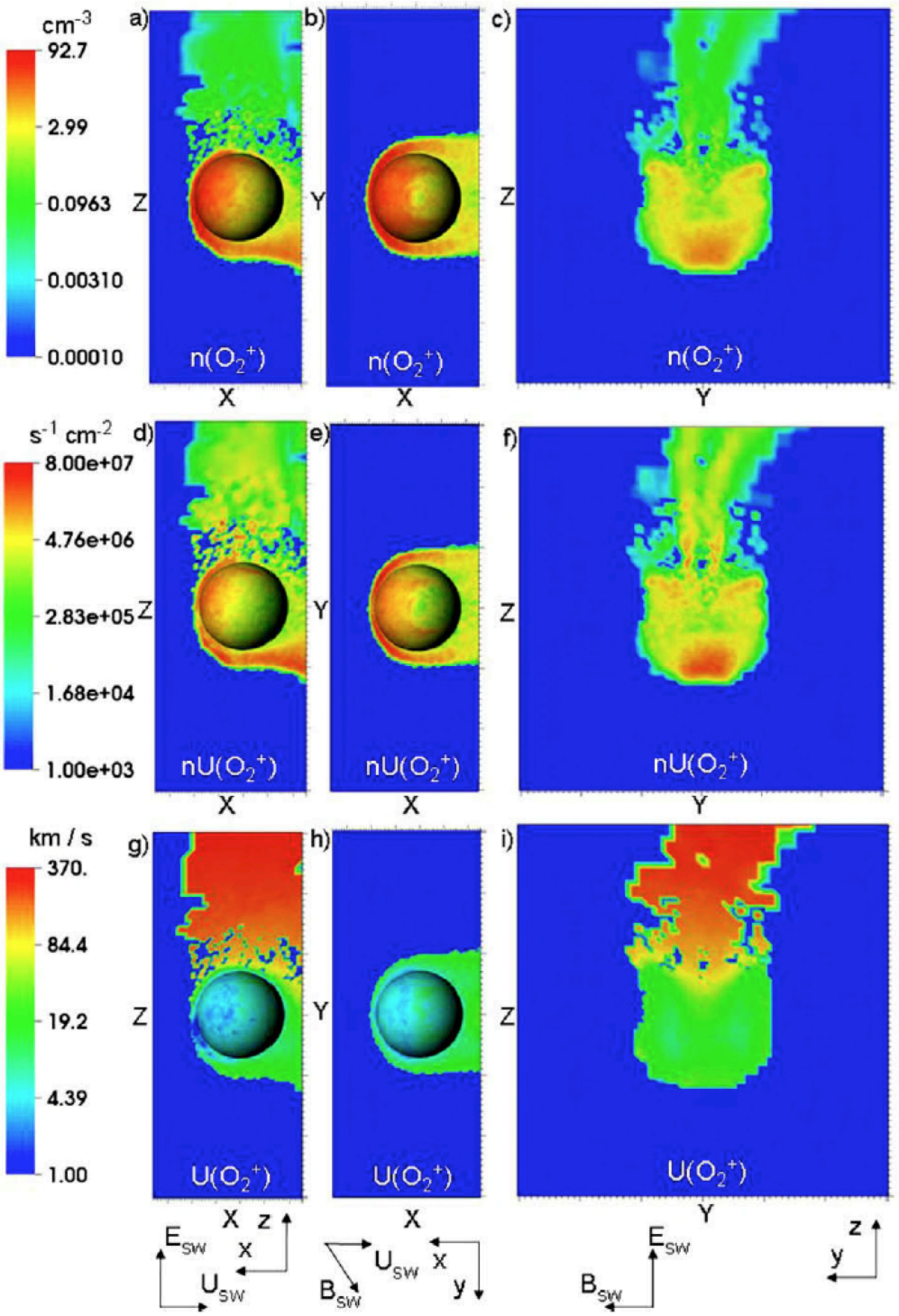

Figure 4.9: The O_2^+ ions near Mars results by *Kallio et al.* (2010). (a-c) the ion density, $n(O_2^+)$, in cm^{-3}; (d-f) the particle flux, $nU(O_2^+)$, in $cm^{-2}s^{-1}$; and (g-i) the bulk velocity, $U(O_2^+)$, in km. s^{-1} (*Kallio et al.*, 2010).

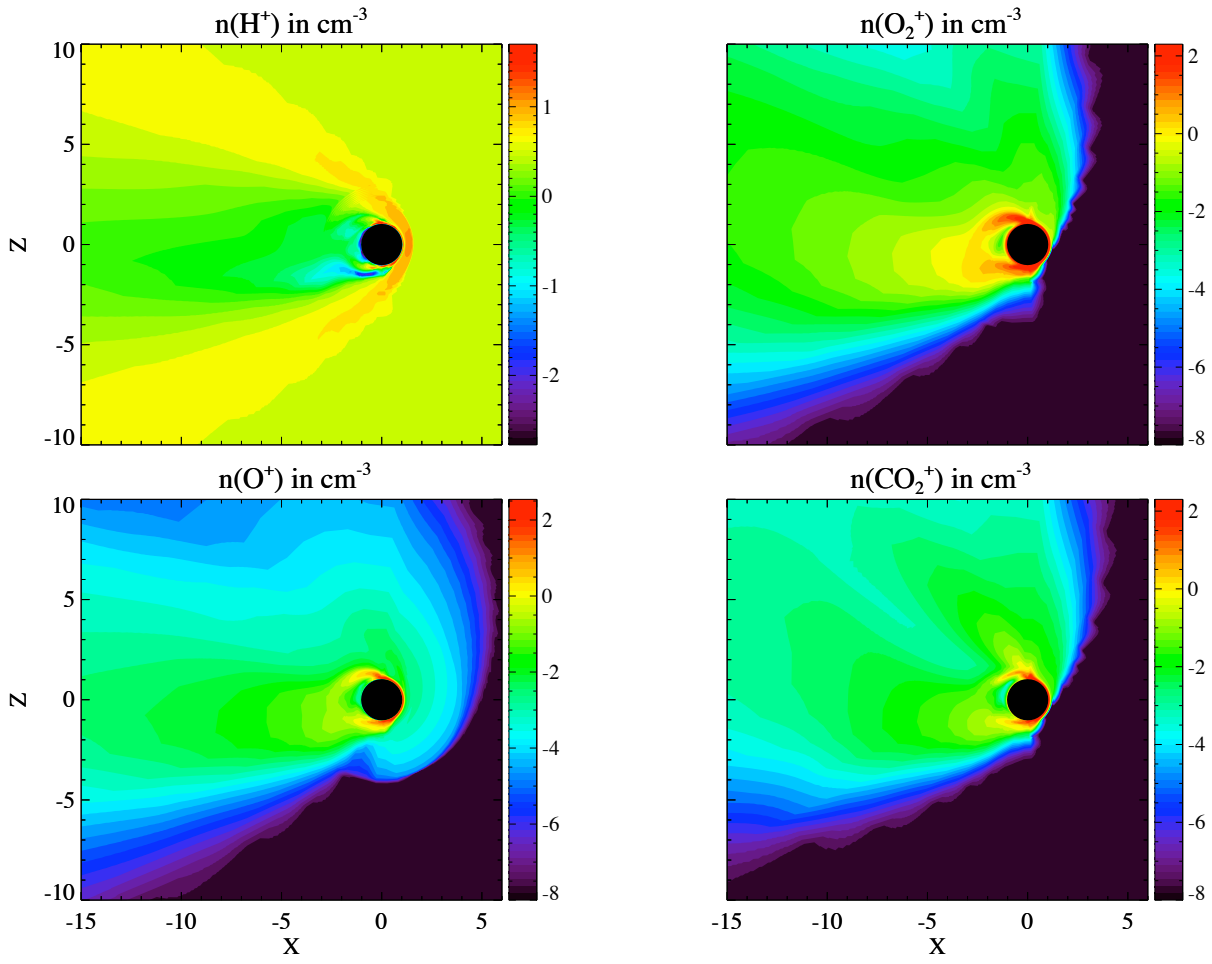

Figure 4.10: The calculated ion number densities in the X-Z plane for H^+, O_2^+, O^+, CO_2^+. Note the use of a logarithmic scale (Case 4).

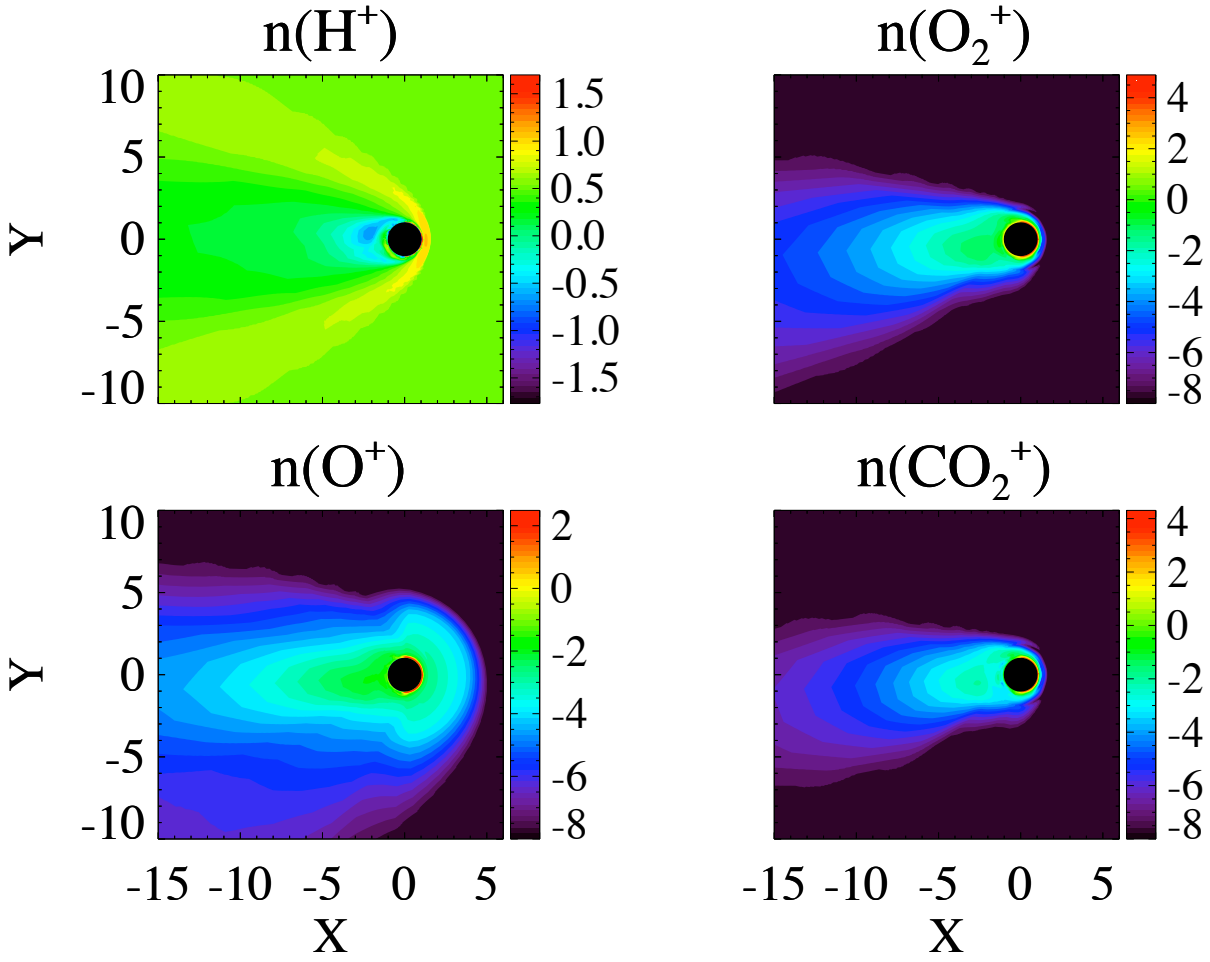

Figure 4.11: The calculated ion number densities in cm^{-3} in the X-Y plane for H^+, O_2^+, O^+, CO_2^+. Note the use of a logarithmic scale (Case 4).

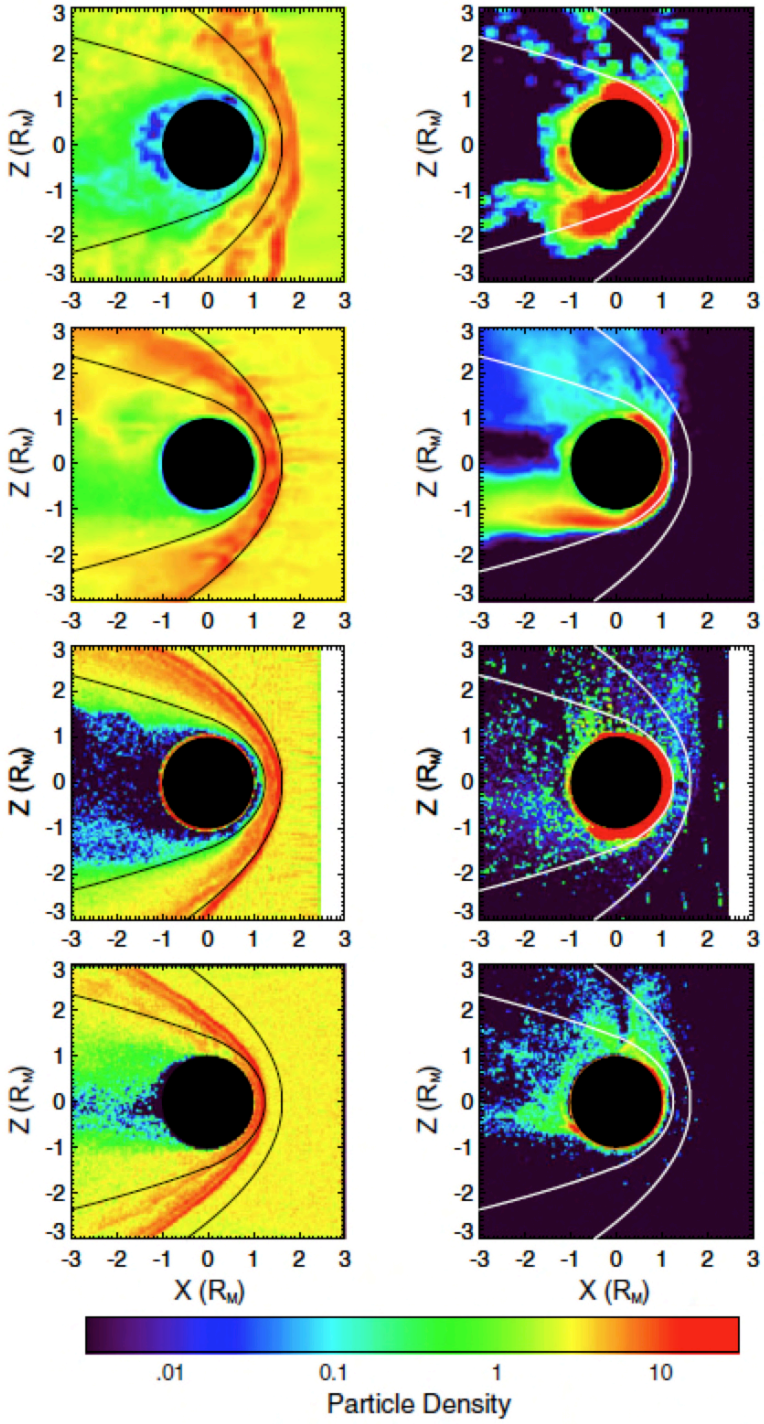

Figure 4.12: Model results for the Brecht, Kallio, Modolo, and Boesswetter hybrid models, from top to bottom: two-dimensional cuts of H^+ (left) and O^+ (right) in the X-Z plane (*Brain et al.*, 2010)

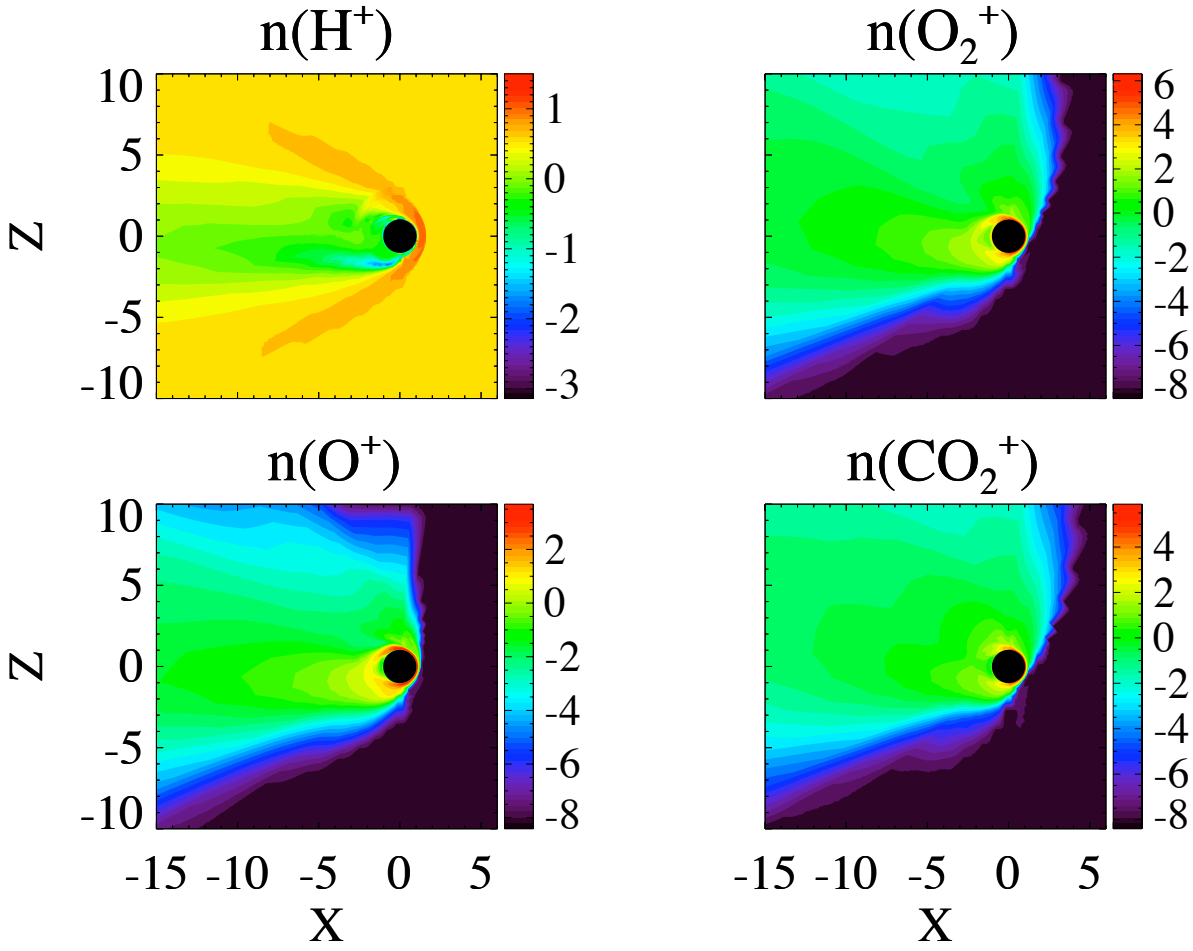

Figure 4.13: The calculated ion number densities in cm^{-3} in the X-Z plane for H^+, O_2^+, O^+, CO_2^+. Note the use of a logarithmic scale (Case 3: no hot O corona).

jump outward. To verify this hypothesis, we did a simulation equivalent to Case 2, but without the hot O corona this time (Case 3): as we can see in Figure 4.13, the density distribution for O^+ is now similar to O_2^+ and CO_2^+. This confirms the effect of the hot oxygen corona on the O^+ density distribution.

The hydrogen draping around Mars is barely visible since we do not distinguish between solar wind and ionospheric hydrogen. In order to observe the hydrogen properties more clearly, we introduced an additional hydrogen fluid and separated ionospheric and solar wind hydrogen. We observe, as expected, the formation of a

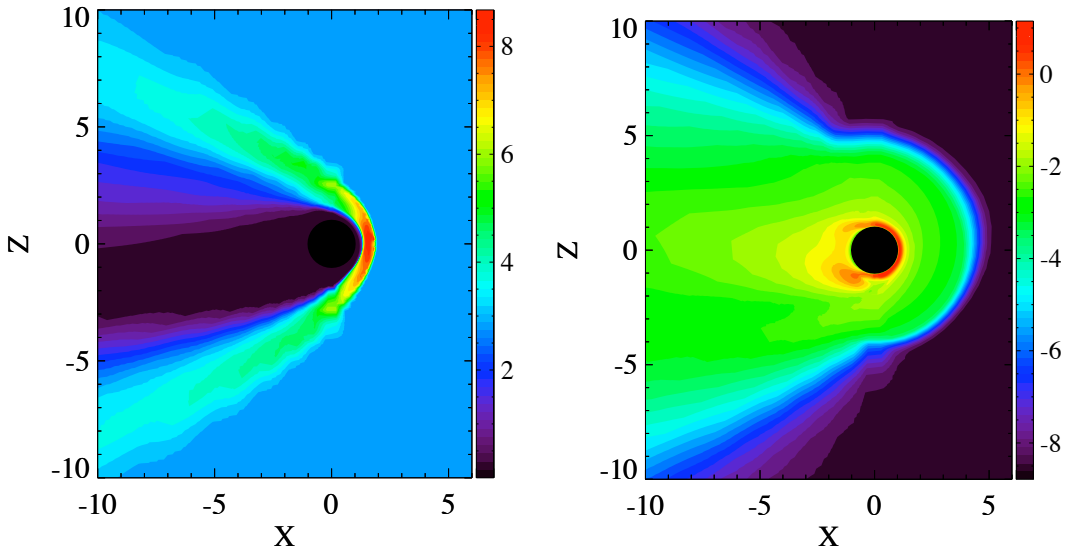

Figure 4.14: The calculated densities of the solar wind (left) and ionospheric hydrogen (right). Note that the ionospheric hydrogen density is in a logarithmic scale unlike the solar wind hydrogen density.

cavity in the solar wind H^+ flow close to the body as shown in Figure 4.14.

4.2.4 Temperature

Temperature plays an important role in the ionospheric region especially in determining the shape of the density distributions. However, thermal conduction, the main energy transport mechanism in the ionosphere, is not included in our MHD equations, although we hope to add it in the near future. Still, we were able to obtain a reasonable temperature profile from our results in Case 4, interpolated along the Viking trajectory (Figure 4.15). In fact, given the simplifying assumptions we made, our ion temperature profile is surprisingly close to observations by *Hanson et al.* (1977).

It is also important to mention the role ion-ion collisions play in the low ionospheric region. We noticed while running our simulations that the addition of ion-ion collisions coupled the temperatures of the individual fluids and brought them closer to one another. While this coupling is unecessary in the single fluid model, it is im-

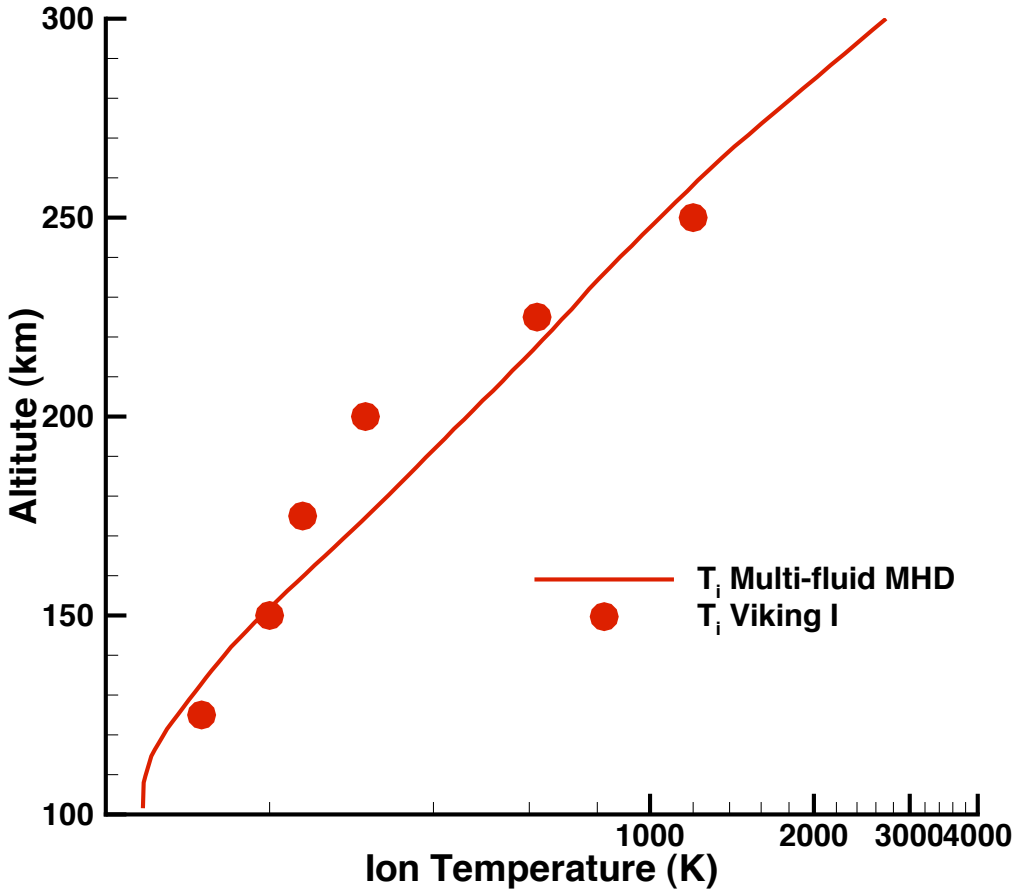

Figure 4.15: The calculated total ion temperature in K , along the Viking trajectory - Case 4- from our multi-fluid model and the observed temperature profile by Viking 1(*Hanson et al.*, 1977).

portant to add it the multi-fluid case. As a result, the fit of our calculated values to observations has considerably improved.

4.2.5 Pressure

Figure 4.16 shows the solar minimum subsolar pressure profile for Case 2. $P_{thermal}$ is the total thermal pressure, P_B is the magnetic pressure, $P_{dynamic}$ is the dynamic pressure and P_{total} is the total pressure. The bow shock separates the dynamic pressure and the thermal pressure dominated regions. In this case, without the remnant crustal field, the bow shock is located at 1.53 R_M. We can see the magnetic pile up boundary (MPB) as we move from a thermal pressure to a magnetic pressure dominated region at 1.14 R_M.

Figure 4.17 shows the solar minimum pressure profile for Case 4 (crustal field added). The bow shock is located at 1.56 R_M, which is close to the MGS observations (*Vignes et al.*, 2002) and slightly further out than the single fluid model results (*Ma et al.*, 2004). We can see the magnetic pile up boundary (MPB) is at 1.17 R_M. We notice by comparing figures 4.16 and 4.17 that the presence of the crustal field pushes the MPB outward and increases the magnetic pressure close to the body. The bow shock is also pushed outward as a result.

We also run simulations for the solar maximum condition (Case 6) so as to see whether the solar condition plays a role in the bow shock location as well in the shape of the pressure profiles. The main difference between solar minimum and solar maximum is different neutral profiles and ionization rates (not in the values of the solar wind conditions). This results in a more extended ion plume distribution around the body. Figure 4.18 shows the corresponding pressure profile. As observed in the single fluid case (*Ma et al.*, 2004), the solar maximum case has a bow shock and MPB further out from the body than in the solar minimum case. In Figure 4.18, we observe the bow shock at 1.67 R_M and the MPB at 1.26 R_M. This is consistent with

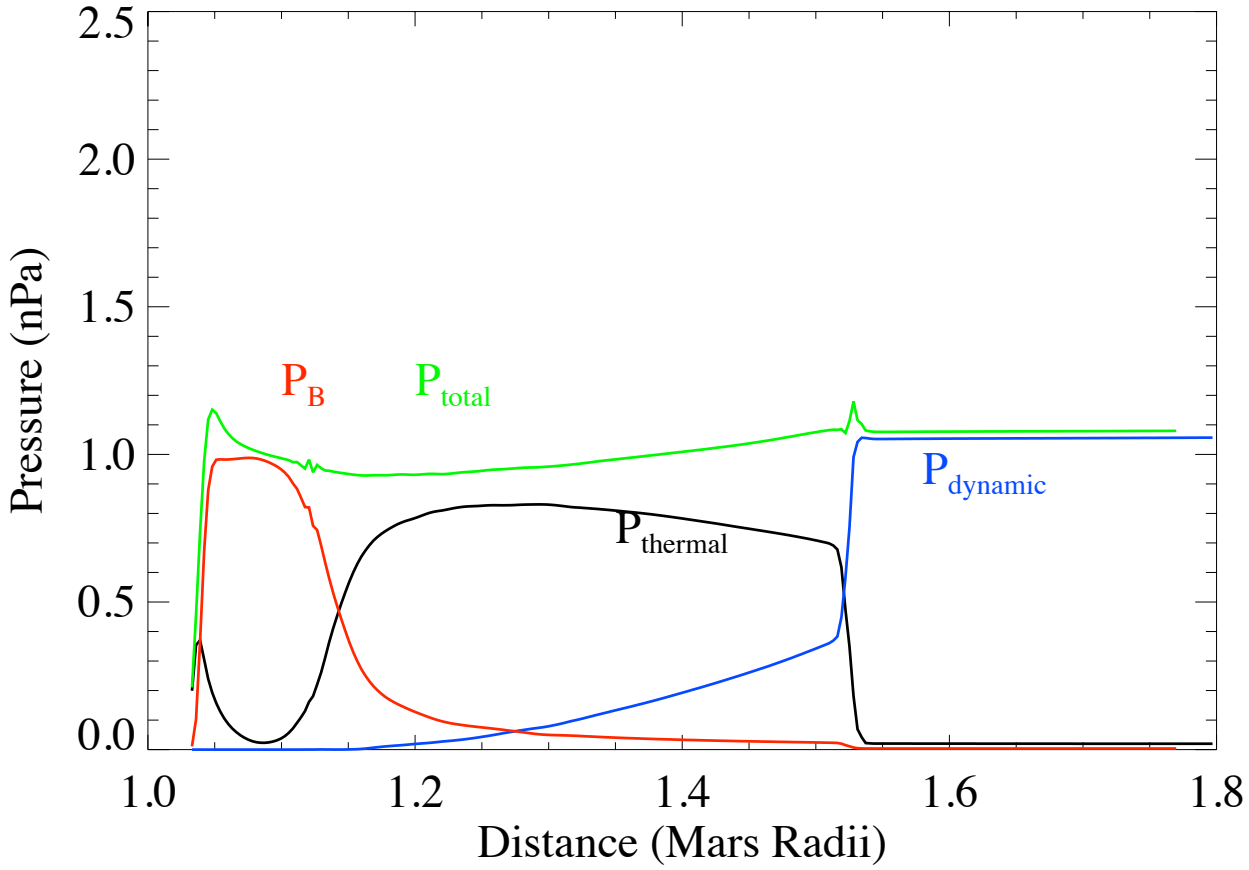

Figure 4.16: Pressure profiles along Sun-Mars line in the dayside for solar minimum without the crustal field (Case 2).

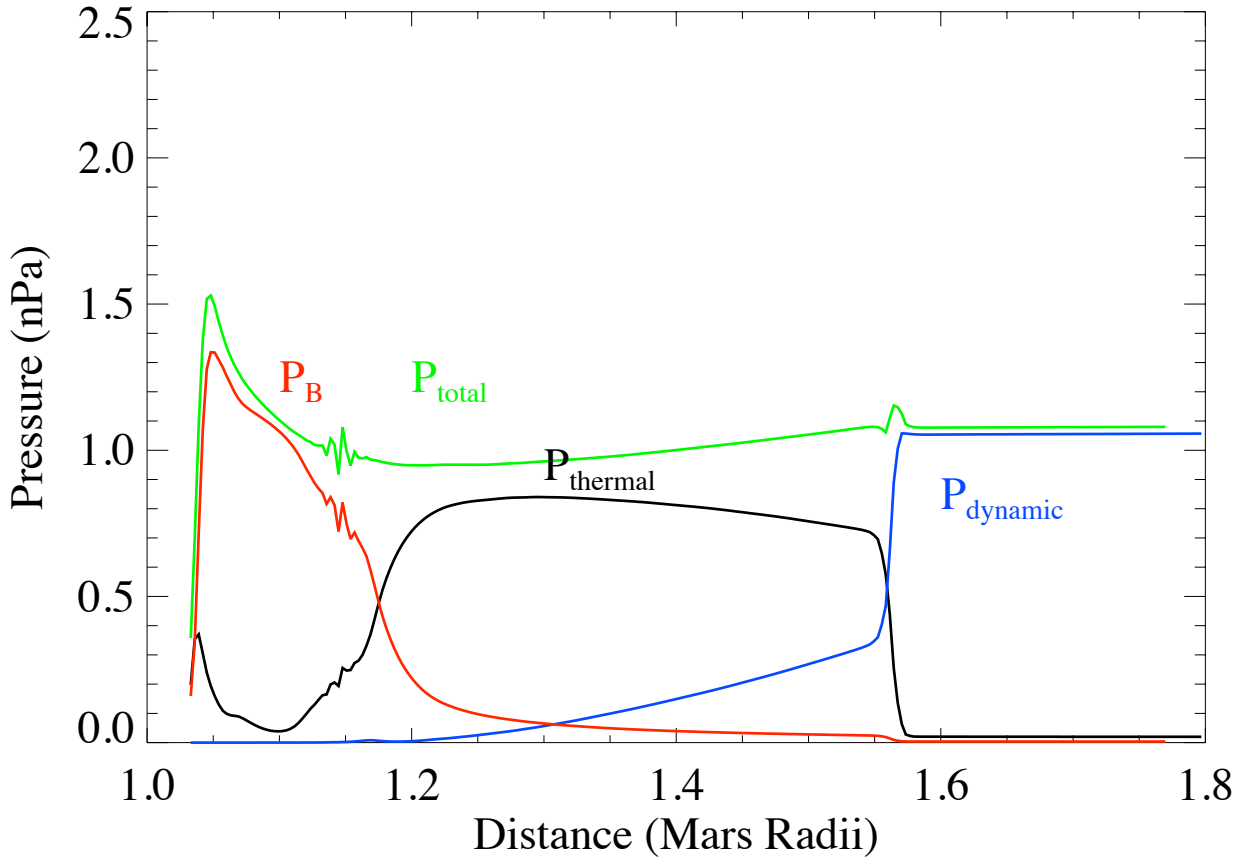

Figure 4.17: Pressure profiles along Sun-Mars line in the dayside for solar minimum (Case 4).

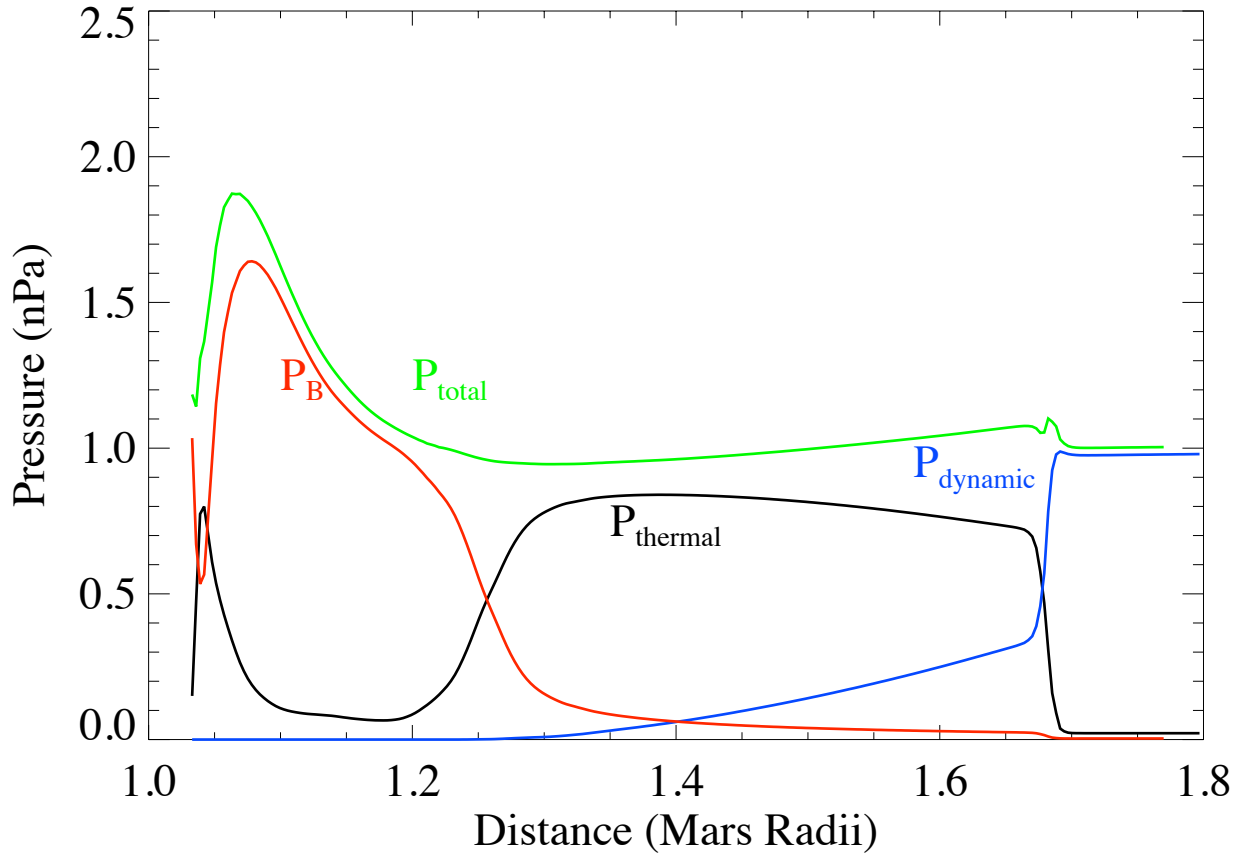

Figure 4.18: Pressure profiles along Sun-Mars line in the dayside for solar maximum (Case 6).

observations along the subsolar line (*Vignes et al.*, 2000).

4.2.6 Comparison to measured densities and role of the Hall effect

Our new model has been validated by comparing it to the single fluid model results and to observed values. In Figure 4.19, we compare our calculated electron density (Case 5) to the MGS radio occultation observation. Our results show a reasonable fit to the data.

We also compare our solar minimum results (Case 4) to the Viking observations by running a solar minimum simulation with the subsolar location taken to be at 99.4 west longitude and 25.3 north latitude in order to closely approximate the Viking

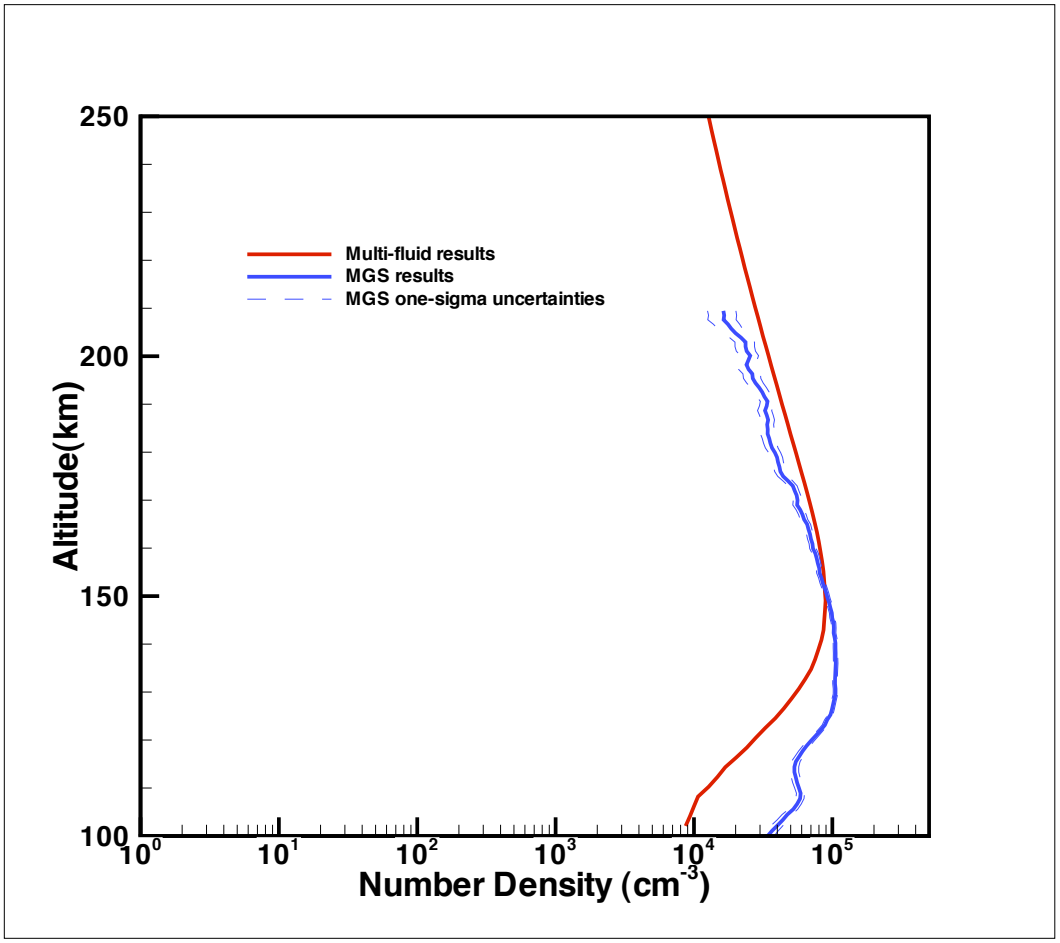

Figure 4.19: Comparison between MGS electron density measurements and Multi-fluid model results (Case 6)

conditions. The results are shown in Figure 4.20.

The agreement between the calculated and observed parameters in the region of the Viking measurements is similar to that obtained by the multispecies single-fluid model of *Ma et al.* (2004) (Figure 4.23), which is not surprising given the fact that the same chemistry scheme and neutral atmosphere parameters were used in both set of calculations and transport processes are not very strong in the region under consideration. The agreement between the calculated and observed molecular ion densities is quite good. The model results for O^+ are noticeably lower than the

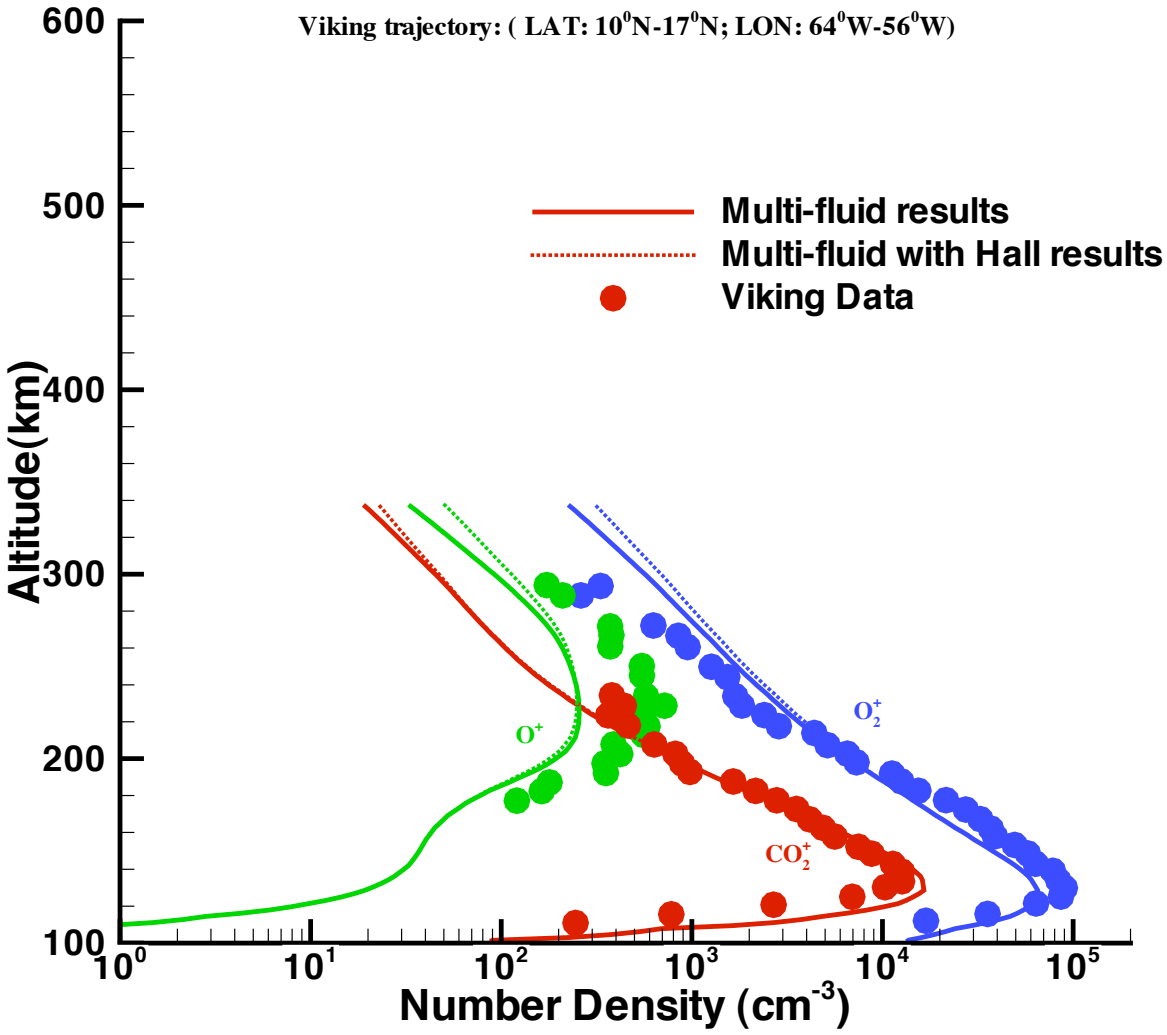

Figure 4.20: Comparison between Viking ion density measurements and the multi-fluid model results (with and without the Hall effect) along the Viking trajectory.

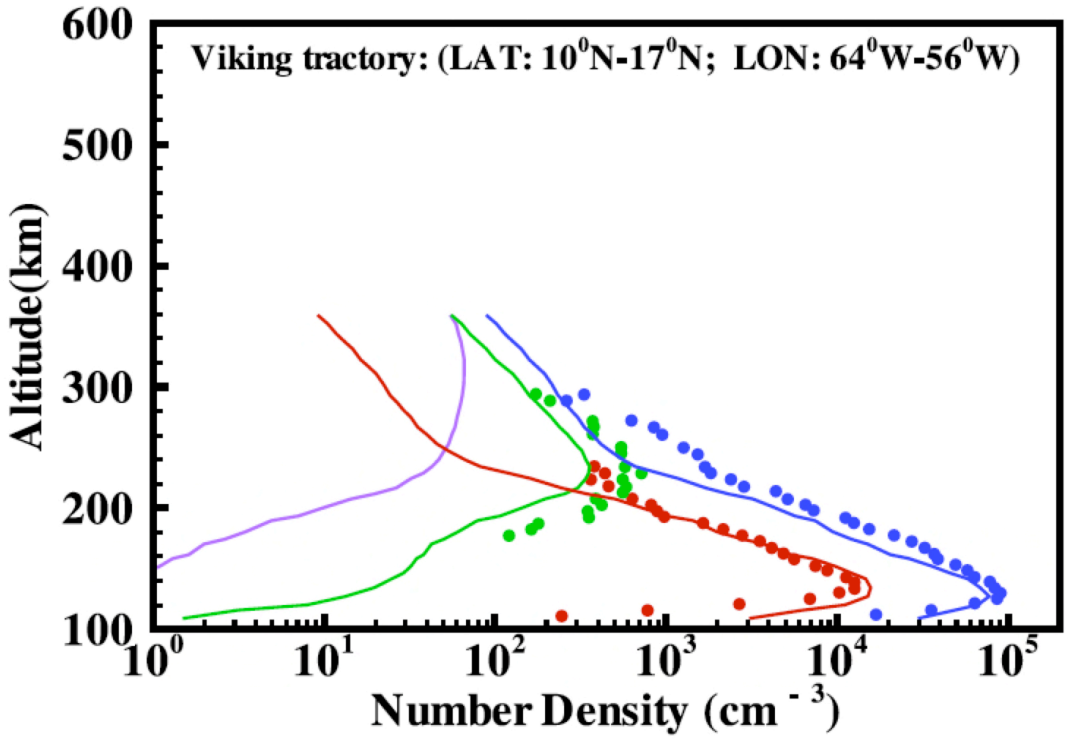

Figure 4.21: Comparison between Viking ion density measurements and the single-fluid model results along the Viking trajectory (*Ma et al.*, 2004)

measured values. However, we need to remember that the Viking mass spectrometer did not measure the atomic neutral density. Most of our current estimate of the O density came from fitting the measured O^+ density by adjusting the neutral O density in 1D ionospheric models until a good fit was obtained (e.g. *Hanson et al.*, 1977; *Chen et al.*, 1978). In order to compare our results with the single-fluid model results we used the same neutral density values selected by *Ma et al.* (2004) and we did not undertake a systematic study of adjusting the O density to get a best fit. However as a test, we did double our O densities in order to establish the kind of adjustments necessary and that gave us a very good fit to the observed O^+ densities (Figure 4.22), although the CO_2^+ density now does not fit as well as before.

It is known that the transition between chemical equilibrium conditions to trans-

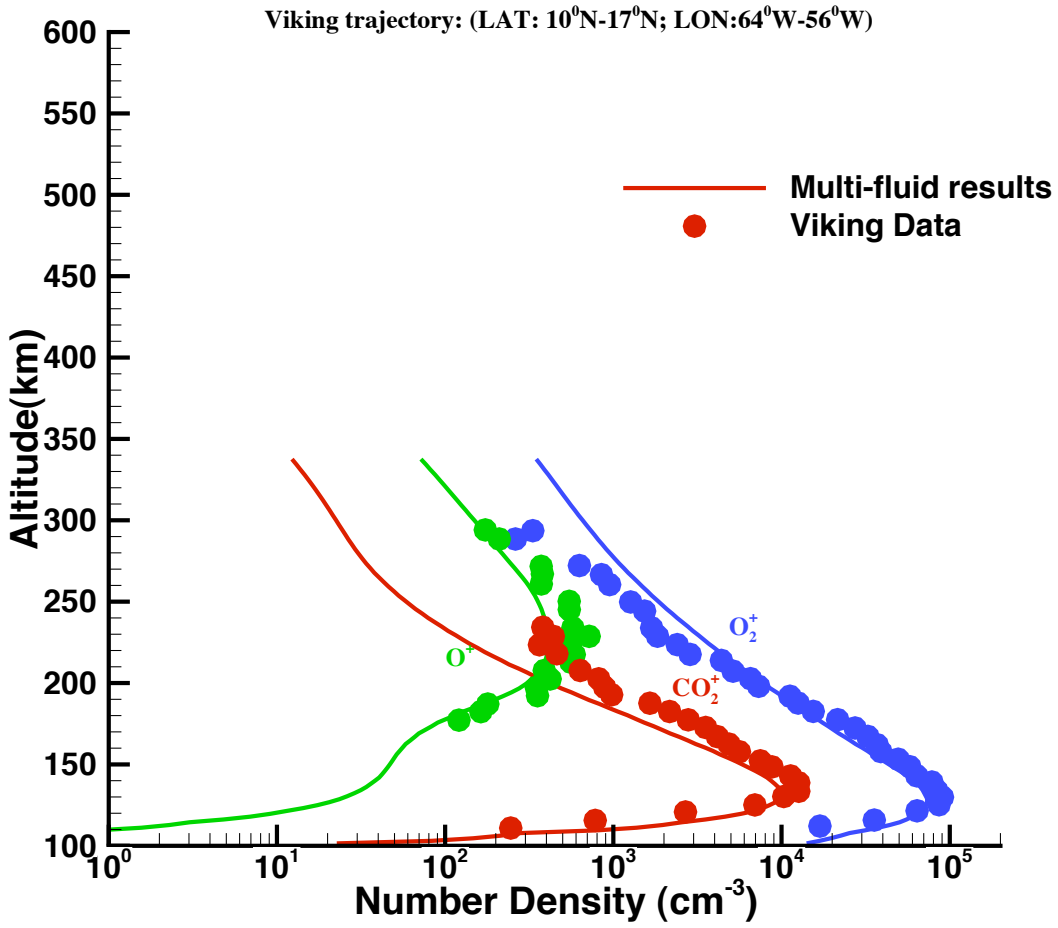

Figure 4.22: Comparison between Viking ion density measurements and the Multi-fluid model results along the Viking trajectory after doubling the oxygen neutral density

port takes place around 200 km. In fact, in the region above the peak and below the region where transport dominates, the plasma decreases with a scale height that is equal to approximately twice that of the major ionizable neutrals (cf. *Schunk and Nagy*, 2009). The measured Viking CO_2^+ and O_2^+ scale heights are about 23 and 29 km and it is also the case for our calculated values. On the other hand, the exospheric neutral gas temperature has been measured by Viking (*Nier and McElroy*, 1977) to be about 185 K, giving a neutral scale height of about of about 10.4 and 28.5 for CO_2 and O respectively, which is consistent with the observed (Viking) and calculated (multi-fluid) data.

We also ran a case for solar cycle minimum conditions with no crustal field (Case 2) and interpolated our results along the Viking trajectory. The major difference is that ion densities are lower in the absence of crustal field (Figure 4.23).

We also notice above 200 km, in the region where chemical control is no longer dominant, an increase in the slope which suggests larger effective scale heights. There has been a discussion about the role of horizontal magnetic fields and how they may affect vertical transport in the region (*Krymskii et al.*, 2002), but Pioneer Venus observations at Venus suggested the horizontal magnetic field explanation is improbable (*Dwivedi and Mahajan*, 2003).

The issue is that previous discussions have assumed that the temperature is constant with altitude, which is not the case in the ionospheric region where we have significant temperature gradients that can reduce the effective scale height (*Schunk and Nagy*, 2009).

Let us write the one-dimensional, steady state, vertical momentum equation:

$$\frac{\partial p}{\partial r} = -\rho g \tag{4.10}$$

In equation 4.10, we can replace p by nkT to obtain (friction terms are neglected):

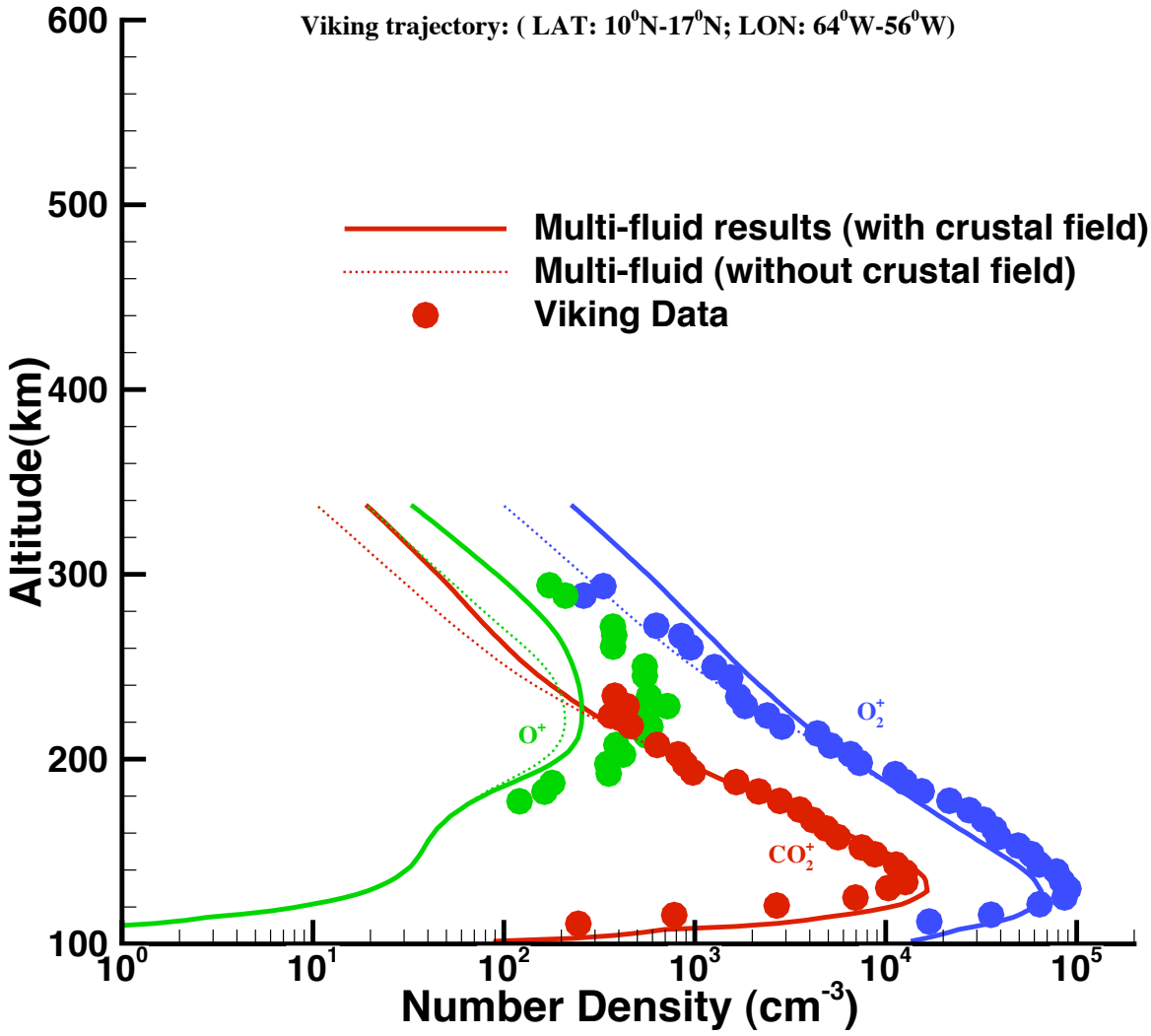

Figure 4.23: Comparison between Viking ion density measurements and the multi-fluid model results with and without crustal field along the Viking trajectory

$$kT\frac{\partial n}{\partial r} + nk\frac{\partial T}{\partial r} = -nmg \tag{4.11}$$

which gives, if we do not neglect the temperature gradient term:

$$\frac{1}{n}\frac{\partial n}{\partial r} = -\frac{mg}{kT} - \frac{1}{T}\frac{\partial T}{\partial r} \tag{4.12}$$

It is clear in equation 4.12 that the term $-\frac{1}{T}\frac{\partial T}{\partial r}$, which corresponds to the temperature gradient, contributes to reducing the effective scale height, if it is not negligible. Our results in that region show that in fact, that term is not negligible. Still, other studies showed that there might be other factors in addition to significant temperature gradients that could explain the change in the effective scale height. One of the other possible factors is plasma loss due to vertical transport as assumed by *Chen et al.* (1978) and *Fox* (1993). On the other hand, *Shinagawa and Cravens* (1989) constructed an MHD model and obtained the best agreement with the observed densities when they included an induced magnetic field and horizontal removal of plasma. Our results and past studies results seems to indicate that the observed change in the density slope is due to several factors such as temperature gradient, magnetic fields an plasma loss due to convective transport.

4.2.7 Hall Effect

The results presented so far were obtained neglecting the Hall effect in the magnetic field equation to highlight the asymmetries caused by the multi-fluid effect rather than the ones due to the decoupling of ions and electrons via the Hall effect. However, the Hall effect is available as an option in our code (*Ma et al.*, 2007; *Tóth et al.*, 2008) and has been included in some of our runs. As we can see in Figure 4.20, the addition of the Hall term does not modify our results significantly. The pressure profile shown in Figure 4.24 corresponds to the solar maximum case with the Hall

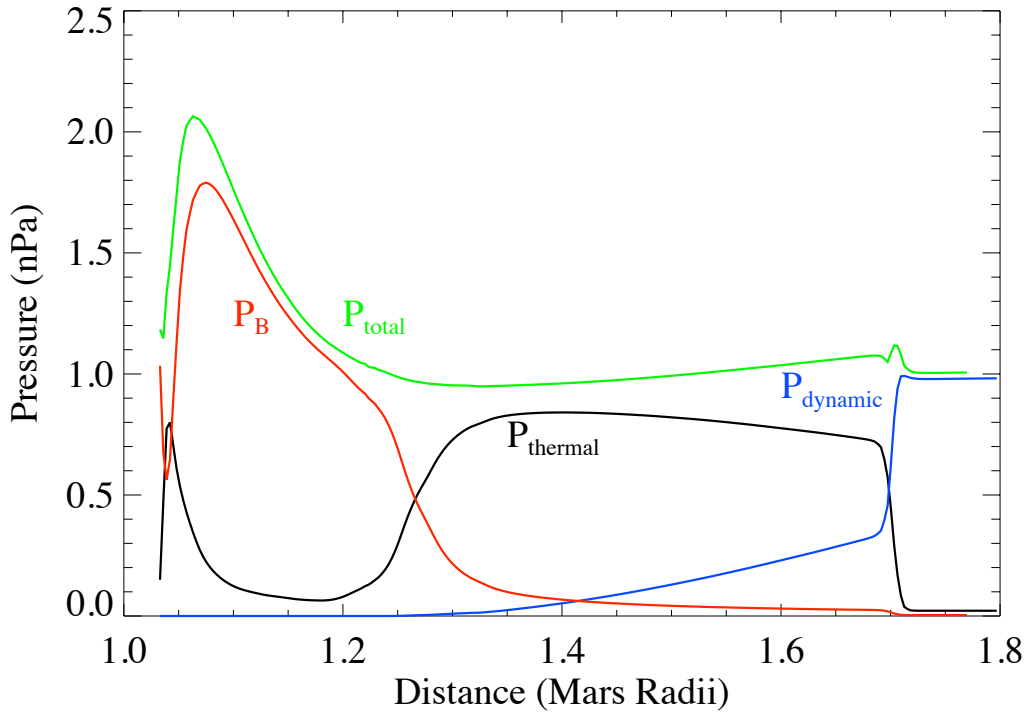

Figure 4.24: Pressure profiles along Sun-Mars line in the dayside for solar maximum with the Hall effect.

effect included; we can only see a slight outward movement of the shock. A summary of the MPB and bow shock positions for the different cases used in our study is shown in Table 4.3.

4.2.8 Escape fluxes

We also used our model to estimate the total escape fluxes at 6 Mars radii. Our results, given in Table 4.4, are somewhat different from the single fluid model (*Ma et al.*, 2007). The main difference is the much higher O_2^+ escape flux compared to the escape rates of the other species. This might be due to the new dynamics present in our model, in particular the existence of asymmetric plumes. Finally, our calculated total flux values are comparable but somewhat lower than the most recent measurement $(3 \times 10^{24} s^{-1})$, from the ASPERA instrument carried by Mars Express

Solar condition	Crustal field	Hall	MPB location in R_M	Bow Shock location in R_M
Solar minimum	No	No	1.14	1.53
Solar minimum	Yes	No	1.17	1.56
Solar minimum	Yes	Yes	1.17	1.58
Solar maximum	Yes	No	1.26	1.67
Solar maximum	Yes	Yes	1.27	1.7

Table 4.3: The calculated subsolar MPB and bow shock positions for solar minimum and solar maximum with and without crustal field and Hall effect; the observed subsolar bow shock and MPB locations are 1.64 ± 0.08 R_M and 1.29 ± 0.04 R_M respectively (*Vignes et al.*, 2000)

Escape fluxes in s^{-1}	O^+	O_2^+	CO_2^+	Total
Case 2	2.2×10^{23}	1.4×10^{24}	2.9×10^{23}	1.91×10^{24}
Case 4	1.6×10^{23}	1.4×10^{24}	2.1×10^{23}	1.77×10^{24}
Case 5	2.0×10^{23}	2.9×10^{24}	4.1×10^{23}	3.51×10^{24}
Case 6	7.7×10^{23}	9.0×10^{23}	1.7×10^{23}	1.84×10^{24}

Table 4.4: Calculated escape fluxes for Mars using the multi-fluid model

(*Lundin et al.*, 2008).

4.3 Summary

Our new multi-fluid MHD model of Mars gives very promising results. It succeeds in describing new physical processes such as the density plumes and the asymmetries due to the decoupling of the ions, which could not previously be observed with the single fluid model. At the same time, it verifies the observed bow shock locations and shows a reasonable fit to the data.

We observe an asymmetric magnetic pile up and velocities in the X-Z plane resulting from the Lorentz force in the Z direction. We observe gyroradius effects in the individual velocities distributions proving that our model can indeed capture kinetic effects that were not previously captured by the multispecies model.The Lorentz force also affects the ion density distribution around the body in the same plane. The

asymmetric density plume is a distinguishing feature for the heavy species (O^+, O_2^+, CO_2^+) and is a direct result of the decoupling of the ions as separate fluids. Our results are similar to results previously obtained by hybrid models (e.g. *Brecht*, 1997; *Brecht and Ledvina*, 2006; *Kallio et al.*, 2010), in regions where the simulations overlap. This work demonstrates that multi-fluid MHD models provide a good and credible way to study the interaction of fast moving plasmas with non-magnetic solar wind bodies.

We ran our model for different configurations (Cases 1 to 5) and we observed that adding a hot oxygen corona, the observed crustal field and going from solar minimum to solar maximum conditions push the magnetic pile up boundary and the bow shock outward. This variability of both the bow shock and the MPB has been predicted by the multispecies single fluid model and is now confirmed by our multi-fluid model. The Hall effect did not affect our results significantly.

Our multi-fluid model gives reasonable escape fluxes and the density results compare reasonably well with the observations made by MGS and very well with Viking data, thus validating our model.

In summary, our new multi-fluid MHD model enables us to describe accurately the interaction of Mars' ionosphere with the solar wind and observe physical processes that we could not describe with the single fluid model, while efficiently using our computational resources. This is an important contribution to the current studies on the topic as the main challenge has been to find a compromise between accuracy and efficiency.

Our future plans are to solve for the separate electron pressure equation and include thermal conduction in our equations. We also want to use a more realistic three dimensional atmosphere (as opposed to the spherically symmetric neutral profile we are currently using). For this purpose, we plan to use the three dimensional Mars thermospheric general circulation model (Mars TGCM), which incorporates a photochemical dayside ionosphere and includes seasonal, SZA and longitude variations in

its global structure (*Bougher et al.*, 2004).

CHAPTER V

Multi-fluid model of Venus' interaction with the solar wind

5.1 Introduction

In Chapter 4, we presented the results of our new Mars multi-fluid model and compared our results to observed values. The next step is to validate our multi-fluid model by applying it to another solar system body; Venus comes as a natural choice since its atmospheric composition is very similar to Mars'. We describe our Venus physical model and present our preliminary results for Venus' interaction with the solar wind. We obtain asymmetric densities, magnetic pile up and velocity distributions in the X-Z plane as a result of the multi-fluid effect. We show results for both solar maximum to solar minimum conditions and compare them to Pioneer Venus Orbiter (PVO) and Venus Express (VEX) observations.

5.2 Physical model and simulation details

In Venus' case, similarly to Mars, we solve separate mass, momentum and energy equations for the four fluids H^+, O_2^+, O^+, CO_2^+. The equations are the same as in Mars' case. We use a reasonably comprehensive chemical scheme; the associated reactions and rates are presented in Table 5.1. As we can see, most of the rates are the

Table 5.1: List of chemical reactions and rates considered in the model

Reactions	Rate coefficient	References
$CO_2 + h\nu \rightarrow CO_2^+ + e$	$1.30 \times 10^{-6} s^{-1} (solarmax)$ $4.27 \times 10^{-7} s^{-1} (solarmin)$	*Schunk and Nagy* (2009)
$O + h\nu \rightarrow O^+ + e$	$1.21 \times 10^{-6} s^{-1} (solarmax)$ $4.67 \times 10^{-7} s^{-1} (solarmin)$	*Schunk and Nagy* (2009)
$CO_2^+ + O \rightarrow O_2^+ + CO$	$1.64 \times 10^{-10} cm^{-3} s^{-1}$	*Schunk and Nagy* (2009)
$CO_2^+ + O \rightarrow O^+ + CO_2$	$9.60 \times 10^{-11} cm^{-3} s^{-1}$	*Schunk and Nagy* (2009)
$O^+ + CO_2 \rightarrow O_2^+ + CO$	$1.1 \times 10^{-9} (\frac{800}{Ti})^{(0.39)} cm^{-3} s^{-1}$	*Fox and Sung* (2001)
$H^+ + O \rightarrow O^+ + H$	$5.08 \times 10^{-10} cm^{-3} s^{-1}$	*Fox and Sung* (2001)
$O_2^+ + e \rightarrow O + O$	$7.38 \times 10^{-8} (\frac{1200}{Te})^{(0.56)} cm^{-3} s^{-1}$	*Schunk and Nagy* (2009)
$CO_2^+ + e \rightarrow CO + O$	$3.10 \times 10^{-7} (\frac{300}{Te})^{(0.5)} cm^{-3} s^{-1}$	*Schunk and Nagy* (2009)

same as Mars besides the photoionization rates. Also, note that we are considering here fewer reactions than in Mars' case. In order to evaluate some of the reaction rates that are temperature dependent, the individual ion temperatures are obtained from the individual pressures, while the electron temperature is assumed to be equal to the average ion temperature.

We run simulations for the solar minimum and maximum condition. The X axis of our coordinate system points from Venus toward the Sun, the Z axis is normal to Venus' orbital plane and positive toward the north celestial pole, and Y axis completes the right-hand coordinate system. Our computational domain is defined by $-24R_V \leq X \leq 8R_V, 16R_V \leq Y, Z \leq 16R_V$, where R_V is the radius of Venus ($\sim$ 6052 km). We use a non-uniform, spherical grid structure with a radial resolution as low as 10 km in the ionospheric region. We set our lower boundary to 100 km above the surface. The O_2^+, O^+ and CO_2^+ densities at the inner boundary are taken to be the photochemical equilibrium values. The electron and ion temperatures are assumed to be equal to the neutral temperature. A reflective boundary condition is used for $\mathbf{u}$ and $\mathbf{B}$. We ran our model for solar minimum (Case 1) and maximum (Case 2), respectively. In the solar maximum case, the upstream solar wind plasma temperature is set to 2.5×10^5K.

Cases	Solar condition	n_{SW} (cm^{-3})	U_{SW} ($km.s^{-1}$)	Upstream B field (nT)
Case 1	Solar minimum	25	-450.0	(7.76, -5.65, 0.0)
Case 2	Solar maximum	17	-400.0	(12.1, -8.82, 0.0)
Case 3	Solar minimum	14	-430.0	(8.09, 0.0, -5.88)

Table 5.2: Simulation cases used in this study and corresponding parameters.

The IMF (Interplanetary Magnetic Field) is assumed to be a Parker spiral in the X-Y plane with an angle of 36 degrees and a magnitude of 15 nT. The solar wind velocity and density are selected to be 400 km/s and 17 cm^{-3} respectively. These parameters correspond to a dynamic pressure P_D equal to 4.5 nPa and a Mach number $M_f = 4.5$. We use different parameters for the solar minimum case as shown in Table 5.2. We also run an additional case to compare to Venus Express conditions (Case 3). The summary of the parameters used in these simulations are presented in Table 5.2. It is important to note that for the Parker spiral cases for Venus (Cases 1 and 2), the signs for the magnetic field **B** are inversed with comparison to Mars, so in Venus' case, for this particular configuration, the convective electric field **E** is pointing southward.

Figure 5.1 shows the adapted neutral atmosphere and the production rates from *Fox and Sung* (2001); they are the same as the ones used by *Ma et al.* (2009). Unlike in Mars' case where we have neutral hydrogen and hot oxygen, we only consider, as a first step in our preliminary study, neutral CO_2 and O in Venus' case.

5.3 Simulation results and discussion

5.3.1 Magnetic field and velocity

We consider our solar minimum results and examine the magnetic field and velocity distribution. The calculated magnetic field and velocity values are shown in Figures 5.2 and 5.3. In both figures, we plotted the magnetic field and velocity in the X-Y and X-Z planes, respectively. The magnetic field in the X-Z plane is clearly

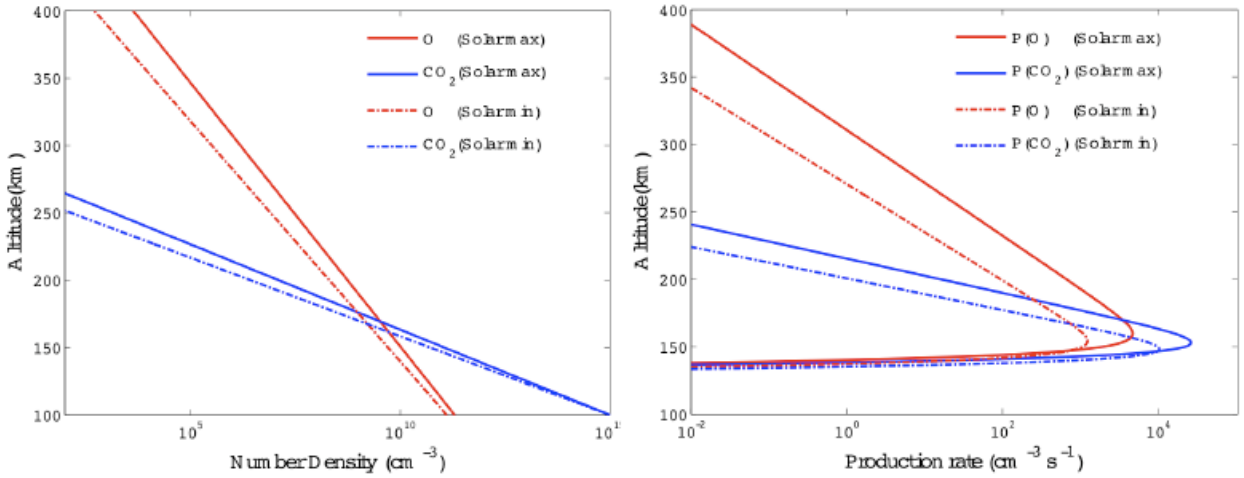

Figure 5.1: Density profiles of the neutral species adopted for solar cycle minimum and maximum conditions (left) and Ionization rates (right) (*Fox and Sung*, 2001)

asymmetric. This is a very important signature that we could not observe with ideal single fluid MHD and is due to the effect of the convective electric field **E** (along the Z axis, pointing southward). Please note that since the configuration of the magnetic is of opposite sign to that of Mars, the asymmetries in Venus and Mars are opposite to one another. In addition, since Venus radius ($R_V \sim 6052$ km) is about twice that of Mars ($R_M \sim 3396$ km), the kinetic effects are much less pronounced. In addition, the magnetic field in Venus' environment ($\sim$ 15 nT in solar maximum condition) is up to 5 times higher than the magnetic field in Mars ($\sim$ 3 nT). This results in a much smaller gyroradius in Venus' case and therefore even less pronounced kinetic effects.

In the X-Y plane, the magnetic pile up is symmetric (Figure 5.3). However, the shock position in the dawnside is closer than the shock position at the duskside. In fact, quasi-perpendicular shocks are dominating in the duskside, while quasi-parallel shocks dominate in the dawnside. This asymmetry of the bow shock in the X-Y plane

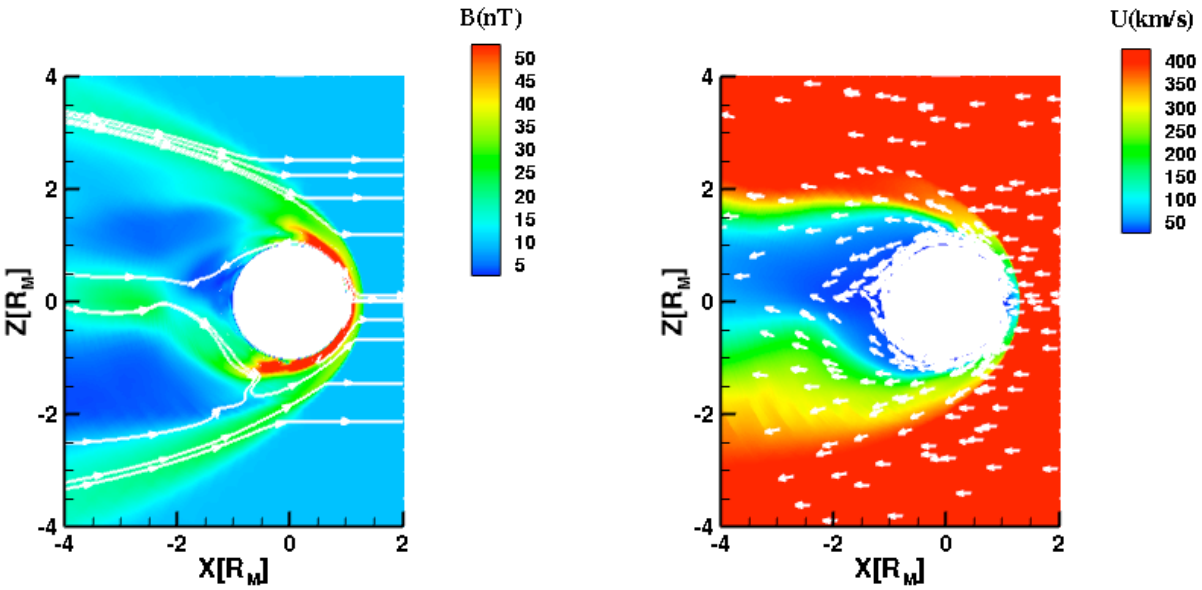

Figure 5.2: The calculated magnetic field and average ion velocity in the X-Z plane in Venus. The color show the magnitude of the vector field; the white lines correspond to the field lines and the white arrows show the direction (not the magnitude) of the velocity (Case 1).

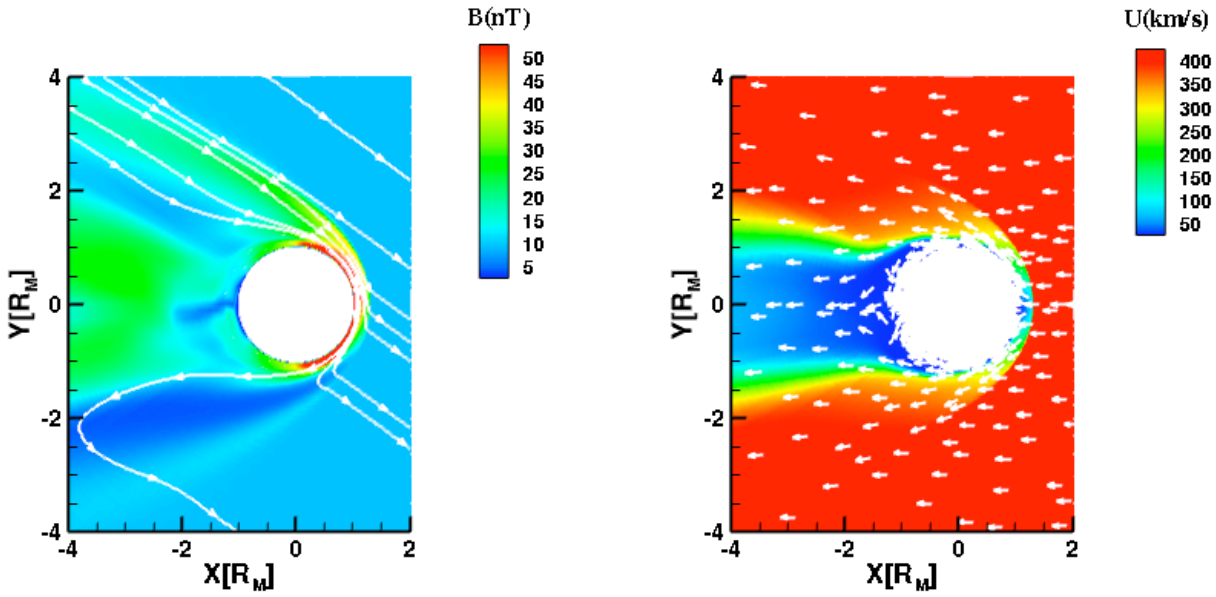

Figure 5.3: The calculated magnetic field and average ion velocity in the X-Y plane in Venus. The color show the magnitude of the vector field; the white lines correspond to the field lines and the white arrows show the direction (not the magnitude) of the velocity (Case 1).

is in agreement with observations (*Zhang et al.*, 1991).

Figure 5.4 shows the velocity of each species and we notice that the ionospheric heavy species are accelerated in the lower hemisphere by the convective electric field. Given that we expect the acceleration to take place at a distance equal to twice the gyroradius, and in the case of Venus, the gyroradius is much smaller than Mars', the acceleration takes place very close to the body. And the lighter the ion is, the smaller the gyroradius is, which explains why in Figure 5.4, we cannot see the acceleration of O^+ as it is too close to the body.

5.3.2 Densities

The density distribution is also asymmetric in the X-Z plane although much less pronounced than in Mars. Figures 5.5 shows the density distributions in the X-Z plane. The calculated ion distribution in the multi-fluid model is very similar to the hybrid models' asymmetric density distributions (*Kallio et al.*, 2006).

5.3.3 Pressure

Figure 5.6 shows the solar minimum subsolar pressure profile for Case 1. $P_{thermal}$ is the total thermal pressure, P_B is the magnetic pressure. $P_{dynamic}$ is the dynamic pressure and P_{total} is the total pressure. The bow shock separates the dynamic pressure and the thermal pressure dominated regions. The subsolar position of the bow shock is at 1.31 R_V. We can see the magnetic pile up boundary as we move from a thermal pressure to a magnetic pressure dominated region at 1.10 R_V. Note that unlike in Mars case, we do not have a sharp increase in the magnetic and total pressures close to the body. This is a result of the absence of magnetic crustal field at Venus.

We also ran simulations for solar maximum (Figure 5.7) and obtain a bow shock position at 1.33 R_V and a magnetic pile-up boundary at 1.15 R_V. This is consistent with Mars' results where solar maximum's condition pushed the bow shock outward.

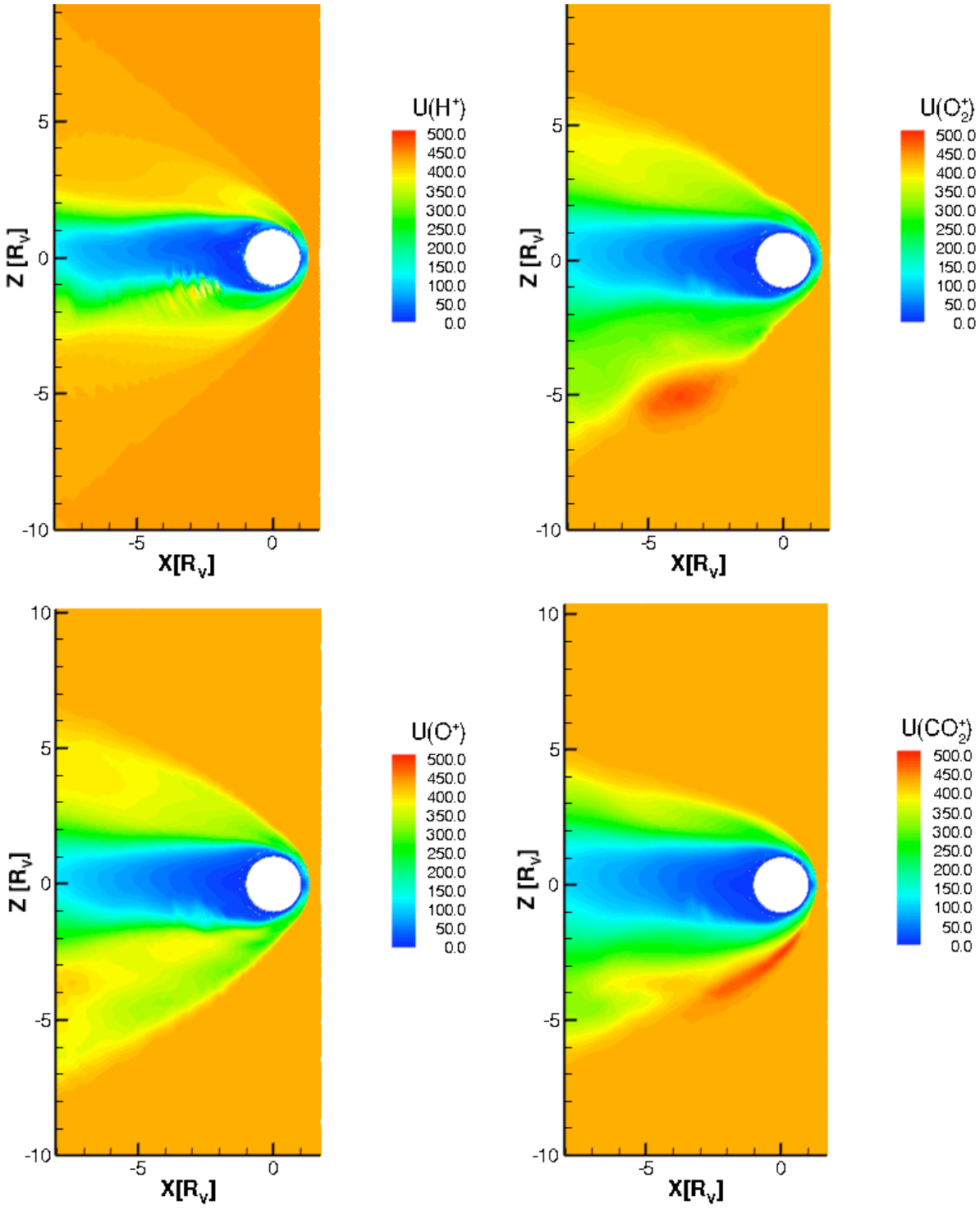

Figure 5.4: Calculated individual velocity for H^+, O_2^+, O^+, CO_2^+ (absolute value). We observe an acceleration of the flow around the body for the ionospheric species

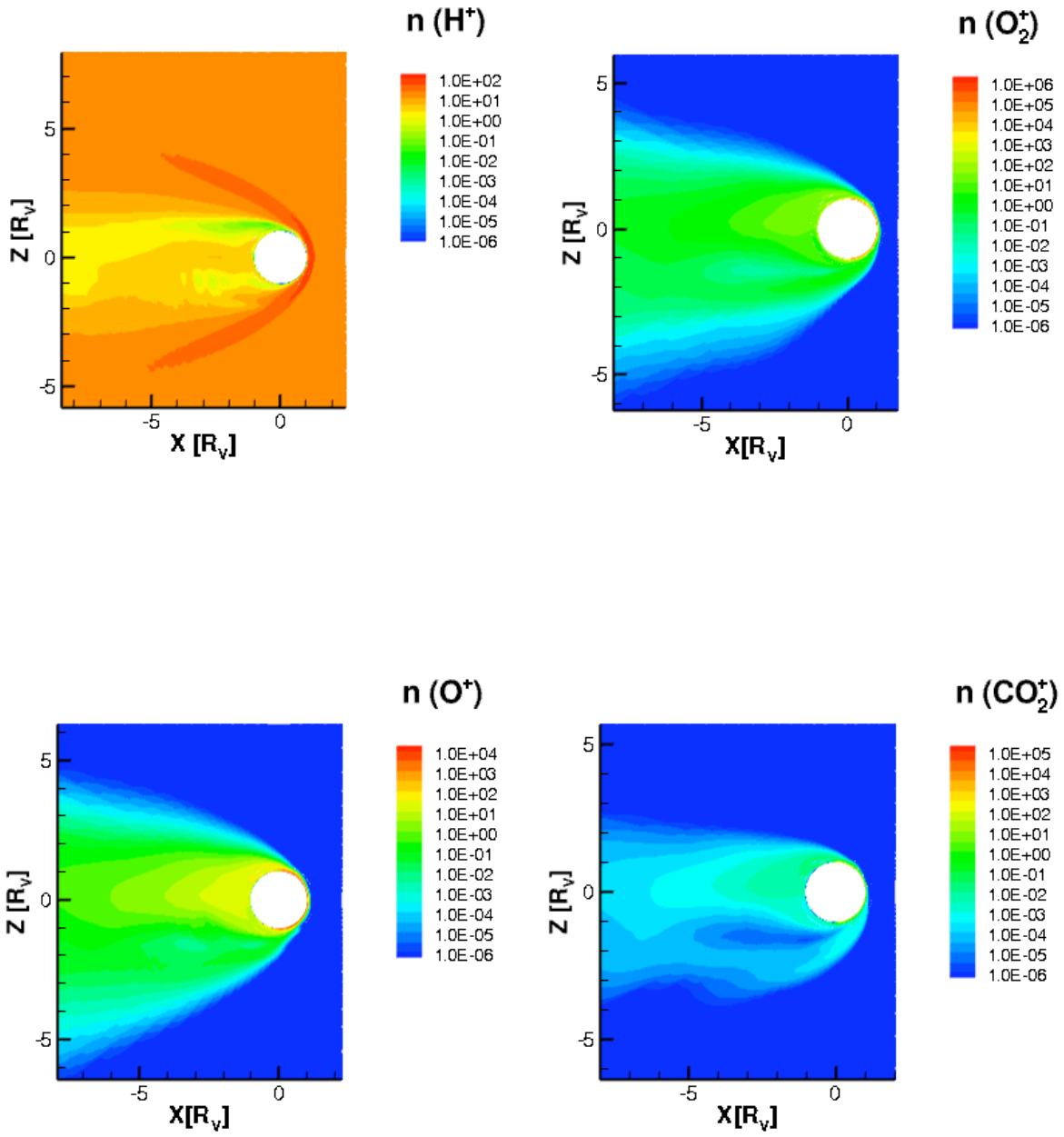

Figure 5.5: The calculated ion number densities in the X-Z plane of H^+, O_2^+, O^+, CO_2^+ for solar minimum condition. Note the use of a logarithmic scale.

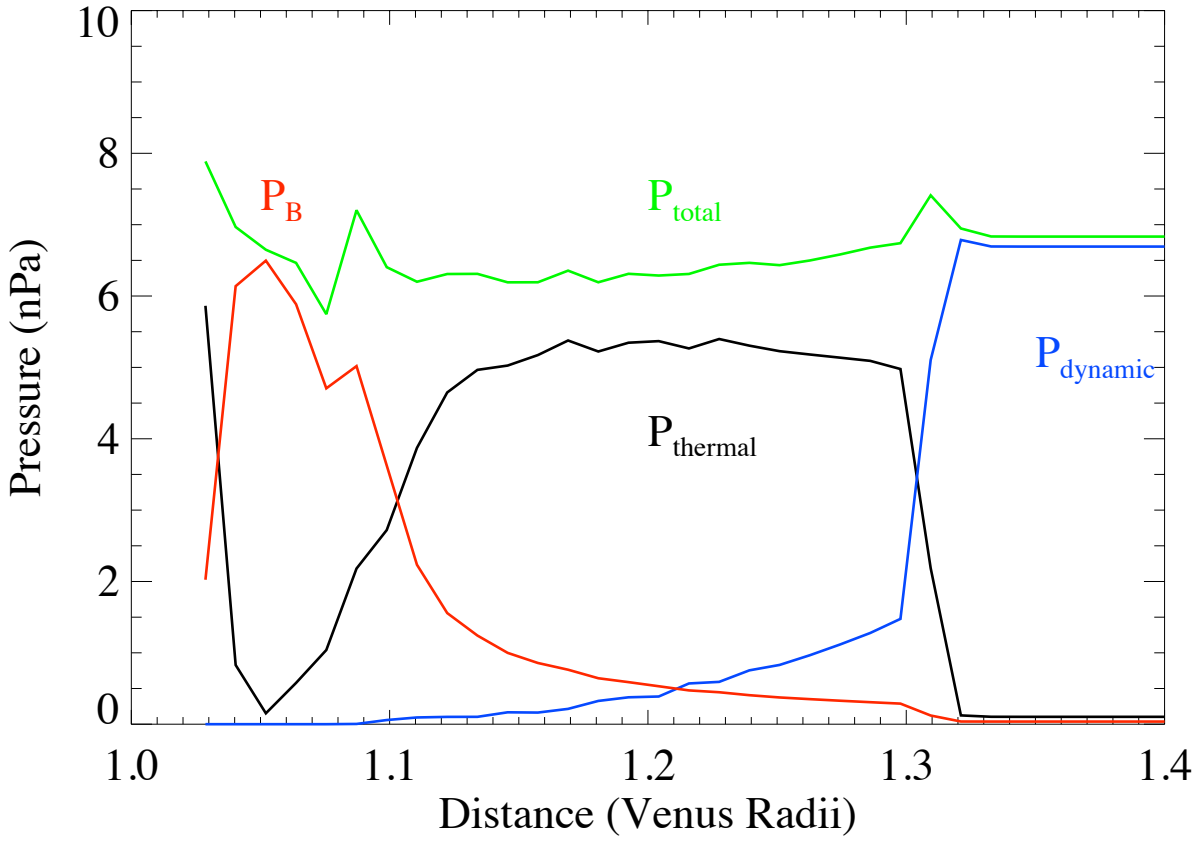

Figure 5.6: Pressure profiles along Sun-Venus line in the dayside for solar minimum (Case 1).

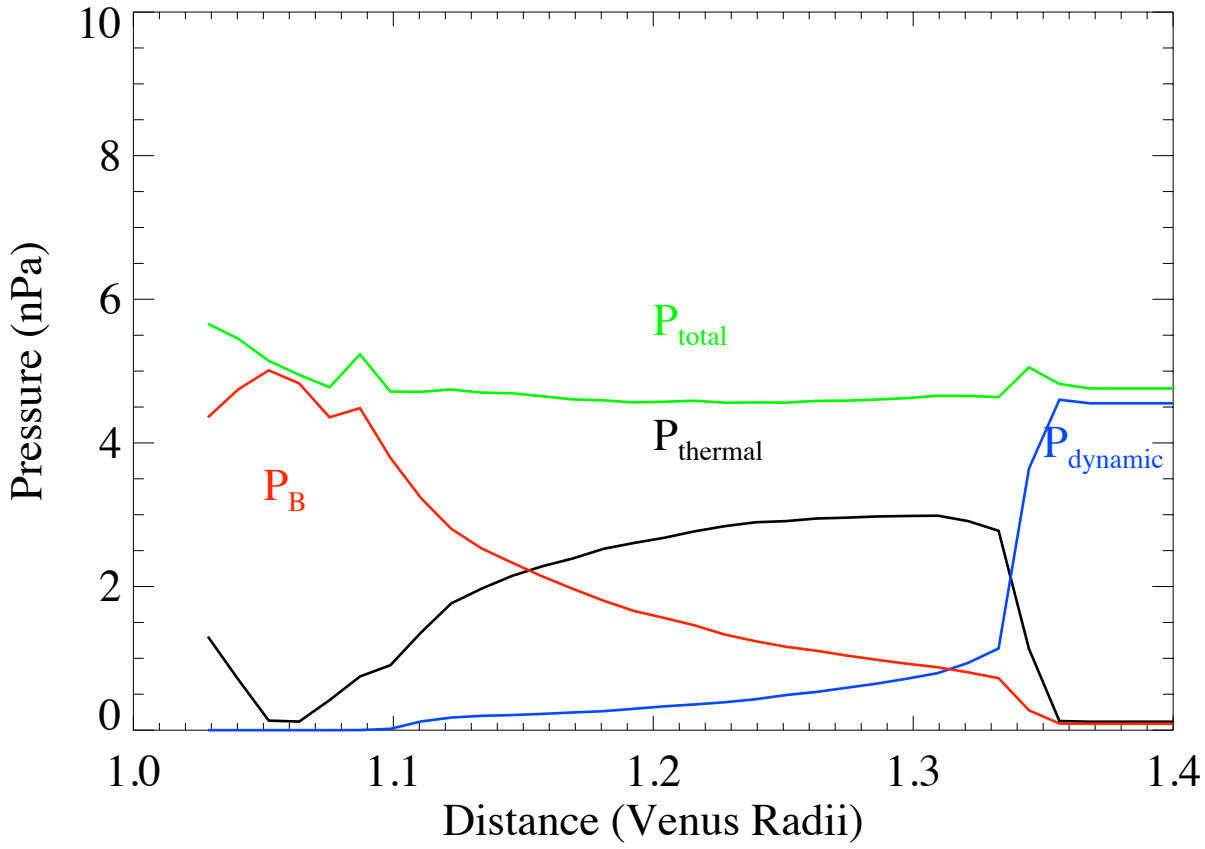

Figure 5.7: Pressure profiles along Sun-Venus line in the dayside for solar maximum (Case 2).

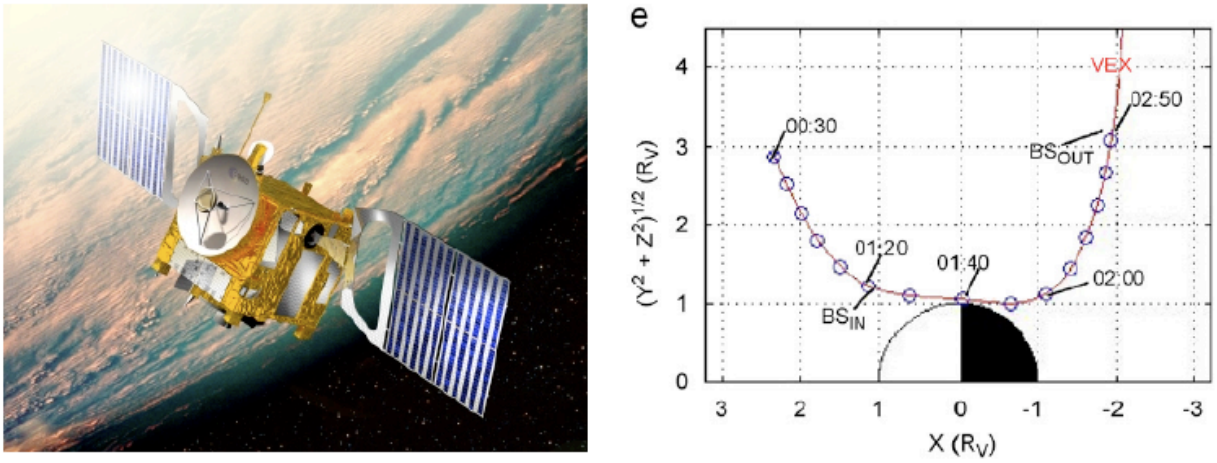

Figure 5.8: Venus Express Spacecraft (left) and trajectory (right)

Our bow shock location is consistent with Pioneer Venus' (PVO) observations of a subosolar bow shock position at 1.36 R_V (*Slavin et al.*, 1980). In Figure 5.2, we can see that the bow shock position at the terminator is around 2.1 R_V which is consistent with Venus Express observations of $\sim$ 2.0 R_V (*Martinecz et al.*, 2008). They are also comparable to the bow shock positions obtained by the single fluid values (*Ma et al.*, 2004) although there seem to be a more significant difference between solar conditions (1.44 R_V for solar maximum and 1.33 R_V for solar minimum).

5.3.4 Comparison to data

We now compare our model results to the observed values. We ran a simulation that corresponds to Venus Express Conditions (Case 3), we compare the magnetic field value, interpolated along Venus Express trajectory (Figure 5.8) to the observed data (Figure 5.9). As we can see, our results fit very well the observations. In comparison, Figure 5.10 shows hybrid model results (*Kallio et al.*, 2008) and single fluid model results (*Ma et al.*, 2009) compared to VEX results.

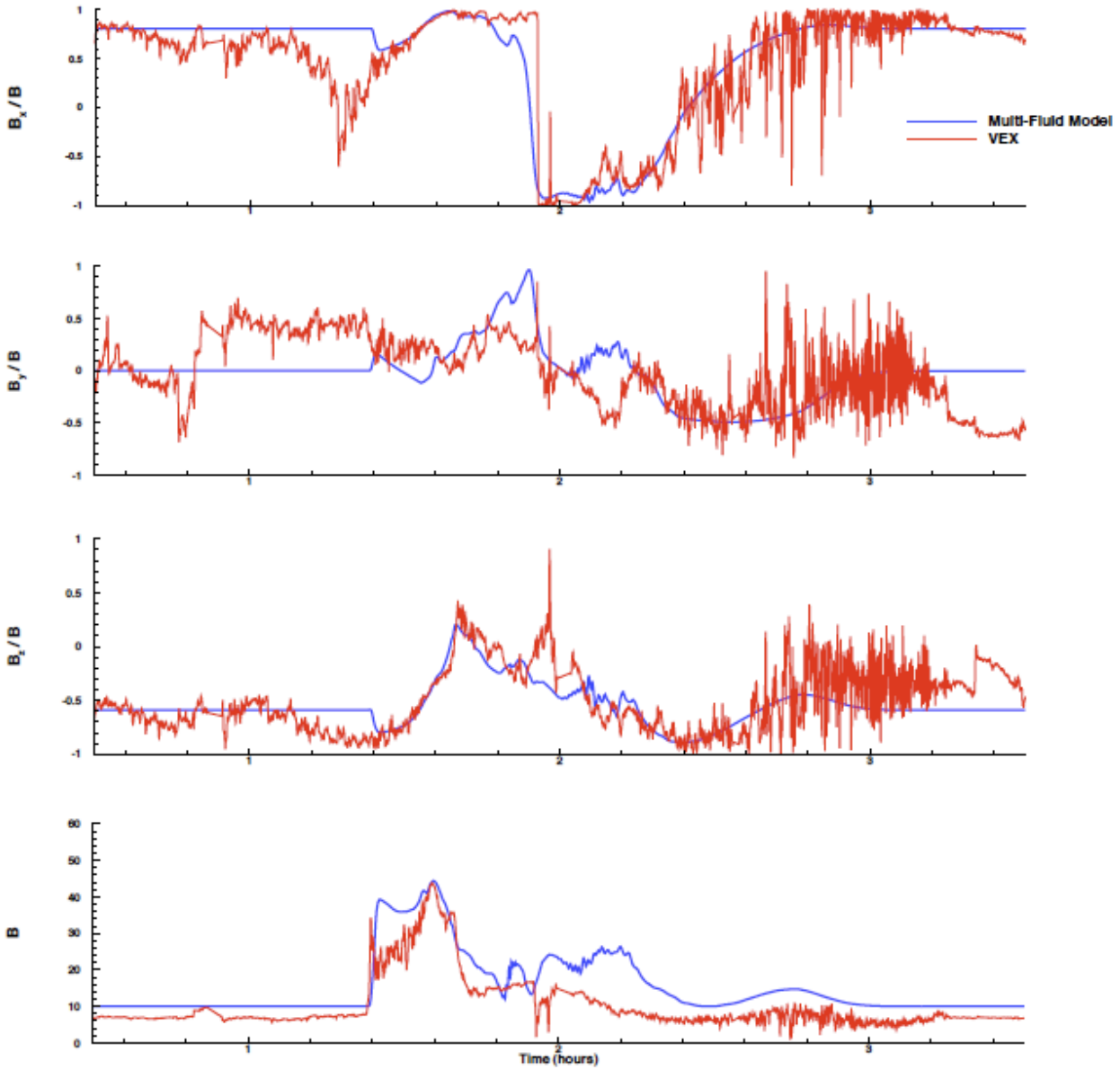

Figure 5.9: Calculated magnetic field for Case 3 along Venus Express (VEX) trajectory, compared to VEX observations

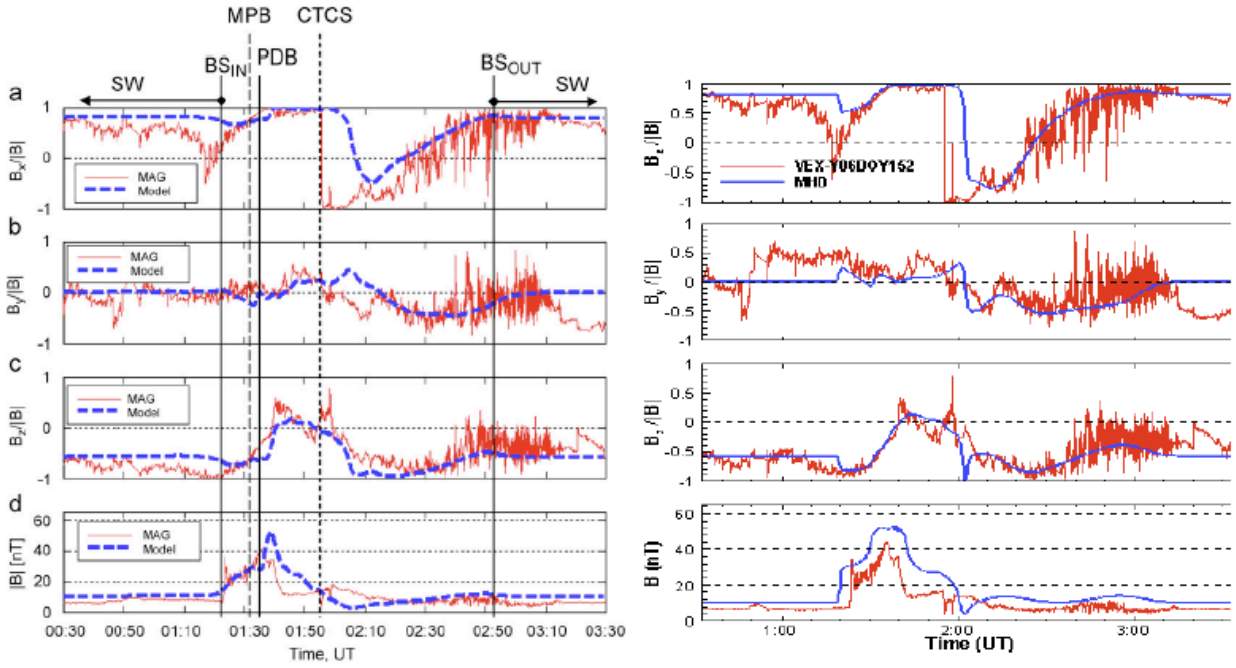

Figure 5.10: Calculated magnetic field by a hybrid mode (left - *Kallio et al.* (2008)) and a single fluid model (right - *Ma et al.* (2009))along Venus Express (VEX) trajectory, compared to VEX data

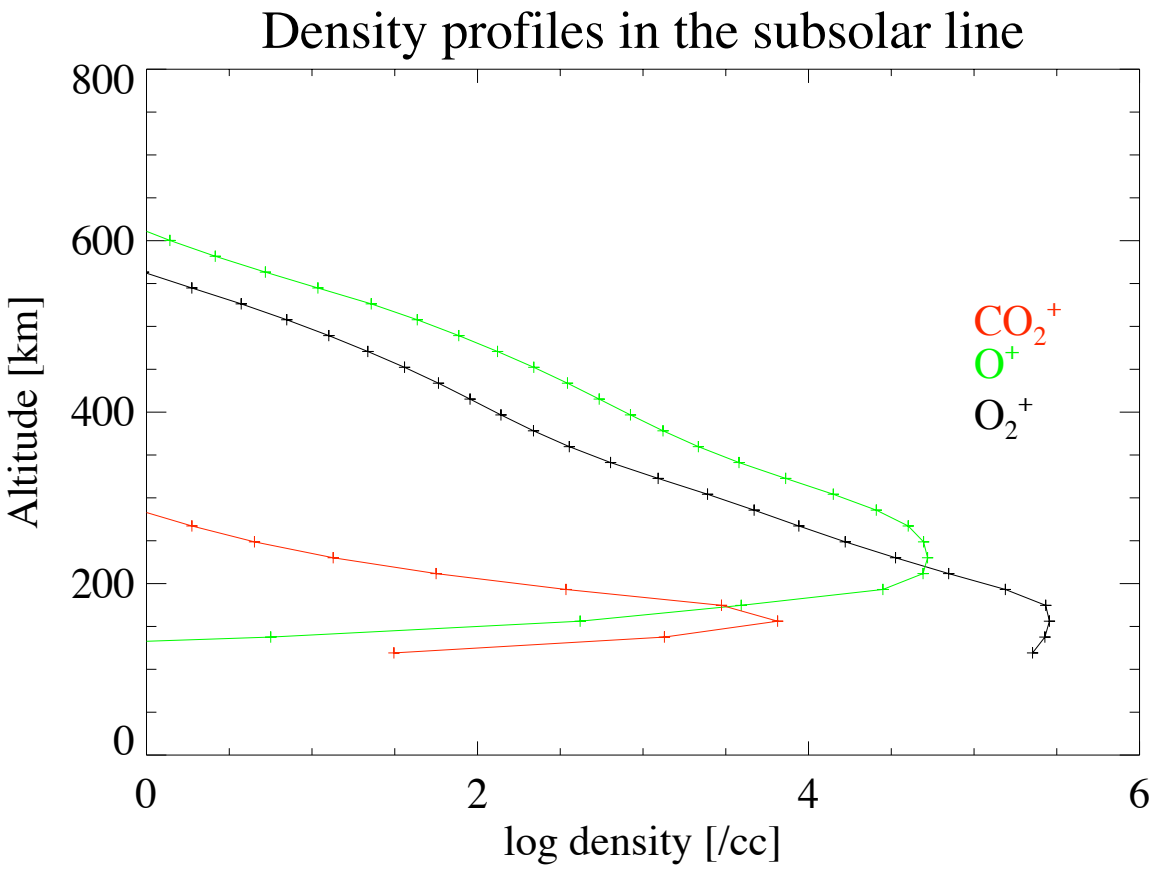

Figure 5.11: The calculated density profile by the multi-fluid model for Case 2

In Figures 5.11, we show our ion density profile along the subsolar line for the solar maximum case. As we can see, our preliminary results do not show the clear ionopause given by the observations in Figure 5.12. This might be due to different reasons: not including a hot oxygen corona and/or not including thermal conduction in our calculations. We are still working on understanding the reasons behind these differences.

5.4 Discussion

The application of our multi-fluid MHD model to Venus gives promising preliminary results. It succeeds in describing new physical processes such as the asymmetries

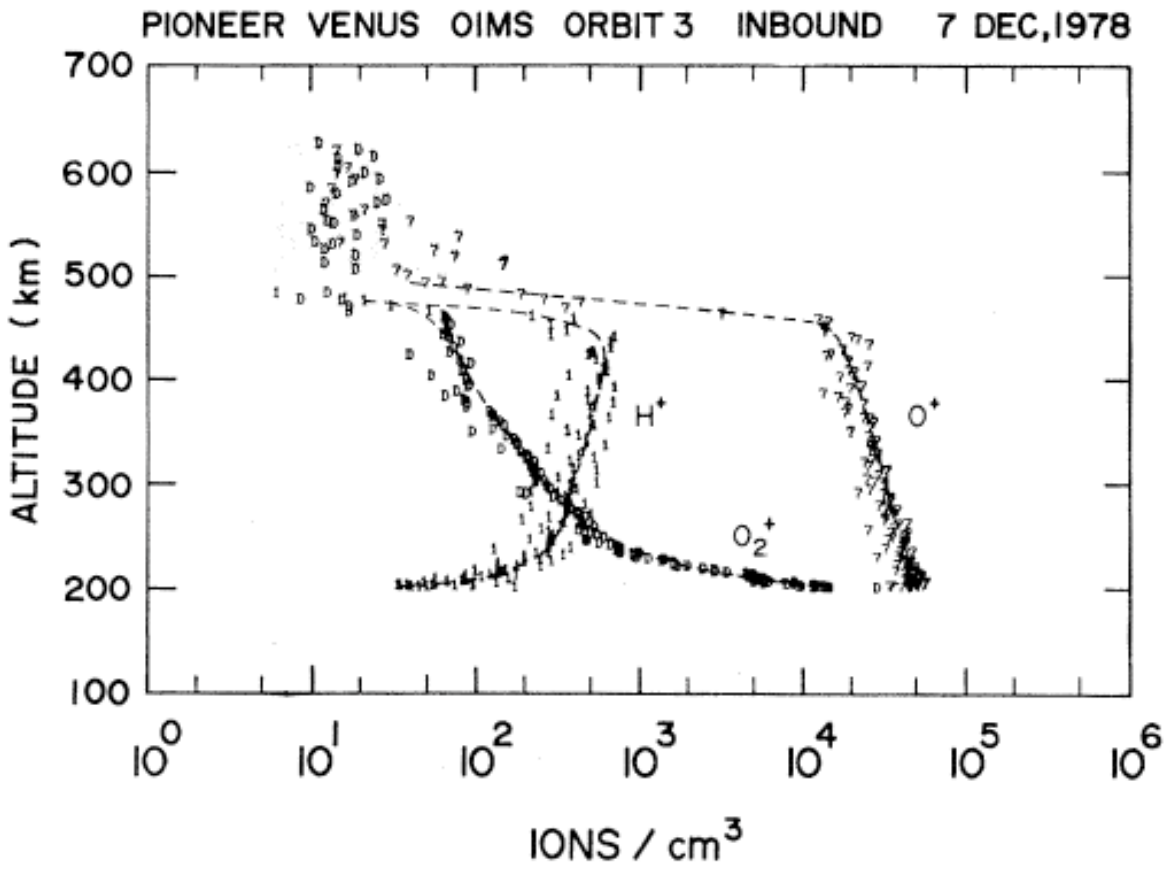

Figure 5.12: Representative altitude profiles of three ions measures by the orbiter ion mass spectrometer. The ionopause is marked by the sharp gradient in O^+ at 500 km (*Taylor et al.*, 1979)

Escape fluxes in s^{-1}	O^+	O_2^+	CO_2^+	Total
Case 1	1.9×10^{25}	2.9×10^{25}	1.3×10^{22}	4.8×10^{25}
Case 2	3.9×10^{25}	6.4×10^{24}	1.3×10^{21}	4.5×10^{25}

Table 5.3: Calculated escape fluxes for Venus using the multi-fluid model

due to the decoupling of the ions, which could not be previously observed with the single fluid model. We observe an asymmetric magnetic pile up, individual velocities and densities.These kinetic effects were shown by hybrid models (*Kallio et al.*, 2006) and are now reproduced by our Venus multi-fluid MHD model.

Our results fit the observed bow shock locations by Pioneer Venus Orbiter and Venus Express, verify the expected differences between solar minimum and maximum conditions and show a good fit to the magnetic field data by Venus Express. We also compute the escape fluxes for both solar minimum and maximum conditions; the results are shown in Table 5.4. We see that although the EUV flux is higher for solar maximum condition, the total plasma escape rates for both conditions are comparable, which is due to the higher dynamic pressure in the solar minimum case. The results given by our model are compatible to ASPERA-4 measurements of oxgen escape corresponding to a lower limit of 10^{25} s^{-1} (*Barabash et al.*, 2007).

Although we can reproduce the asymmetries that we have calculated in Mars' case in the magnetic field, individual velocities and individual densities, these effects are much less pronounced in Venus given the larger radius of the body and the smaller ion gyroradius (due to the stronger interplanetary magnetic field).

We also need to better understand the differences between our subsolar density profile and the observations in Venus case. The observations show the presence of an ionopause in Venus which we do not observe yet. The presence of the ionopause in Venus is an important feature especially in comparison with Mars. An outstanding mystery is why Venus is seen to have a constant ionopause while Mars (which has a similar ionosphere) does not. The application to Venus is also interesting in studying

the interaction of a fully non-magnetized body with the solar wind and how the absence (or presence) of remnant crustal field affects the results. As we saw in the subsolar pressure profile (Figure 5.6) and in the magnetic field 2D plots (Figure 5.2), Venus' magnetic pressure is not as enhanced close to the body as in Mars' case and we do not observe mini-magnetospheres close in Venus' magnetic pile up region (Figure 5.2). A continuation of our work on Venus would definitely lead to an insightful comparative study of the two bodies.

CHAPTER VI

Conclusion and future work

In this work, we use our new multi-fluid MHD model to study the interaction of the solar wind with two non-magnetized solar system bodies: Mars and Venus. Our model gives very good results, depicting new physical processes in the interaction region.

Our multi-fluid model started from the multispecies single fluid MHD model previously developed in the CSEM group. To improve the existing model, we decided to solve individual continuity, momentum and energy equations for every ion; therefore, we take into account the dynamics of the decoupled ions. In both Mars and Venus case, we consider four ion species H^+, O_2^+, O^+ and CO_2^+. Since our main interest is to study the ionospheric region and its interaction with the solar wind, we set our lower boundary to 100 km and our resolution to 10 km, using a spherical adaptive grid.

We first apply our model to Mars' interaction with the solar wind. We use a comprehensive chemical scheme and run simulations for multiple cases such as solar minimum and maximum conditions, and with or without crustal fields and the hot oxygen corona. We obtain asymmetric densities, velocities and magnetic pile up in the X-Z plane. This is the plane that contains the convective electric field E, while the X-Y plane shows symmetric results. The asymmetries in the X-Z plane are the result of the effect of the Lorentz force on the decoupled individual ions. We also observe

gyroradius effects in the individual velocity distributions. These processes are very similar to those calculated by hybrid models which proves that multi-fluid MHD models provide a good and credible way to study Mars' interaction with the solar wind. Our results are consistent with the measured bow shock and MPB locations. We observe a variation of both locations based on the solar condition, the presence and position of the crustal field and the inclusion of the hot oxygen corona.

We compare our calculated density profiles against Viking observed ion densities and MGS total density. We also compute the escape fluxes for multiple cases and compare them to the single fluid results and the observed values from Mars Express. Our calculated values compare very well with the observations. The addition of the Hall effect does not seem to affect our results significantly, nor does it improve our fit to the data.

Another way of validating our model and showing its versatility is to apply it to another non-magnetized solar system body: Venus. Unlike Mars, Venus does not have a crustal magnetic field; it is also bigger in diameter and the upstream magnetic field is much stronger than in Mars environment, resulting in a much smaller gyroradius. The latter combined with the bigger size of the body leads to much less pronounced kinetic effects. Still, we are able to observe similar (but less pronounced) asymmetries in the magnetic field, velocity and density distributions in the X-Z plane. We run our Venus multi-fluid model for solar minimum and maximum conditions and calculate MPB and bow shock positions that fit the observations. We also compare our magnetic field results to Venus Express data and they show a very good fit to the observations. In summary, our preliminary Venus results are very encouraging and prove that our multi-fluid model is versatile and can be applied to other solar system bodies besides Mars.

Our multi-fluid MHD model succeeds in describing non-magnetized planets interaction with the solar wind in a more realistic and accurate manner than the single

fluid model by showing/reproducing physical processes that so far have only been captured by hybrid calculations. This is a very important step since MHD models need less computer resources and can therefore achieve an excellent spatial resolution in the region of interest without exhausting the available resources. So far, the main problem of this type of models has been their inability to capture kinetic effects in regions where the gyroradius becomes comparable to the size of the body. The single fluid approach was clearly a limitation in that respect. The multi-fluid MHD approach appears as a good compromise between accuracy in depicting the physical processes and efficiency in computer time, as long as the ion gyroradius is not too large.

Still, our model can always be improved. We are currently working on solving for the electron pressure equation separately. So far, in both bodies, we have assumed the electron pressure to be equal to the ion pressure, which is a reasonable approximation. However, by solving for the electron and ion pressures separately, we hope to account better for the decoupling between ions and electrons and improve the accuracy of our results.

Another important feature is thermal conduction. So far, we have neglected the divergence of the heat flux, in the individual energy equations. However, we know that heat conduction can be an important transport process in the ionospheric region. We will use the following approximation of the heat flux $\mathbf{h}_s = -\kappa \nabla T_s$, where κ is thermal conductivity and T_s is the individual temperature. We are planning to implement a thermal conductivity term similar to the one used by *Terada et al.* (2009).

Finally, we plan to further pursue our comparative study between Mars and Venus in order to examine key features such as the observed constant ionopause at Venus and the intermittent one at Mars and also understand better the role of the crustal magnetic field. We also plan to use a more realistic atmosphere from the TGCM model (*Bougher et al.*, 2004) that includes seasonal, SZA and longitude variations in

its global structure. In addition, we want to broaden our study to weakly magnetized solar system bodies interaction with the solar wind by including Mercury. The application of our multi-fluid model to Mercury will enable us to describe and understand better how bodies with a weak intrinsic dipole interact with the solar wind. We hope to fully describe the parameters that control the generation, size and transport of the flux transfer events (FTEs) observed by MESSENGER. Our multi-fluid model is also the appropriate tool to study the asymmetric enhanced plumes of heavy ions in Mercury and their role in the Hermean magnetosphere.

BIBLIOGRAPHY

BIBLIOGRAPHY

Acuna, M. H., et al. (1998), Magnetic Field and Plasma Observations at Mars: Initial Results of, *Science*, doi:10.1126/science.279.5357.1676.

Arkani-Hamed, J. (2001), A 50-degree spherical harmonic model of the magnetic field of Mars, *J. Geophys. Res.*, *106*, 23,197–23,208, doi:10.1029/2000JE001365.

Barabash, S., et al. (2007), The loss of ions from Venus through the plasma wake, *Nature*, *450*, 650–653, doi:10.1038/nature06434.

Benna, M., et al. (2009), Modeling the response of the induced magnetosphere of Venus to changing IMF direction using MESSENGER and Venus Express observations, *Geophys. Res. Lett.*, *36*, 4109–+, doi:10.1029/2008GL036718.

Bougher, S. W., S. Engel, R. G. Roble, and B. Foster (1999), Comparative terrestrial planet thermospheres 2. Solar cycle variation of global structure and winds at equinox, *J. Geophys. Res.*, *104*, 16,591–16,611, doi:10.1029/1998JE001019.

Bougher, S. W., S. Engel, R. G. Roble, and B. Foster (2000), Comparative terrestrial planet thermospheres 3. Solar cycle variation of global structure and winds at solstices, *J. Geophys. Res.*, *105*, 17,669–17,692, doi:10.1029/1999JE001232.

Bougher, S. W., S. Engel, D. P. Hinson, and J. R. Murphy (2004), MGS Radio Science electron density profiles: Interannual variability and implications for the Martian neutral atmosphere, *Journal of Geophysical Research (Planets)*, *109*, 3010–+, doi:10.1029/2003JE002154.

Brain, D., et al. (2010), A comparison of global models for the solar wind interaction with Mars, *206*, 139–151, doi:10.1016/j.icarus.2009.06.030.

Brecht, S. H. (1997), Hybrid simulations of the magnetic topology of Mars, *J. Geophys. Res.*, *102*, 4743–4750, doi:10.1029/96JA03205.

Brecht, S. H., and S. A. Ledvina (2006), The Solar Wind Interaction With the Martian Ionosphere/Atmosphere, *Space Sci. Rev.*, *126*, 15–38, doi:10.1007/s11214-006-9084-z.

Chen, R. H., T. E. Cravens, and A. F. Nagy (1978), The Martian ionosphere in light of the Viking observations, *J. Geophys. Res.*, *83*, 3871–3876, doi:10.1029/JA083iA08p03871.

Duru, F., D. A. Gurnett, R. A. Frahm, and J. D. Winningham (2008), Evidence of a Transient Ionopause at Mars Identified from the Excitation of Local Electron Plasma Oscillations, *AGU Fall Meeting Abstracts*, pp. B1316+.

Dwivedi, A. K., and K. K. Mahajan (2003), Plasma distribution at Venus and Ionospheric magnetic fields: Implication for Mars, *Geophys. Res. Lett.*, *30*(24), 240,000–1, doi:10.1029/2003GL018263.

Fox, J. L. (1993), On the escape of oxygen and hydrogen from Mars, *Geophys. Res. Lett.*, *20*, 1747–1750, doi:10.1029/93GL01118.

Fox, J. L., and K. Y. Sung (2001), Solar activity variations of the Venus thermosphere/ionosphere, *J. Geophys. Res.*, *106*, 21,305–21,336, doi:10.1029/2001JA000069.

Glocer, A., G. Tóth, Y. J. Ma, T. Gombosi, J.-C. Zhang, and L. M. Kistler (2009), Multi-fluid BATS-R-US: Magnetospheric composition and dynamics during geomagnetic storms, initial results, *J. Geophys. Res.*, doi:10.1029/2009JA014418.

Godunov, S. K. (1959), A difference scheme for numerical computation of discontinuous solutions of hydrodynamic equations, *47*(3), 271–306, (in Russian).

Gombosi, T. I. (1994), *Gaskinetic Theory*, Cambridge University Press, Cambridge, UK.

Groth, C. P. T., D. L. De Zeeuw, K. G. Powell, T. I. Gombosi, and Q. F. Stout (1999), A parallel solution-adaptive scheme for ideal magnetohydrodynamics, in *Proc. 14th AIAA Computational Fluid Dynamics Conference*, AIAA Paper No. 99-3273, Norfolk, Virginia.

Hansen, K. (2001), Mhd simulations of the magnetospheres of jupiter and saturn: Application to the cassini mission, Ph.D. thesis, Univ. of Michigan, Ann Arbor, USA.

Hanson, W. B., S. Sanatani, and D. R. Zuccaro (1977), The Martian ionosphere as observed by the Viking retarding potential analyzers, *J. Geophys. Res.*, doi:10.1029/JS082i028p04351.

Harnett, E. M., and R. M. Winglee (2003), The influence of a mini-magnetopause on the magnetic pileup boundary at Mars, *Geophys. Res. Lett.*, *30*, 10–1, doi:10.1029/2003GL017852.

Harnett, E. M., and R. M. Winglee (2007), High-resolution multifluid simulations of the plasma environment near the Martian magnetic anomalies, *Journal of Geophysical Research (Space Physics)*, *112*, 5207–+, doi:10.1029/2006JA012001.

Harten, A., P. D. Lax, and B. van Leer (1983), On upstream differencing and Godunov-type schemes for hyperbolic conservation laws, *25*(1), 35–61.

Hedin, A. E., H. B. Niemann, W. T. Kasprzak, and A. Seiff (1983), Global empirical model of the Venus thermosphere, *J. Geophys. Res.*, *88*, 73–83, doi: 10.1029/JA088iA01p00073.

Holmström, M., and E. Kallio (2004), The solar wind interaction with Venus and Mars: energetic neutral atom and X-ray imaging, *Advances in Space Research*, *33*, 187–193, doi:10.1016/j.asr.2003.05.008.

Jarvinen, R., E. Kallio, I. Sillanpää, and P. Janhunen (2008), Hybrid modelling the Pioneer Venus Orbiter magnetic field observations, *Advances in Space Research*, *41*, 1361–1374, doi:10.1016/j.asr.2007.10.003.

Kallio, E., R. Jarvinen, and P. Janhunen (2006), Venus solar wind interaction: Asymmetries and the escape of Op ions, *Planet. Space Sci.*, pp. 1472–1481, doi: 10.1016/j.pss.2006.04.030.

Kallio, E., K. Liu, R. Jarvinen, V. Pohjola, and P. Janhunen (2010), Oxygen ion escape at Mars in a hybrid model: High energy and low energy ions, *206*, 152–163, doi:10.1016/j.icarus.2009.05.015.

Kallio, E., et al. (2008), The Venusian induced magnetosphere: A case study of plasma and magnetic field measurements on the Venus Express mission, *Planet. Space Sci.*, *56*, 796–801, doi:10.1016/j.pss.2007.09.011.

Knudsen, W. C., K. Spenner, K. L. Miller, and V. Novak (1980), Transport of ionospheric O/+/ ions across the Venus terminator and implications, *J. Geophys. Res.*, *85*, 7803–7810, doi:10.1029/JA085iA13p07803.

Krymskii, A. M., T. K. Breus, N. F. Ness, M. H. Acuña, J. E. P. Connerney, D. H. Crider, D. L. Mitchell, and S. J. Bauer (2002), Structure of the magnetic field fluxes connected with crustal magnetization and topside ionosphere at Mars, *Journal of Geophysical Research (Space Physics)*, *107*, 1245–+, doi:10.1029/2001JA000239.

Ledvina, S. A., Y. Ma, and E. Kallio (2008), Modeling and Simulating Flowing Plasmas and Related Phenomena, *Space Sci. Rev.*, *139*, 143–189, doi:10.1007/s11214-008-9384-6.

Linde, T. J. (1998), A three-dimensional adaptive multifluid MHD model of the heliosphere, Ph.D. thesis, Univ. of Mich., Ann Arbor.

Liu, Y., A. F. Nagy, C. P. T. Groth, D. L. DeZeeuw, T. I. Gombosi, and K. G. Powell (1999), 3D multi-fluid MHD studies of the solar wind interaction with Mars, *Geophys. Res. Lett.*, *26*, 2689–2692, doi:10.1029/1999GL900584.

Liu, Y., A. F. Nagy, T. I. Gombosi, D. L. Dezeeuw, and K. G. Powell (2001), The solar wind interaction with Mars: results of three-dimensional three-species MHD studies, *Advances in Space Research*, *27*, 1837–1846, doi:10.1016/S0273-1177(01)00301-5.

Lundin, R., S. Barabash, M. Holmström, H. Nilsson, M. Yamauchi, M. Fraenz, and E. M. Dubinin (2008), A comet-like escape of ionospheric plasma from Mars, *Geophys. Res. Lett.*, *35*, 18,203–+, doi:10.1029/2008GL034811.

Ma, Y. (2006), 3d multi-species global mhd studies of the solar wind interaction with mars and saturn's magnetospheric plasma flow with titan, Ph.D. thesis, Univ. of Michigan, Ann Arbor, USA.

Ma, Y., A. F. Nagy, K. C. Hansen, D. L. De Zeeuw, T. I. Gombosi, and K. Powell (2002), Three-dimensional multispecies MHD studies of the solar wind interaction with Mars in the presence of crustal fields, *J. Geophys. Res.*, *107*(A10), 1282, doi:10.1029/2002JA009293.

Ma, Y., A. N. annd I.V. Sokolov, and K. Hansen (2004), Three-dimensional, multispecies, high spatial resolution MHD studies of the solar wind interaction with Mars, *J. Geophys. Res.*, *109*, A07,211, doi:10.1029/2003JA010367.

Ma, Y., C. T. Russell, A. F. Nagy, T. L. Z. an J. G. Luhmann, and H. Y. Wei (2009), Mhd study of the solar wind interaction with venus, EGU AGU Meeting, 2009.

Ma, Y. J., et al. (2007), 3D global multi-species Hall-MHD simulation of the Cassini T9 flyby, *Geophys. Res. Lett.*, *34*, doi:10.1029/2007GL031627.

Martinecz, C., et al. (2008), Location of the bow shock and ion composition boundaries at Venus:initial determinations from Venus Express ASPERA-4, *Planet. Space Sci.*, *56*, 780–784, doi:10.1016/j.pss.2007.07.007.

Mitchell, D. L., R. P. Lin, C. Mazelle, H. Rème, P. A. Cloutier, J. E. P. Connerney, M. H. Acuña, and N. F. Ness (2001), Probing Mars' crustal magnetic field and ionosphere with the MGS Electron Reflectometer, *J. Geophys. Res.*, *106*, 23,419–23,428, doi:10.1029/2000JE001435.

Modolo, R., G. M. Chanteur, E. Dubinin, and A. P. Matthews (2006), Simulated solar wind plasma interaction with the Martian exosphere: influence of the solar EUV flux on the bow shock and the magnetic pile-up boundary, *Annales Geophysicae*, *24*, 3403–3410, doi:10.5194/angeo-24-3403-2006.

Nagy, A. F., T. E. Cravens, S. G. Smith, H. A. Taylor, and H. C. Brinton (1980), Model calculations of the dayside ionosphere of Venus - Ionic composition, *J. Geophys. Res.*, *85*, 7795–7801, doi:10.1029/JA085iA13p07795.

Nier, A. O., and M. B. McElroy (1977), Composition and structure of Mars' upper atmosphere - Results from the neutral mass spectrometers on Viking 1 and 2, *J. Geophys. Res.*, *82*, 4341–4349, doi:10.1029/JS082i028p04341.

Powell, K., P. Roe, T. Linde, T. Gombosi, and D. L. De Zeeuw (1999), A solution-adaptive upwind scheme for ideal magnetohydrodynamics, *J. Comp. Phys.*, *154*, 284–309.

Powell, K. G. (1994), An approximate Riemann solver for magnetohydrodynamics (that works in more than one dimension), *Tech. Rep. 94-24*, Inst. for Comput. Appl. in Sci. and Eng., NASA Langley Space Flight Center, Hampton, Va.

Powell, K. G., et al. (2006), Parallel adaptive solution of the MHD equations and its role in the Space-Weather Modeling Framework, in *Numerical Modeling of Space Plasma Flows*, *Astronomical Society of the Pacific Conference Series*, vol. 359, edited by G. P. Zank and N. V. Pogorelov, p. 33.

Ramshaw, J. (1983), A method for enforcing the solenoidal condition on magnetic fields in numerical calculation, *J. Comp. Phys.*, *52*, 592.

Schunk, R., and A. Nagy (2009), *Ionospheres*, Cambridge Press, Cambridge University.

Schunk, R. W., and A. F. Nagy (1980), Ionospheres of the terrestrial planets, *Rev. Geophys. Space Phys.*, *18*, 813–852.

Shinagawa, H., and S. W. Bougher (1999), A two-dimensional MHD model of the solar wind interaction with Mars, *Earth, Planets, and Space*, *51*, 55–60.

Shinagawa, H., and T. E. Cravens (1989), A one-dimensional multispecies magnetohydrodynamic model of the dayside ionosphere of Mars, *J. Geophys. Res.*, *94*, 6506–6516, doi:10.1029/JA094iA06p06506.

Simon, S., A. Boesswetter, T. Bagdonat, and U. Motschmann (2007), Physics of the Ion Composition Boundary: a comparative 3-D hybrid simulation study of Mars and Titan, *Annales Geophysicae*, *25*, 99–115, doi:10.5194/angeo-25-99-2007.

Slavin, J. A., et al. (1980), The solar wind interaction with Venus - Pioneer Venus observations of bow shock location and structure, *J. Geophys. Res.*, *85*, 7625–7641, doi:10.1029/JA085iA13p07625.

Spreiter, J., A. Summers, and A. Alksne (1966), Hydrodynamic flow around the magnetosphere, *Planet. Space Sci.*, *14*, 223.

Szegö, K., et al. (2000), Physics of mass loaded plasmas, *Space Sci. Rev.*, *94*, 429–671.

Tanaka, T. (1993), Configurations of the solar wind flow and magnetic field around the planets with no magnetic field: Calculation by a new MHD simulation scheme, *J. Geophys. Res.*, *98*, 17,251–17,262, doi:10.1029/93JA01516.

Tanaka, T., and K. Murawski (1997), Three-dimensional MHD simulation of the solar wind interaction with the ionosphere of Venus: Results of two-component reacting plasma simulation, *J. Geophys. Res.*, *102*, 19,805–19,822, doi:10.1029/97JA01474.

Taylor, H. A., H. C. Brinton, S. J. Bauer, R. E. Hartle, P. A. Cloutier, R. E. Daniell, and T. M. Donahue (1979), Ionosphere of Venus - First observations of day-night variations of the ion composition, *Science*, *205*, 96–99, doi: 10.1126/science.205.4401.96.

Terada, N., H. Shinagawa, T. Tanaka, K. Murawski, and K. Terada (2009), A three-dimensional, multispecies, comprehensive MHD model of the solar wind interaction with the planet Venus, *Journal of Geophysical Research (Space Physics)*, *114*, 9208–+, doi:10.1029/2008JA013937.

Tóth, G., Y. J. Ma, and T. I. Gombosi (2008), Hall magnetohydrodynamics on block adaptive grids, *J. Comp. Phys.*, *227*, 6967–6984, doi:10.1016/j.jcp.2008.04.010.

Tóth, G., et al. (2011), Adaptive numerical algorithms in space weather modeling, *J. Comp. Phys.*

Vignes, D., M. H. Acuña, J. E. P. Connerney, D. H. Crider, H. Rème, and C. Mazelle (2002), Factors controlling the location of the Bow Shock at Mars, *Geophys. Res. Lett.*, *29*(9), 090,000–1, doi:10.1029/2001GL014513.

Vignes, D., et al. (2000), The solar wind interaction with Mars: Locations and shapes of the Bow Shock and the magnetic pile-up boundary from the observations of the MAG/ER experiment onboard Mars Global Surveyor, *Geophys. Res. Lett.*, *27*, 49–52, doi:10.1029/1999GL010703.

Vignes, M. S. (1989), Time-dependent MHD simulations for cometary plasmas, *Astron. Astrophys.*, *433*.

Wu, C. C. (1992), MHD flow past an obstacle - Large-scale flow in the magnetosheath, *Geophys. Res. Lett.*, *19*, 87–90, doi:10.1029/91GL03007.

Zhang, T. L., J. G. Luhmann, and C. T. Russell (1991), The magnetic barrier at Venus, *J. Geophys. Res.*, *96*, 11,145–+, doi:10.1029/91JA00088.